Motion Analysis of a Semi-Submersible Crane Vessel at Inconvenient Draft

A Flooding Tank Approach

T.G. Vos

Master of Science Thesis

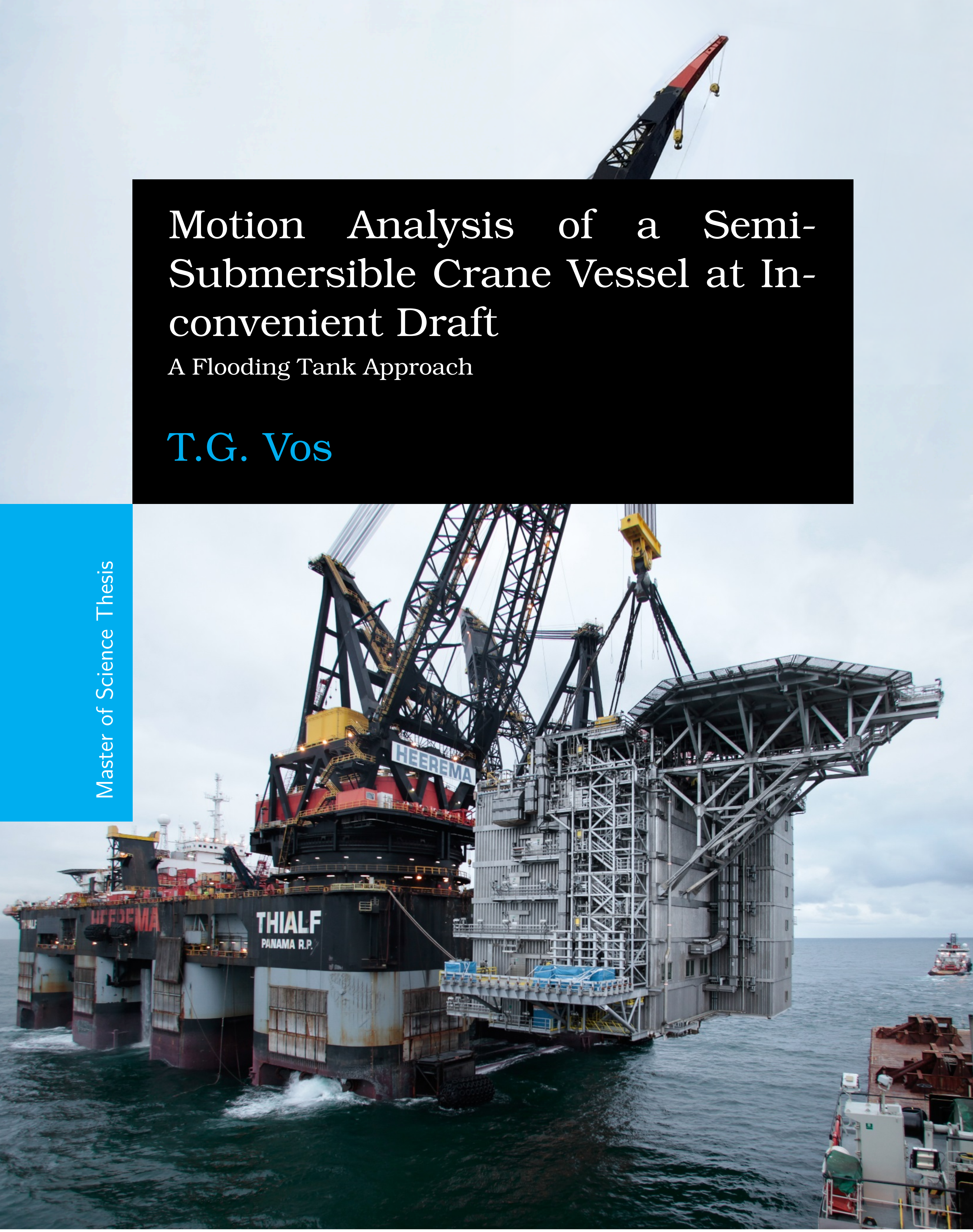

TU Delft
Delft
University of
Technology

Mechanical, Maritime and Materials Engineering

The work in this thesis was supported by Heerema Marine Contractors. Their cooperation is hereby gratefully acknowledged.

Cover figure: photograph of the SSCV Thialf at inconvenient draft, installing the living quarters module of Clair Ridge *(Courtesy of BP p.l.c.).*

Motion Analysis of a Semi-Submersible Crane Vessel at Inconvenient Draft

A Flooding Tank Approach

BY

T.G. Vos

in partial fulfillment of the requirements for the degree of

Master of Science

in Offshore & Dredging Engineering

at the Delft University of Technology,

to be defended publicly on Friday September 25, 2015 at 11:00 AM.

Chair	Prof.dr.ir. R.H.M. Huijsmans	Delft University of Technology
Committee	Ir. J. den Haan	Delft University of Technology
	Dr. ir. A. Romeijn	Delft University of Technology
	Dr. ir. A. Vrijdag	Delft University of Technology
	Ir. I. van Winsen	Heerema Marine Contractors
	Ir. R. van Dijk	Heerema Marine Contractors

Abstract

Heerema Marine Contractors is an offshore contractor, notable for operating three of the four largest semi-submersible crane vessels in the industry. These vessels are intended to operate at a deep draft with the pontoons well submerged. During transits the SSCVs are de-ballasted, resulting in the pontoons piercing the water surface.

In some situations, it became clear that the SSCVs are not able to reach the required draft. For example when the SSCV is operating in shallow waters, it is not possible to ballast to the operational draft with the pontoons well submerged. Instead, the pontoons are just below the water surface. This draft is internally referred to as the ”inconvenient draft”.

Both full scale and model tests observations shows that the shallow layer of water on top of the submerged pontoons behaves different than the surrounding water. For small wave heights standing waves are present at the shallow layer on top of the pontoons. For higher waves non-linearities, like breaking waves and emergence of the pontoons, are observed. The conventional programs to calculate the motion behavior of the SSCVs are not able to predict the motions of the vessel, due to the non-linearities involved.

In this research a flooding tank approach is used to capture the non-linear behavior of a body at inconvenient draft. The region on top of the submerged body is defined as a free flooding tank. During a time-domain simulation, the water inside the free flooding tank is calculated at each time step. This tank water exerts a static force on the top surface of the body. The diffraction and radiation forces on the remaining wetted surface of the body will be acquired using the results of a previously executed radiation diffraction analysis.

Firstly, the numerical model is applied to a captive submerged cylinder to calculate the excitation forces on the body. For a wave height and submergence of 1 meter, the numerical model is able to capture the non-linear force response. In case of a wave height of 2m and 4m, the response is over predicted. The cause of this discrepancy is assigned to the linear tank boundary conditions used in the model. At a submergence of 3m and 7m, good correspondence is found.

Secondly, the model is applied to a SSCV at inconvenient draft. Here it can be concluded that the numerical model does not entire fulfill the objective. The obtained RAOs do not show the wave height dependency for both heave and roll. Nevertheless, the numerical model shows a significant improvement in the results compared to the results using the conventional programs.

Preface

This report describes the research conducted for the final steps of the Master of Science in Offshore & Dredging Engineering at the Delft University of Technology. During my bachelor's degree in mechanical engineering, the offshore world and particularly vessel motions have already been an increasingly interesting topic for me. In combination with the challenging projects within the offshore industry, the choice of doing a subsequent degree in this field was evident. I am thankful for the opportunity Heerema Marine Contractors has given me to conduct this research. Graduation within this company has definitely confirmed my choice of doing this master's degree.

I wish to thank various people for their contribution to this thesis. First and foremost my daily supervisor Ivan. You always made time for me in case I got stuck. During my entire graduation, I have never heard from you that you were too busy if I had some questions. Thanks for your assistance and thorough feedback of the draft report. I would like to thank Radboud for keeping the helicopter view during the whole thesis. Your shared insights and critiques were very useful and always pushed me to go further. In no particular order I would like to thank Harald, Eelco, Geert and Job for the valuable and constructive suggestions during the various internal meetings.

From the university I would like to thank Professor Huijsmans. First of all as being the chair of my graduation committee. You always showed great enthusiasms and were very supportive during the progress meetings. Secondly, for the interesting lectures in the field of hydromechanics. These lectures have certainly contributed to my interest in the offshore world.

Finally, I would like to thank Eline for the moral support during the last months. You aways had to listen to daily progress, achievements and setbacks. Despite it is not your field of interest, you always managed to be supportive and encouraging.

Enjoy reading!

Leiden, September 2015

Thijs

Table of Contents

Appendices

Chapter 1

Introduction

Heerema Marine Contractors (HMC) is an offshore contractor, notable for operating three of the four largest semi-submersible crane vessels (SSCVs) in the industry; SSCV Thialf with a maximum crane capacity of 14.200mT, SSCV Hermod with 8.100mT and SSCV Balder with 6.945mT. In addition, an even larger crane vessel with a crane capacity of 20.000mT will be added to the fleet in the coming years. These vessels are used for the installation and removal of all types of fixed and floating offshore structures, subsea pipelines and infrastructures in both shallow and deep water.

The SSCVs consists of two pontoons and a deck supported by three or four columns on each of the pontoons. Inside the pontoons and columns large ballast tank are present. By regulating the amount of ballast water in these tanks, the draft of the vessel can be optimized to the environmental and working conditions. In case the tanks are empty the draft of the SSCV is as low as possible and the pontoons emerge from the water surface, see figure 1-1a. This draft is used during transits and therefore known as the transit draft. During operations the SSCVs are ballasted to a deep draft with the pontoons well submerged, this is known as the operational draft, see figure 1-1b.

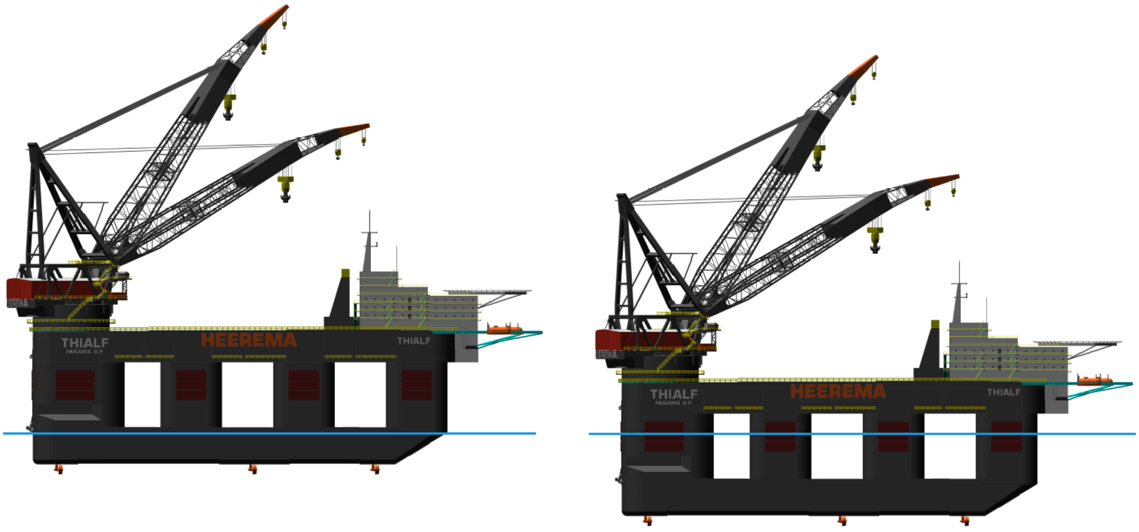

(a) *Transit draft with the pontoons piercing the water surface.*

(b) *Operational draft with the pontoons well submerged.*

Figure 1-1: *SSCV Thialf at two regular drafts*

In some situations however, it became clear that the SSCVs are not able to reach the appropriate draft for the environmental and working conditions. For example when the SSCV Thialf had to sail with a heavy structure in the cranes, it was not able to reach the transit draft due to the extra weight of the structure. Instead of the pontoons emerging from the water surface, the pontoons were just submerged (figure 1-2). There are also situations where the SSCV is not able to reach the desired operational draft. For example during the summer of 2014 when the SSCV Thialf had to install a platform in a shallow part of the North Sea. Instead of ballasting to the full operational draft of 26 m, the SSCV Thialf was forced to operate at a draft of only 16 m due to limited water depth. This also resulted in the pontoons to be just below the water surface.

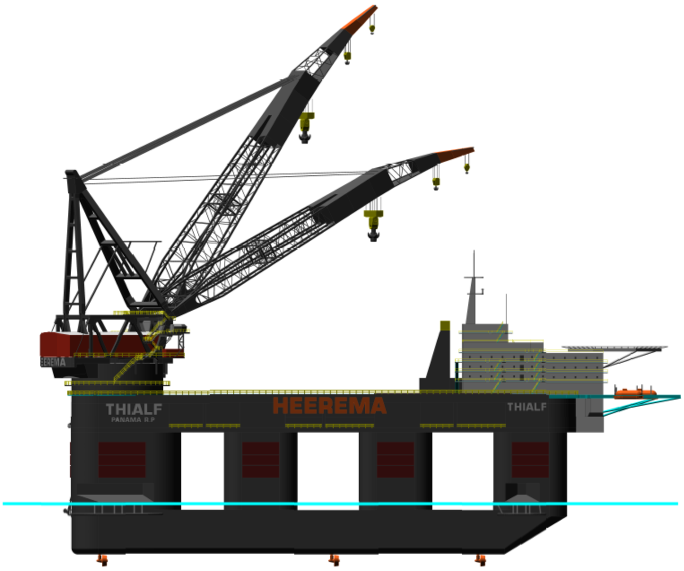

Figure 1-2: *SSCV Thialf with the pontoons just below the water surface, known as inconvenient draft.*

The draft with the pontoons just below the water surface is internally referred to as the “inconvenient draft”. During activities with the SSCV at this draft, it became clear that the shallow layer of water on top of the pontoons behaves different than the surrounding water. In this shallow water region the waves become isolated from the surrounding sea and non-linearities like breaking waves are observed. In addition to that, part of the pontoon could emerge resulting in rapid changes in water plane area.

1-1 Motivation

For both operational and transit draft, the conventional computer programs for calculating vessel motions haven proven themselves to be effective and reliable. During the preparation of a certain project however, it became clear that this is not the case for the inconvenient draft as described above (hence the “inconvenience”). Due to the non-linearities in the shallow water region above the pontoons the linear assumptions that underlie these conventional computer programs are not valid any more. This results in calculation of extreme water elevations on top of the pontoons and, as a consequence, calculation of incorrect motions of the SSCV. Proper understanding of these motions is in turn required for the structural assessment of, for example, sea fastening and to determine the weather window during operations. Eventually HMC was forced to perform expensive and time consuming model tests for this project. The model test result showed indeed non-linearities in the motion behavior.

A drawback of the model tests is that the obtained results are only valid for the applied loading and wave conditions. Especially due to the non-linearities involved. Since it is required to predict the behavior in advance and not have to redo new model tests, several in-house attempts have been made within HMC to better capture the model tests results. Unfortunately without the desired results. Finally the transit draft model was hand-tuned by trial and error to fit the measured results of the inconvenient draft. Even though the results showed some agreements with the model tests, the hand-tuning was done without respecting any physics and it is impossible to say if the tuned properties are physically correct.

To get a better grip on the motions of a SSCV at inconvenient draft, a new numerical model is developed as part of this graduation thesis.

Objective

Heerema Marine Contractors is not able to predict the motion response of a semi-submersible crane vessel with the conventional computer programs in case the pontoons are 3 m or less below the free surface. Therefore the objective of this thesis is:

> *To develop a numerical model which is capable of calculating the motion behavior of a SSCV at a draft where the pontoons are 3 meter or less below the free surface.*

This objective is divided into to the following sub-objectives:

1. Perform a literature study to gain more insight in available methods and to select the most appropriate method for the numerical model;
2. Apply the numerical model to a captive body at inconvenient draft to acquire the excitation forces;
3. Extend the numerical model to simulate the motion behavior of a body at inconvenient draft.

1-2 Background

Semi-Submersibles

Semi-submersibles are specialized marine vessels used in a number of specific offshore roles such as drilling, production and heavy lifting. They are generally characterized by two pontoons and a deck supported by two, three or four columns on each of the pontoons. The major advantage of this remarkable design is that semi-submersibles generally show far less motions than mono-hull vessels. This makes them especially suitable for tasks with very strict motion requirements.

What makes these type of vessels to have such a favorable motion behavior? As soon as the ballast tanks of the semi-submersible are being filled, the overall mass m of the vessel increases significantly. As a result the draft of the vessel increases and, due to their design, the pontoons disappear far below the water surface. In addition, the columns of the vessel now pierce the water surface which makes the water plane area A_{wl} (i.e. the total surface area of the hull piercing the water plane) relative small. The large mass and small water plane area result in a relatively long natural period T_n of the vessel, since:

$$T_n \propto \sqrt{\frac{m}{A_{wl}}}$$

As the natural periods are significantly longer than the wave excitation periods and due to the transparent character of the semi-submersibles, the wave forcing is significantly lower. This leads to the semi-submersibles to have a very low motion response. For HMC this result in a high workability and low weather on weather time.

Response Amplitude Operators

In most cases the motion behavior of a vessel is indicated with the frequency-domain equation of motion. This equation follows from applying Newton's second law on a vessel is waves:

$$M\ddot{\vec{x}}(\omega) = \vec{F}_{diff} + \vec{F}_{rad} + \vec{F}_{rest} \tag{1-1a}$$

$$= \vec{F}_{diff} - A\ddot{\vec{x}} - B\dot{\vec{x}} - C\vec{x} \tag{1-1b}$$

Here, the first term on the right hand side of (1-1a) is the excitation force due to the incoming and diffracted waves on a fixed body and the second term is the hydrodynamic reaction force due to waves radiating from the oscillating body in still water. This second term can be split into a part in-phase with the acceleration $\ddot{\vec{x}}$ and a part in-phase with the velocity $\dot{\vec{x}}$ of the vessel, as shown in (1-1b). The third term in (1-1a) is the hydrostatic reaction or restoring force and is proportional to the motion $\vec{x}$. The force $\vec{F}_{diff}$ and the coefficients A, B and C are computed by hydrodynamic codes. Most commercially available hydrodynamic codes are based on potential theory and the frequency-domain approach and require data of the geometry of the vessel and its mass and load distribution as input.

The term $\vec{F}_{diff}$ is considered as the frequency response function (FRF) of the vessel from wave to force. This function describes the force of the vessel, due to an incoming wave with a certain amplitude and frequency. As soon as $\vec{F}_{diff}$ and the coefficients A,

B and C are known, equation (1-1b) can be used to obtain the FRF of the vessel from force to motion. Similar as the force FRF, this function describes the motion response of the vessel due to an applied force with a certain amplitude and frequency. The magnitude of the frequency response functions is commonly called Response Amplitude Operator (RAO) in the marine environment. The phase angle follows from the ratio between the real and imaginary part. In this work the terms force RAO and motion RAO are used to indicate respectively the force and motion response. The term FRF is occasionally used to denote both the magnitude and phase at once.

An essential property of the FRF is that it is linear. This implies that, at each frequency, the ratio as well as the phase shift between the output and the input is constant. Thus doubling the input (e.g. the wave amplitude) results in a doubled output (a double force amplitude), while the phase shift between the output and input does not change. The linearity of the FRFs makes it possible to combine the wave to force FRF and the force to motion FRF into an overall FRF of the vessel, i.e. from wave to motion, which is linear again.

1-3 Contents and Outline of this Thesis

Chapter 2 gives a more detailed problem description. First, the calculated motion RAOs of the SSCV Thialf are compared to the RAOs obtained from model tests. Subsequently we focus on the calculated and measured force RAOs on a captive submerged cylinder. This chapter ends with the explanation on the erroneous results.

Chapter 3 concerns a literature study. The main focus of this study is to gain more insight in similar problems and the applied methods. Several methods are compared to each other and subsequently a final method is chosen.

In **chapter 4** the chosen method is discussed in more detail. First, the general approach of the numerical model is given. The model is divided into two components: a radiation diffraction calculation and a time-domain simulation. The latter consists of two subcomponents: the Flow Module and the Motion Module. Both components are further elaborated on. Thereafter the main assumptions are being discussed, followed by an explanation of the coordinate systems. At the end of this chapter required software is stated.

After a brief introduction on radiation diffraction theory, **chapter 5** continues with the application of the radiation diffraction calculation. The main purpose of this calculation is to acquire the necessary boundary conditions and hydrodynamic coefficients for the chosen method. Two options are found which might be suitable to acquire this data. The data of both options will be used in the following time domain simulation.

The main emphasis of **chapter 6** is on the implementation of the first sub-component of the time domain simulation; the Flow Module. First a general description is given on various types of flow. Two implementations of fluid pressures are discussed in this chapter. This chapter ends with analytical flow cases for verification of the Flow Module.

Chapter 7 describes the second part of the numerical model; the Motion Module. The Motion Module solves the equations of motion using a numerical integration scheme. Firstly the input parameters are discussed, followed by a brief description of the integration scheme. Subsequently the Motion Module is validated by computing the motion response of a SSCV at transit draft. The resulting RAOs are compared with RAOs obtained from a radiation diffraction analysis. At the end the coupling is made with the Flow Module.

In **chapter 8** the numerical model is applied to a captive submerged cylinder. Firstly regular wave simulations are performed. The results are compared to in-house developed CFD results. Next, irregular waves are used to obtain force RAOs on the cylinder. Subsequently, the numerical model is applied to the SSCV Thialf at inconvenient draft. The full time-domain simulation is applied and the acquired motion RAOs are compared to model test RAOs.

In **Chapter 10** all the gathered conclusions of this research are summarized and the final recommendations are stated.

Chapter 2

Problem Description

This chapter gives more insight in the problem. Firstly, the calculated motion RAOs of the SSCV Thialf at 14.5 m draft are shown, together with the RAOs obtained from model tests. The main observations are discussed. To give more insight in the problem, we focus in more depth on a similar problem based on a submerged suction can. Model tests were performed whilst the suction can was held captive just below the water surface. In this case the conventional diffraction programs are not able to calculate the wave excitation forces on the cylinder, due to the small submergence. In-house developed CFD calculations are discussed to gain more insight.

2-1 Motion Response of the SSCV Thialf

Figure 2-1 shows the motion RAO for heave and roll of the SSCV Thialf at 14.5 m draft in beam waves. This draft corresponds to 0.9 m submergence of the pontoons. Both the RAOs acquired from model tests as from the radiation diffraction program WAMIT [1] are shown.

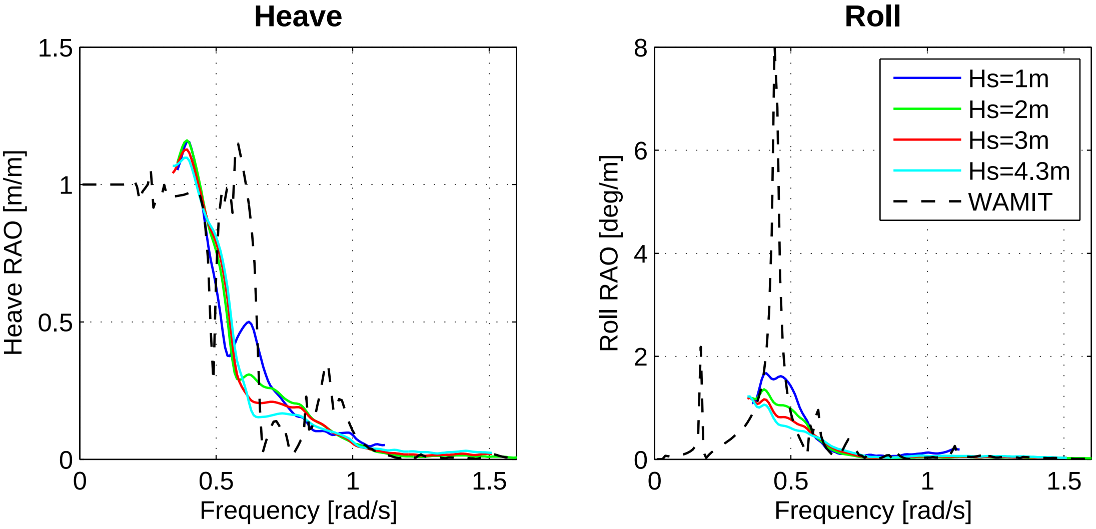

Figure 2-1: *Heave and roll RAO of SSCV Thialf at 14.5m draft in beam waves*

For heave it is clearly visible that WAMIT is not capable of reproducing the model tests RAOs. First of all, sharp and incorrect peaks are observed at various frequencies which are not present at the model test RAOs. Secondly, a wave height dependency is visible in the model test RAOs between 0.5 and 0.75 rad/s, whereas WAMIT shows the RAO for a unit wave only.

For roll motions two clear peaks can be observed in the WAMIT RAO. The lower peak around 0.2 rad/s corresponds to the natural frequency of the SSCV Thialf at 14.5 m draft. Unfortunately, this frequency is outside the range of the model test results such that comparison is not possible. Remarkable is the larger peak near 0.5 rad/s. This frequency corresponds to the natural frequency of the SSCV at transit draft. Visualization of the free-surface elevation of WAMIT at this frequency shows standing waves on top of both pontoons, between the columns. The standing waves on the port side and starboard pontoon are 90° out of phase with each other.

Focusing on the model test RAOs for roll, a wave height dependency is observed at this peak. For 1 m significant wave height, the peak in roll is slightly present. However, it is truncated just below 2 deg/m. For larger wave heights the peak disappears. This indicates that for small wave heights standing waves might be present on top of the pontoons, whereas for larger wave heights the standing waves are reduced due to viscous effects and non-linearities, e.g. wave breaking. Additionally, for larger wave heights the pontoons emergence from the water surface occasionally.

The model tests show that the motion RAO of the vessel becomes dependent on the wave height. Strictly speaking, it is therefore not allowed to use the term RAO anymore. An RAO gives the constant ratio between output and input, whereas the model tests show that the ratio varies for a varying wave height. Still, it is common to present the motion response in terms of RAOs, since is it a familiar technique and the results can be interpreted at a glance. In this research the term RAO is still used, whereby the corresponding wave height will be explicitly mentioned.

2-1-1 Hydrodynamic coefficients

To gain more insight in the force to motion response of the vessel, figure 2-2 shows the added mass and damping coefficients of the SSCV Thialf at inconvenient draft. The coefficients are obtained by WAMIT as well.

Both the added mass and damping coefficients show sharp peaks over the frequency range. The added mass coefficients even become negative at approximately 0.3 rad/s and 0.8 rad/s. The coefficients of the other modes, including the coupling terms, show similar peaks and negative values. This indicates that the force to motion FRF is incorrectly evaluated for the SSCV at inconvenient draft.

2-2 Force Response of a Captive Submerged Suction Can

Besides the incorrect evaluation of the force to motion FRF, it could be possible that the wave to force FRF is incorrect evaluated as well. To investigate this, we will focus

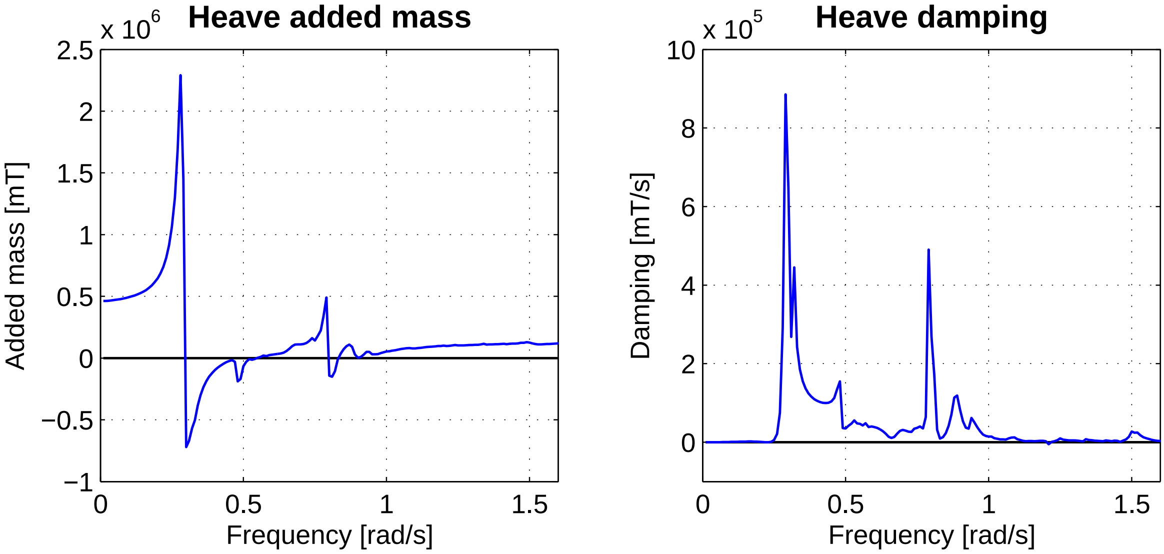

Figure 2-2: *Heave added mass and damping coefficients of SSCV Thialf at 14.5m draft*

in more detail on the force RAOs of a captive submerged suction can. These RAOs are obtained from model tests.

Several model test were executed with the suction can in an upright position just below the water surface. The full scale suction can had a diameter of 15 m and a height of 13 m. The submergence varied between 1 m, 3 m and 7 m, the significant wave height between 1 m, 2 m and 4 m and the peak period between 7 s, 9 s and 11 s. The variation in peak periods did not show distinctive results, such that the upcoming results are shown for a peak period of 9 s only.

The results for various wave heights and submergences are shown in figure 2-3. The obtained force RAO of WAMIT is included as well. Here, it should be noted that for the WAMIT calculation the geometry of a cylinder is used instead of a suction can. In-house research has indicated that this has insignificant effect on the results.

The left graph of figure 2-3 shows the vertical force RAO as calculated by WAMIT and obtained by model tests for the suction can/cylinder being 1 m submerged. Assuming the model test results to be correct, two observations can be made:

1. The radiation diffraction calculation strongly over predicts the measured force.
2. The model test force RAO is dependent on the wave height.

The former observation occurs at a frequency of 0.73 rad/s. Here the force per meter wave height is 7000 kN/m, whereas the model test for one meter wave height shows approximately 2500 kN/m. An over prediction of nearly 180%. The absence of any viscous effects in the radiation diffraction calculation might again contribute to the large over estimation.

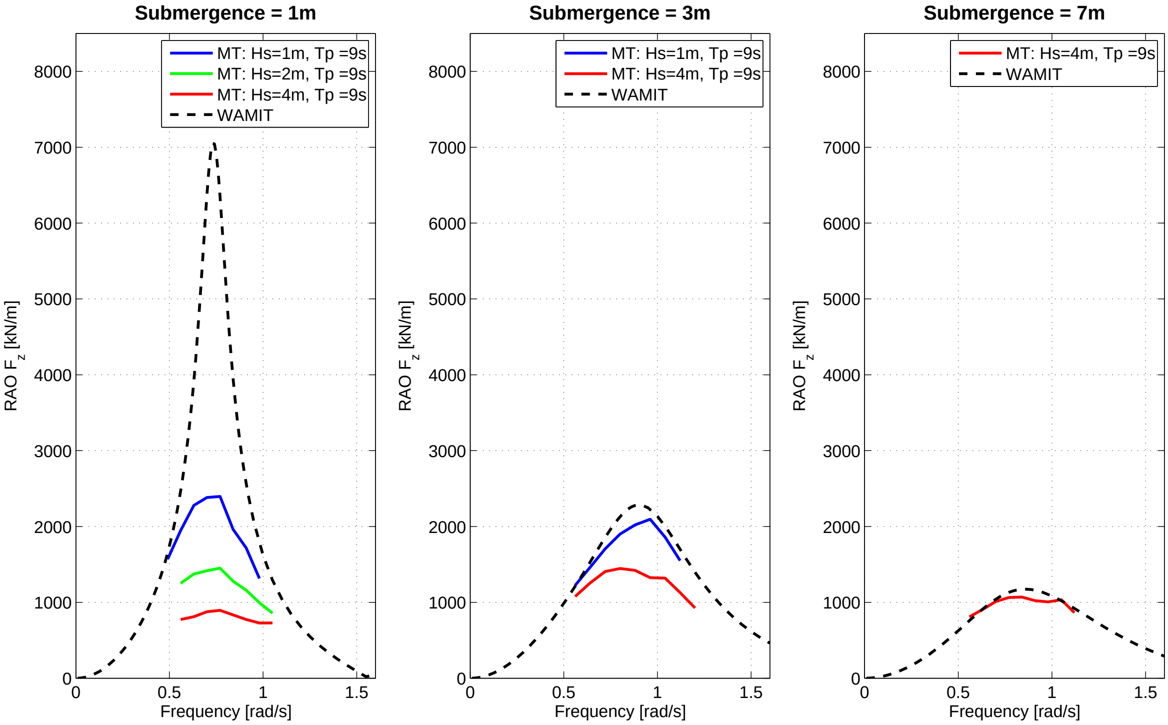

Figure 2-3: *Heave force RAO on a captive suction can for various wave heights*

The latter observation implies that non-linear effects are present which causes the RAO to be wave height dependent. Thus we can state that wave to force FRF is miscalculated by the radiation diffraction program as well.

Larger submergences

The middle and right graphs of figure 2-3 shows the same force RAOs on the suction can/cylinder for a submergence of respectively 3 m and 7 m. It can be seen that the peak in the force RAO calculated by WAMIT reduces drastically for increasing submergence depth. At 3 m submergence WAMIT approaches the model test result for 1 m wave height, however the wave height dependency is still present at 4 m waves.

At a submergence of 7 m the RAO calculated by WAMIT equals the model test results. This suggest that the possible presence of the non-linear effects slowly reduces for increasing submergence and clarifies why radiation diffraction calculations are valid for a SSCV at operational draft. Unfortunately, no model test at a submergence of 7 m and a wave height other than 4 m were done to confirm the absence of these non-linear effects.

2-3 Observed Fluid Behavior

During the model tests on the submerged captive suction it became clear that the waves break as soon as they enter the shallow water region on top. For larger wave heights also emergence of the top surface was observed. Similar and more clear observations on the fluid behavior can be made by using CFD simulations. These simulations are obtained by [2].

The simulations are performed using a captive submerged cylinder with the same diameter and height as the suction can. Both regular as irregular waves are used, with the (significant) wave height and (peak) period equal to the model test values. Four snapshots of regular wave simulations are shown in figure 2-4. Here the submergence, wave height and wave period were respectively 1 m, 4 m and 8.6 s.

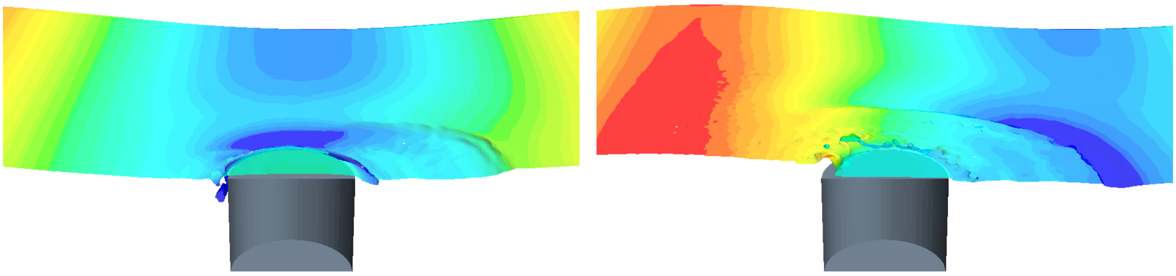

(a) *The top surface of the cylinder runs completely dry in a wave trough.*

(b) *The surface elevation at the leading edge increases due to the upcoming wave crest.*

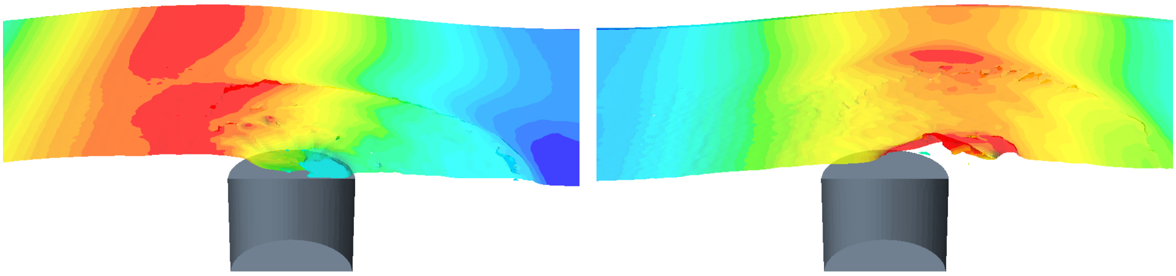

(c) *The wave breaks at the leading edge and a high velocity jet shoots over the cylinder.*

(d) *The high velocity jet meets the trailing edge water and a sort of pumping mode arises.*

Figure 2-4: *Four snapshots of a CFD simulation with a regular wave of 4m and a frequency of 0.73 rad/s.*

Strongly non-linear phenomena can be observed in the four snapshots. Figure 2-4a shows that the top surface of the cylinder runs dry in the wave trough, indicating a sudden change in water plane area. At the snapshots of 2-4b and 2-4c the fluid shows great resemblance between green water flow onto a deck and theoretical breaking dam problems. Whereas in figure 2-4d a small pumping mode may be seen at the trailing edge of the cylinder. For smaller wave heights, the animations show a more present pumping mode shifted slightly forward to the center of the cylinder (not shown here).

Visualization of the radiation diffraction calculations shows an extreme pumping mode on top of the cylinder at the same frequency of 0.73 rad/s. Here, the surface elevation on top is 6.6 m at a maximum for an incoming wave amplitude of only 1 m. Since the diffraction calculations give results in the linear frequency domain a negative elevation of 6.6 m on top occurs as well. This is physically incorrect since the submergence of the cylinder is 1 m.

For an SSCV at inconvenient draft similar kind of observations were done. At full scale it was observed that the waves on top of the pontoons became isolated from the surrounding sea, breaking waves were observed in the shallow water region and the pontoon emerged from the water occasionally. The radiation diffraction calculations show large standing waves on top of the pontoons.

2-4 Cause of the Erroneous Results

The radiation diffraction programs which are used to calculate wave forces and body motions are based on potential theory. The basics of potential theory are elaborated in more detail in appendix A. To use this theory in combination with waves, it is assumed that the surface slope or steepness of the waves is very small. This allows terms in the wave-equation with a magnitude in the order of the wave steepness-squared to be ignored, which simplifies the calculations drastically. As a result, the harmonic motions of the water particles and the harmonic pressures will have a linear relation with the wave surface elevation.

Radiation diffraction programs in turn calculate surface elevations for infinite small wave and motion amplitudes. Subsequently linearity is used to extrapolate the results to the preferred amplitude. For linear events this extrapolation is valid and results in correct wave forces and moments on the body and correct added mass and damping coefficients. However, for a submerged body in close proximity to the free surface, a relatively small layer of water is present on top of this body. In this case the underlying linear assumptions are not valid any more.

First of all the calculated results for infinite small waves are extrapolated to physically impossible values, like extreme surface elevations and pressures on the body. This results in incorrect added mass and damping coefficients and in incorrect wave forces and moments. Secondly the equations of motion are solved using the linear approach. In this case the stiffness terms are assumed to be constant, whereas the emergence of the body implies that it is not allowed to assume constant stiffness terms. These strongly non-linear phenomena make both the force FRF and motion FRF dependent on the wave height and causes the radiation diffraction programs to give erroneous results in these kind of situations.

Chapter 3

Literature Review

Prior to the development of the numerical model, a literature study is performed. The main focus of this study is to gain more insight in similar problems in literature and industry and to gain more insight in the already available methods. Several methods are discussed, after which some additional methods are further elaborated on. At last, the final method is determined which is used during this research.

3-1 Similar Problems and the Applied Methods

Heerema Marine Contractors is not the only company dealing with problem. Already in 1999 [3] did research on the motion behavior of the Enforcer Series. These amphibious support vessels have a stern dock which creates a sheltered environment for the deployment of landing craft up to Sea State 4 conditions. In order to receive the landing craft the vessel is ballasted, slightly trimmed backward and the stern door is opened resulting in a layer of water inside the stern dock of about 2 m. [3] encountered large standing waves inside the dock in case use was made of the conventional radiation diffraction calculations. These waves were not observed during the accompanying model tests. Finally a multi-domain approach was used for the radiation diffraction calculations to avoid the erroneous results. A clear explanation of this approach including several applications is given by [4]. A short summary is included in appendix A-3. The multi-domain approach turned out to be a good method in calculating vessel motions, however only in case extra damping was added inside the dock. Similar results were found in [5], which did a hydrodynamic analysis of king size transport vessels at open seas.

[6] also made use of the multi-domain approach for assessing the hydrodynamic behavior of heavy marine transport vessels during offshore loading and discharge. Although this research focuses more on the gap flow between the heavy marine transport vessel and its cargo, the same method at the submerged deck of the vessel were no cargo is present is applied. Furthermore it was noted that the suitability to apply potential theory largely depends on the water level above the submerged deck, which is in line with the model test results of figure 2-3.

[7] used the CFD program ComFLOW to calculate wave loads and internal loads on a semi-submersible at shallow (inconvenient) draft. The wave loads were derived from captive CFD simulations and were compared with both linear diffraction theory as the model test results. The CFD simulations showed reliable results for a captive body at both operational as shallow draft. On the other hand, long computational times were required for the simulations. At the time of the performed research, the ComFLOW software was not yet fully compatible with moving body simulations. Boundary conditions used for the captive simulations could not be applied and finally a numerical beach was used, resulting in a significant increase in computational time.

[8] did research on the same submerged cylinder as discussed in section 2-2. First a parameter study was performed to get a better understanding on the erroneous results of diffraction calculations. Thereafter it was investigated the use of a damping lid in the diffraction calculations to suppress extreme water elevations. This showed that the peak in the force RAO reduces significantly for an increasing damping value. A proper damping value was based on literature and the model test RAOs for 1 m waves. The wave height dependency was not captured with the fixed damping value and various values dependent on the wave height were stated. However, even for the maximum damping value the force RAO was still over predicted for 4 m waves. Therefore a new method was developed to be able to capture the non-linear behaviour of the force RAO. This method, named TiDoFin, requires a previously determined database of force RAOs for various submergences. Subsequently the instantaneous water height on top of the submerged body is determined and the time averaged force for a given wave height and wave frequency is provided. TiDoFin captured the non-linear behavior in the wave force, however in case the database was created using the undamped RAOs the force was still over predicted. By again making use of a damping lid and a carefully selected damping values RAO database, the TiDoFin calculations showed good occurrence for the submerged cylinder.

[2] also performed an CFD analysis on the submerged cylinder using the software STAR-CCM+ by CD-Adapco. Simulations were done using both regular as irregular waves and turbulent, laminar and inviscid flow was applied to evaluate what flow phenomena was important. For regular waves the same wave height was chosen as the significant wave height from the model tests. Although the correctness of comparing the results for regular waves with irregular waves for non-linear events is questionable, good results were found in general for the 2 m and 4 m regular waves. The peak in the 1 m wave RAO was unpredicted by CFD. The force RAOs obtained using irregular waves showed better agreement with the model test RAOs. Disadvantage of the simulation including irregular waves is the computational time involved. One irregular wave simulation of 20 minutes took 43 hours computational time, about 20 times longer then a regular wave simulation. In spite of the long computational time involved, the works showed that it is possible to accurately compute wave force RAOs on a submerged captive body close to the free surface.

[9] continues to verify whether CFD is able to predict the motions of an SSCV at survival draft. First the SSCV Thialf at a deep draft was selected to validate the used approach. Several regular wave simulations were done including a 2 m wave and various

wave frequencies to build the RAOs. Good agreement between potential theory and CFD was found for heave and to a slightly lesser extend also for pitch. For roll motions CFD showed a much more damped RAO. Several simulations were redone for a wave height of 8 m which is more in line with performed model tests. Both the peak in the heave and pitch RAO were reduced to values close to the model test RAOs. This shows that even the motion RAOs of the SSCV Thialf at operational draft are not linear with the wave height. The work continues with the SSCV at survival draft. This includes about 3 m water on top of the pontoons. The wave height for all simulations was kept on 2 m again, such that the pontoon practically remains submerged at all times. The heave and pitch responses showed similar trends as the response obtained from model tests. The roll response is over predicted over almost the entire frequency range, but shows far better results than potential theory does. Based on the results it can not yet be concluded if CFD is able to predict the response of an SSCV at inconvenient draft. Only one wave-draft combination is simulated, where the pontoon remained submerged. Larger wave and smaller draft combinations are stated as future work.

3-2 Alternative Methods

Within the industry, several methods based on multi-domain diffraction and CFD are already used to calculate forces and motions of submerged bodies in close proximity to the free surface. However, there are alternative methods available. Smooth Particle Hydrodynamics (SPH) for example is a computational method used for simulating fluid flows. It divides the fluid into a set of discrete elements, referred to as particles. As opposed to CFD, this guarantees conservation of mass without extra computation since the particles themselves represent mass. It was developed in the seventies initially for astrophysical problems, but nowadays it is used in many other fields. In the offshore and civil environment it is starting to show itself at, amongst other areas, green water predictions and dam break problems, see for example [10] and [11]. Furthermore SPH provides real time simulation and very smooth looking animations and therefore lends itself perfectly for visual applications, such as virtual sugary, video games and animations.

Another alternative method is conceived within HMC itself and documented in an internal design brief [12]. This design brief focuses on a SSCV at inconvenient draft but can basically be applied on any submerged body. The method regards the shallow water region on top of the submerged body as a free flooding tank. Each time step the amount of water inside the tank is calculated.This water exerts a force on the top surface of the body. The forces on the remaining wetted surface of the body is acquired using results from a radiation diffraction analysis. Since this method regards the volume on top of the pontoon as a one or more flooding tanks, the method is referred to as the Free Flooding Tanks (FFT)-method from now on.

3-3 Method Selection

In summary several methods are already used to calculate forces and motions of submerged bodies in close proximity to the free surface. Including the additional method from section 3-2, the following selection can be made:

- Multi-Domain Diffraction (MDD)
- Computational Fluid Dynamics (CFD)
- Smooth Particle Hydrodynamics (SPH)
- Free Flooding Tanks (FFT)

CFD seems to be capable of predicting the correct behavior. However, a full CFD analysis to predict the motion behavior of a SSCV in an irregular sea state is (as yet) too computational expensive in terms of time and memory. The same holds for SPH, whereby at this scale and for this application the method seems to be in its infancy. This leaves two methods to be most promising: MDD and FFT. A overview of these two is given in table 3-1 hereafter:

Table 3-1: *Overview of multi-domain diffraction and free flooding tank.*

	Multi-Domain Diffraction	**Free Flooding Tanks**
Software	DELFRAC	-
Domain of Analysis	Frequency Domain	Time Domain
Shallow Water Region	Wave Effects	Still Water in Tanks
Emergence of Body	Not Possible	Possible

In case of MDD calculations are done with the radiation diffraction program DELFRAC, developed by the Delft University of Technology. This is the only program which allows the use of multiple domains in 3D radiation diffraction calculations. In case of the FFT-method one is basically free to choose any software package for the radiation diffraction calculation. The same applies for the implementation of the flooding tanks.

An important distinction between the two methods is the way they treat the shallow water region on top of the submerged body. The MDD takes into account wave effects on top of the body in the form of disturbances from the surrounding region. Although this approaches reality most, it is questionable whether this is correct since it still uses the small wave height assumption and linear waves. The FFT assumed still water within the tanks. It approaches reality less but simplifies the time domain calculations drastically.

Major disadvantage of the MDD-method is the analysis performed solely in the frequency domain, which does not make it possible to take any non-linearities into account. The linear assumptions made in the radiation diffraction programs do not allow any change in water plane area and wetted surface of the body. Thus inclusion of emergence of the body is not possible here. The wave height dependency might be captured by restricting the velocities and pressures on the boundary between the two domains. This restricting implies to be a function of the wave height, submergence depth and possible other variables. However [8] showed that no clear relation is present between these variables and the erroneous results of the radiation diffraction calculations. Emergence of the body is captured by the FFT-method in the form of empty tanks which does not exert any force on the body.

The use of linear waves on top of the body and especially the absence of the ability to include any emergence of the body has led to the rejection of the Multi-Domain Diffraction method and the adoption of the Free Flooding Tank method.

Chapter 4

Methodology

A free flooding tank approach is used in order to capture the non-linear behaviour of a body at inconvenient draft as described in chapter 2. In this approach, the shallow water region on top of the submerged body is defined as a free flooding tank, as shown in figure 4-1. The water inside the free flooding tank exerts a static force on the top surface of the body. Additionally an inertia force is present in case the water mass is accelerated by the body. The diffraction and radiation forces on the remaining wetted surface of the body will be acquired using the results of a previously executed radiation diffraction analysis.

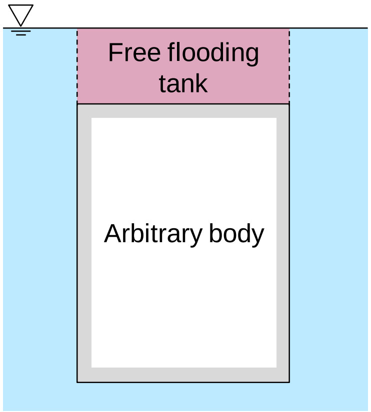

Figure 4-1: *Location of a free flooding tank*

The motions of the body are obtained during a time-domain simulation. During this simulation the equations of motion are solved numerically using a Runge-Kutta scheme. This is done in the main script of the numerical model, called the Motion Module. In order to solve these equations of motion, the force exerted on the body by the flooding tank is required. This force component is calculated by a Flow Module. Each time step the orientation of the body (and thus of the flooding tank) is passed onto the Flow Module. Subsequently the fluid pressure inside the tank and the fluid pressure acting on the outside are acquired. The resulting fluid flow due to a pressure difference is obtained by making use of the Bernoulli equation. Both the force exerted on the body by the new tank filling grade and the tank mass are returned to the Motion Module. Here, the retardation functions are evaluated and the equations of motion are solved to acquire the new orientation of the body.

In this chapter the methodology of the numerical model is elaborated for a general body, which could then be applied on both a cylinder as an SSCV. First the total fluid domain is considered, which is divided into two sub-domains. This chapter continues with a more detailed description of the numerical model. Firstly the equations of motion as used in the Motion Module are elaborated on. Then the purpose and the requirements of the radiation diffraction analysis are discussed, followed by the time-domain simulation including the Motion and Flow Module. Subsequently the main assumptions are elaborated, followed by the involved coordinate systems. This chapter ends with stating the required software.

4-1 Domain splitting

Suppose we have the same arbitrary body located just below the water surface, as mentioned in the introduction of this chapter. This body can be considered as, for example, the side view of a submerged cylinder or the cross section of a pontoon somewhere between two columns. The submergence results in a small layer of water being present on top of the body. In this case the total fluid domain surrounding the submerged body can be split into two sub-domains; an outer domain and one or more tank domains, see figure 4-2. An interface is present between the inner and outer domain.

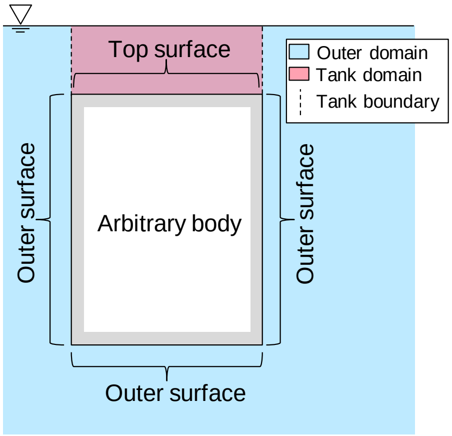

Figure 4-2: *Domain definition for an arbitrary body.*

4-1-1 Sub-domains

The *outer domain* consists of all the water surrounding the body, except for the water on top. The body's surface area that adjoins the outer domain is referred to as the *outer surface*. Forces exerted by the fluid on the outer surface are acquired in advance by a radiation diffraction analysis.

A *tank domain* is located above the submerged horizontal top surface of the body. In case of a submerged cylinder this will result in one tank domain, in case of a SSCV at inconvenient draft this will result in two tank domains, namely on top of each pontoon. The surface area of the body adjoining the tank domain is referred to as the *top surface*. Each tank domain consists of one or more free flooding tanks. The water inside the tanks is assumed to be still water. As a result, a hydrostatic pressure distribution can be considered here. The force on the top surface is exerted by the water inside the free flooding tanks. A static force is present due to the weight of the water. Additionally an inertia force is present in case the water mass is accelerated by the body, i.e. added mass of the tanks.

4-1-2 Flow between domains

An interface is present between the outer domain and the tank domain and is referred to as the *tank boundary*. This tank boundary represents the submerged side of the free flooding tank. Communication between the two domains reflects itself as a fluid flow from one domain to the other.

The flow is generated by a pressure difference at each side of the boundary. At the tank side the fluid pressure follows from the tank water level. At the outer side the pressure is imposed by the fluid in the outer domain and consists of a static and a dynamic component. The former follows from the local surface elevation, the latter from the presence of the waves. Both outer components are obtained from the same radiation diffraction analysis as was used to determine the forces exerted on the outer surface. Since the components are determined in advance and imposed at the tank boundary, the pressures at the outer side are considered as boundary conditions of the flooding tank.

4-2 General Approach

In the introductory chapter of this work is was stated that, in general, the motion behavior of a vessel is indicated with the frequency-domain equations of motion. Whereas in chapter 2 it was observed that both the force FRF and the motion FRF were incorrectly calculated by making use of this approach due to the non-linearities involved.

Therefore the numerical model makes use of adjusted equations of motion. Here, the loads on the entire wetted surface of the body are subdivided into loads on the outer surface and loads on the top surface. In addition, the equations are solved in the time-domain such that the non-linearities can be taken into account. The adjusted equations of motion are stated as:

$$M\ddot{\vec{x}}(t) = \vec{F}^*_{diff} + \vec{F}^*_{rad} + \vec{F}_{rest} + \vec{F}_{tank} \tag{4-1}$$

Here, M is the mass matrix of the body and $\ddot{\vec{x}}(t)$ indicates the time varying acceleration for each degree of freedom. Furthermore, $\vec{F}^*_{diff}$ and $\vec{F}^*_{rad}$ are respectively the wave forces and moments and the radiation forces and moments specifically on the outer surface of the body, $\vec{F}_{rest}$ are the conventional hydrostatic spring terms and $\vec{F}_{tank}$ are the forces and moments exerted by the flooding tanks on the top surface of the body. The latter force consists of two components; a static component $\vec{F}_{st}$ due to the weight of the water and a dynamic component due to inertia of the water:

$$\vec{F}_{tank} = \vec{F}_{st} - M_t\ddot{\vec{x}} \tag{4-2}$$

in which M_t is a six-by-six matrix including the mass of each tank. In order to solve equation (4-1), the numerical model is split into the following two distinct parts:

1. Radiation Diffraction Analysis
2. Time-Domain Simulation
   a. Motion Module
   b. Flow Module

In the upcoming two subsections, a brief description is given on these two parts. Here it is stated what the purpose of the specific part is, what is required to use it and what the internal steps are within the part.

4-2-1 Radiation diffraction analysis

The radiation diffraction analysis is used to acquire the wave forces and moments $\vec{F}^*_{diff}$ and radiation forces and moments $\vec{F}^*_{rad}$ on the outer surface of the body. Subsequently $\vec{F}^*_{rad}$ is used to obtain the added mass and damping coefficients. In addition, the analysis is used to acquire the surface elevation and dynamic fluid pressure at the outer side of the tank boundary. These latter two items are considered as the boundary conditions of the flooding tanks and are required in the Flow Module. The details of the radiation diffraction analysis are discussed in chapter 5. The flow chart of the analysis is included in figure 4-3:

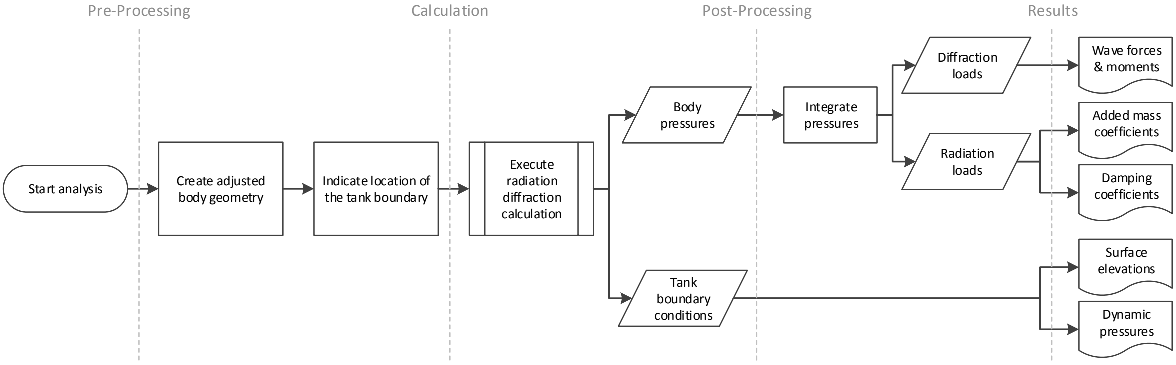

Figure 4-3: *Flow chart of the radiation diffraction analysis.*

The first step in the analysis involves the creation of an adjusted body geometry. This adjustment is required to exclude the top surface of the body, since we are interested in $\vec{F}^*_{diff}$ and $\vec{F}^*_{rad}$, which are specified on the outer surface only. Furthermore it is required to indicate the location of the tank boundary, such that the boundary conditions are acquired specifically at this location. Adjusting the body geometry and indicating the tank boundary can be considered as pre-processing.

The second step in the analysis is the actual radiation diffraction calculation. This calculation provides the diffraction and radiation pressures on the outer surface of the body. Furthermore, the boundary conditions (surface elevations and pressures) at the previously indicated tank boundary are retrieved.

The third and last step is post-processing of the acquired data. Here, the pressures on the outer surface are integrated over the accompanying surface area. This results in the diffraction and radiation loads. The former indicate the wave forces and moments. The latter are split into a part in-phase with the acceleration of the body and a part in-phase with the velocity of the body, i.e. the added mass and damping coefficients.

4-2-2 Time-domain simulation

The time-domain simulation consists of two modules. The first module is the Motion Module which evaluates the retardation functions and solves equation (4-1) numerically. Each time step the second module is called to calculate the static force exerted by the flooding tanks on the top surface and to obtain the added mass of the tanks. This is done in the Flow Module.

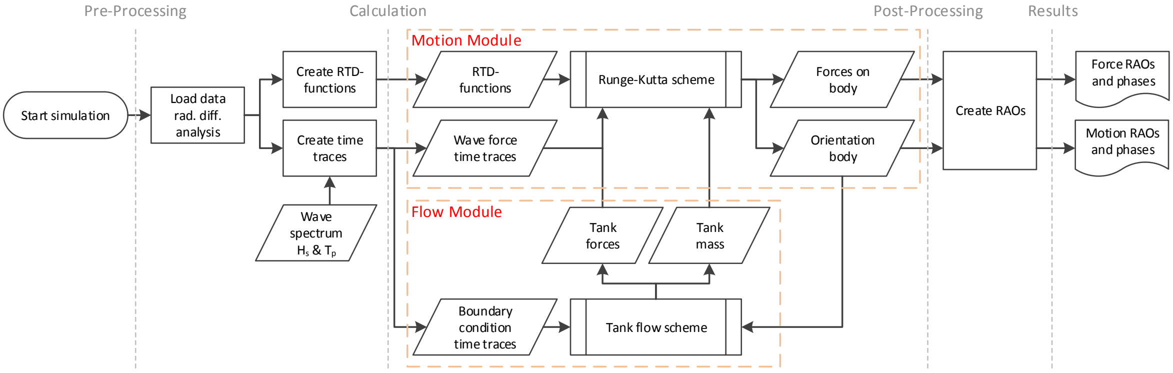

Figure 4-4: *Flow chart of the time domain simulation including the Motion and Flow Module.*

In order to run the time-domain simulation, pre-processing is required. The wave forces and moments on the outer surface and the tank boundary conditions are obtained from the radiation diffraction analysis. As a consequence these quantities are provided in the frequency-domain and need to be converted to the time-domain. This is done by making use of a wave spectrum and applying an inverse Fourier Transform. Converting to the time-domain results in a time trace of:

- the wave load for each of the six degrees of freedom;
- the pressure distribution on the outer side of the tank boundary;
- the surface elevations at the outer side of the tank boundary.

In case of a freely floating body, the added mass and damping coefficients are used to obtain the frequency independent added mass and retardation functions for the damping.

Motion module

The Motion Module solves the equations of motion from (4-1). Firstly, the orientation of the body for the given time step is passed onto the Flow Module. The static tank forces and the added mass of the tanks are returned. The wave forces and moments on the outer surface are acquired from the wave load time traces.

Subsequently, an in-house developed script based on a 4^{th} order Runge-Kutta scheme is used. This script evaluates the retardation functions and solves the equations of motion for a given time step. Output is the total force on the body and the new orientation of the body. The latter is passed onto the Flow Module again during the new time step.

Flow module

In case free flooding tanks are defined, the Flow Module is called at the beginning of each time step.

Firstly, the current submergence of the tank boundary is calculated from the orientation of the body and the surface elevation time trace. This submergence leads to a static pressure on the outer side. The dynamic pressure on the outer side follows from the pressure time trace. Combining both components results in the total outer pressure at the tank boundary. The pressure distribution on the inner side follows from the current tank filling grade.

Subsequently, the flow velocity is calculated from the difference in pressure at each side of the tank boundary. Here, the Bernoulli equation is used. By integrating the velocity over the area of the tank boundary, the total discharge is acquired. The total volumetric flow is obtained by multiplying the discharge with the time step.

This sequence is repeated for each tank. As soon as each of the new tank filling grades is determined, the total hydrostatic force on the top surface of the body is obtained. Both the tank forces and the mass of each tank is passed onto the Motion Module.

4-3 Main assumptions

Based on the general principles as stated in section 4-1, the following main assumptions are made for the numerical model:

Waves are unaffected

Water flows of the top surface of the body as soon as the body emerges. Both model tests and CFD simulations clearly show that this water affects the waves in the vicinity of the body. In the numerical model it is assumed that waves in the outer domain are not affected by water flowing into and out of the free flooding tanks.

Uncoupled force components

It is assumed that fluid pressures in the outer domain are not affected by the fluid pressures in the tank domain. In combination with the first assumption, this leads to the resulting fluid pressure in the outer domain to be the hydrostatic and wave-induced dynamic pressure only. As a result the forces on the outer surface are induced by waves in the outer domain only. Since this force component is uncoupled from the tank domain, it can be obtained separately from the force exerted on the top surface.

The latter force is exerted by the water in the tanks, which in turn varies over time due to in and outflow of tank water. In section 4-1-2 it is stated that this flow follows from the difference in outer and inner pressure at the tank boundary. Since the outer pressure on the boundary is imposed by the incoming waves, the tank force is *not* uncoupled from the pressure field in the outer domain.

Still water

The water inside the tanks is considered as still water, such that the water surface within the tanks remains horizontal (earth fixed) at all times. As a result a hydrostatic pressure distribution is present in the tanks. Therefore, the fluid inside a tank only exerts a vertical force on the body due to gravity. Any other effects, e.g. sloshing are neglected.

Horizontal tanks

In case of a freely floating body the tanks will get a certain inclination angle based on the roll and pitch angle of the body, see figure 4-5a for roll.

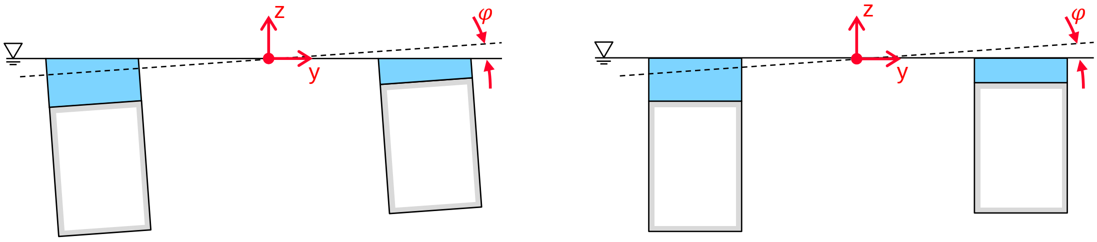

(a) *Inclined Tanks* **(b)** *Horizontal Tanks*

Figure 4-5: *Orientation of the tanks for a body with a roll angle φ.*

As a consequence the Center of Gravity (CoG) of the tank water shifts from its initial position and the pressure distribution at the top surface of the body changes. It is assumed that the flooding tanks remain horizontal (earth fixed) at all times, as shown in figure 4-5b. A few simplifications arise due to this assumption. Firstly, an equal tank level in the entire tank is present. This results in a constant pressure distribution at the top surface of the body. Secondly, no fluid flow is generated by an inclined base plane. Thirdly, the mass of water inside the tanks does not rotate about an axis passing through theCoG of the mass. Therefore no moment of inertia with respect through this axis is present. Note that the mass of water still has to rotate around the axis through the CoG of the vessel.

Zero forward speed

Although it is mentioned in the introduction and problem description of this research that the inconvenient draft could occur for a SSCV in transit, it is assumed that the SSCV has zero forward speed at all times.

4-4 Coordinate Systems

The motions of a body can be split into three (mutually perpendicular) translations of the CoG and three rotations around the CoG. Three right-handed coordinate systems are used within the numerical model, as shown in figure 4-6. These coordinate systems are used to define the body motions, excitation forces and moments and flooding tank properties.

Earth Fixed Coordinate System $E(X, Y, Z)$
The main coordinate system is the Earth Fixed Coordinate System. The (X, Y)-plane lies at the still water surface and the positive Z-axis is directed upwards. The position of the body is denoted in this system. The direction of the incoming wave μ is measured with respect to the the positive (X)-axis. $\mu = 0°$ for following waves, $\mu = 90°$ for starboard beam waves and $\mu = 180°$ for head waves.

Body Fixed Coordinate System $S(x, y, z)$
This coordinate system is fixed to the body with the origin S located above the center of buoyancy (CoB) of the body. If the body is floating upright then the positive z-axis is directed upwards and y is pointing to the port side of the body. At the initial position the origin S is located at the origin E (not shown in figure 4-6 for clarity). Furthermore, the hydrodynamic origin of WAMIT is defined at the body fixed origin S. All input and output from WAMIT is defined with respect to S. Next to the hydrodynamic origin, the position of each flooding tanks is defined in this coordinate system.

Tank Fixed Coordinate System $T(x_t, y_t, z_t)$
Each flooding tank will have its own local coordinate system T^N, where N is the tank number. The origin is located at the bottom surface of the tank at a position specified by $\vec{r}_t$ in the Body Fixed Coordinate System $S(x, y, z)$. The (x_t, y_t, z_t)-axis have the same orientation as the (x, y, z)-axis at all time. The water level in each tank is measured with respect to the tank fixed coordinate system. Only one Tank Coordinate System is shown in figure 4-6 for clarity.

4-5 Software

The radiation diffraction calculation is conducted within WAMIT. A hydrodynamic code developed for the linear analysis of the interaction of surface waves with various types of floating and submerged structures. For post-processing of the WAMIT results use is made of MATLAB.

For the time-domain simulation the choice is made to program the entire code of both modules in MATLAB as well. First of all this ensures ultimate freedom and no restrains of "black box" software, secondly because it is manageable within HMC since both knowledge and the software itself is already available and thirdly because the author of this thesis has experience with it.

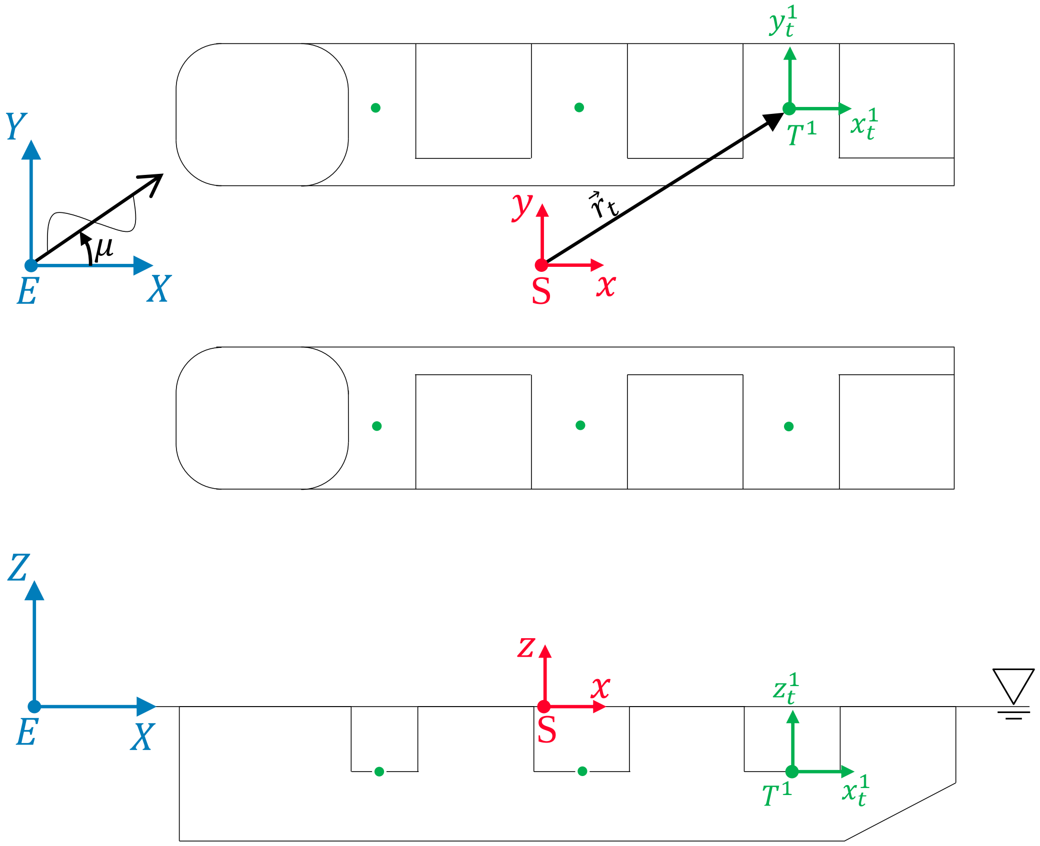

Figure 4-6: *Coordinate systems used in the numerical model, applied on a SSCV.*

Table 4-1: *Motions of a body*

DoF	Name	Describtion	Position and orientation	Force and moment
1	Surge	Motion in x-direction	x [m]	F_x
2	Sway	Motion in y-direction	y [m]	F_y
3	Heave	Motion in z-direction	z [m]	F_z
4	Roll	Rotation around the x-axis	ϕ [rad]	M_x
5	Pitch	Rotation around the y-axis	θ [rad]	M_y
6	Yaw	Rotation around the z-axis	ψ [rad]	M_z

Chapter 5

Radiation Diffraction Analysis

A radiation diffraction analysis needs to be performed to acquire two essential types of input for the time domain simulation. Firstly to determine the necessary hydrodynamic data (i.e. the wave forces and moments and the added mass and damping coefficients) on the outer surface of the body. Secondly the analysis is done to acquire the tank boundary conditions (i.e. the pressure on and surface elevation at the tank boundary).

The radiation diffraction analysis will be performed with the hydrodynamic software WAMIT. This software is developed for the linear analysis of wave interactions with various types of floating and submerged bodies. Since it is usually not possible to give an analytical description of the body's surface, WAMIT makes use of a discretized description of the surface. This is done by an ensemble of connected four-sided facets, or panels, which is called a panel model. The panels are in general quadrilaterals but could degenerate to a triangle when the coordinates of two vertices coincide. Figure 5-1 shows a panel model of the 1 m submerged cylinder.

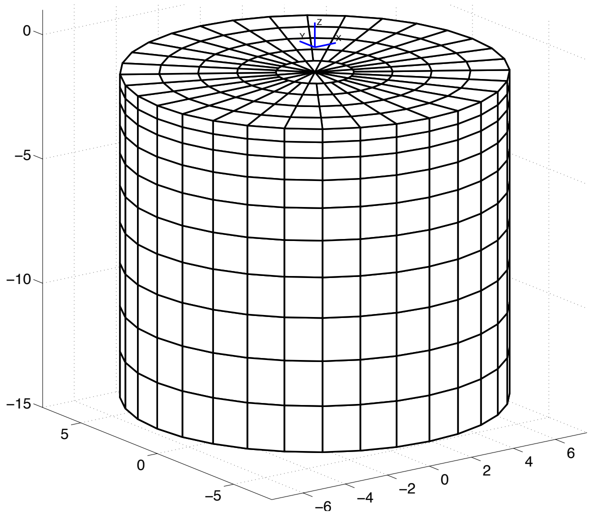

Figure 5-1: *Panel model of the 1m submerged cylinder.*

WAMIT uses potential theory to generate the hydrodynamic data on the body. Firstly it solves the radiation and diffraction velocity potentials on the body for the specified modes, frequencies and wave headings. Subsequently is computes global quantities including the first-order (and second) forces, added mass and damping coefficients and motions. WAMIT may be used to generate the hydrodynamic data directly, however in this case two problems are encountered for the numerical model:

1. WAMIT provides the hydrodynamic data for the entire surface of the body, whereas we are interested in the outer surface only.
2. The erroneous data of the top surface influences the data on the remaining surface.

The former problem is elaborated in section 5-1. The latter will be covered in the sections 5-2 to 5-5. Acquiring of the boundary conditions is discussed in 5-6.

5-1 Pressure integration

The first-order wave forces and moments on a body, induced by an incoming wave with frequency ω and heading μ, are generally calculated by integrating the diffraction pressure $p_d(\omega, \mu)$ over the submerged body surface S [13]:

$$\vec{F}_w(\omega, \mu) = \iint_S p_d(\omega, \mu)\vec{n}dS \tag{5-1a}$$

$$\vec{M}_w(\omega, \mu) = \iint_S p_d(\omega, \mu)\left(\vec{r} \times \vec{n}\right)dS \tag{5-1b}$$

in which $\vec{n}$ is the inward normal vector on the surface dS and $\vec{r}$ is the position of the surface dS in the body fixed coordinate system. The pressure $p_d(\omega, \mu)$ includes both the pressure induced by the incoming undisturbed waves and the pressure induced by the diffracted waves on the body being fixed.

To acquire the wave forces on the outer surface only, use is made of an option within WAMIT to output the complex valued diffraction pressures for each panel separately. This makes it possible to integrate the pressure over specifically selected panels only. As a result the wave forces and moments exerted on these areas only are acquired. Thus, by selecting a specific set of panels $S_o = \{1 \ldots \mathrm{K}\}$ containing only the panels associated with the outer surface, the wave forces and moments on the outer surface are acquired. In discretized form (5-1) then reads:

$$\vec{F}_w(\omega, \mu) = \sum_{k=1}^{K} p_{d,k}(\omega, \mu)A_k\vec{n}_k \tag{5-2a}$$

$$\vec{M}_w(\omega, \mu) = \sum_{k=1}^{K} p_{d,k}(\omega, \mu)A_k\left(\vec{r} \times \vec{n}\right)_k \tag{5-2b}$$

Here A_k is the area of panel k and the term $p_{d,k}(\omega, \mu)$ is the diffraction pressure on panel k due to an incoming and diffracted wave with frequency ω and heading μ.

The added mass and damping coefficients follow from the radiation forces and moments, which in turn are induced by the fluid around an oscillating body in still water. These forces and moments are obtained in a similar way as the diffraction forces and moments shown in (5-1), whereas the radiation pressure p_r is not dependent on the wave heading μ but on the oscillation mode j. By selecting the same set of panels S_o in the pressure integration, the radiation forces and moments on the outer surface are obtained. A slightly different notation for the discretized form is used here:

$$\vec{F}_{r_j}(\omega) = \sum_{k=1}^{K} p_{r_j,k}(\omega) A_k \vec{n}_k \quad \text{for} \quad j = 1 \dots 6 \tag{5-3a}$$

$$\vec{M}_{r_j}(\omega) = \sum_{k=1}^{K} p_{r_j,k}(\omega) A_k \left(\vec{r} \times \vec{n}\right)_k \quad \text{for} \quad j = 1 \dots 6 \tag{5-3b}$$

Here $\vec{F}_{r_j}$ and $\vec{M}_{r_j}$ are three-component column vectors containing respectively the complex valued radiation force in x, y and z-direction and the radiation moment around the x, y and z-axis, caused by a harmonic oscillation of the body in direction j. The term $p_{r_j,k}(\omega)$ is read as the radiation pressure on panel k due to a harmonic oscillation in direction j with frequency ω.

To obtain the added mass and damping coefficients from (5-3), some additional steps are required. Firstly the vectors $\vec{F}_{r_j}(\omega)$ and $\vec{M}_{r_j}(\omega)$ are gathered into a six-by-six radiation load matrix $\mathbf{L}$:

$$\mathbf{L}(\omega) = \begin{pmatrix} \vec{F}_{r_1} & \vec{F}_{r_2} & \cdots & \vec{F}_{r_6} \\ \vec{M}_{r_1} & \vec{M}_{r_2} & \cdots & \vec{M}_{r_6} \end{pmatrix} \tag{5-4}$$

Then a unit oscillatory motion of the body in six degrees of freedom with frequency ω is defined:

$$\vec{x}(\omega) = \vec{x}_a e^{i\omega t} \tag{5-5}$$

where the subscript a denotes the amplitude, such that the velocity and acceleration of this oscillation are given by:

$$\dot{\vec{x}}(\omega) = i\omega \vec{x}_a e^{i\omega t} \tag{5-6}$$

and

$$\ddot{\vec{x}}(\omega) = -\omega^2 \vec{x}_a e^{i\omega t} \tag{5-7}$$

Subsequently, the radiation load matrix can be split into a part being in-phase with the acceleration of the body and a part being in-phase with the velocity:

$$\mathbf{L}(\omega) = -\mathbf{A}\ddot{\vec{x}}(\omega) - \mathbf{B}\dot{\vec{x}}(\omega) \tag{5-8}$$

Substituting (5-4), (5-6) and (5-7) into (5-8) and splitting the real and imaginary part gives respectively the frequency dependent added mass $\mathbf{A}$ and damping $\mathbf{B}$ matrices:

$$\mathbf{A}(\omega) = \operatorname{Re}\left(\frac{\mathbf{L}(\omega)}{\omega^2}\right) \tag{5-9}$$

$$\mathbf{B}(\omega) = -\operatorname{Im}\left(\frac{\mathbf{L}(\omega)}{\omega}\right) \tag{5-10}$$

5-2 Adjusted Panel Models

To acquire the hydrodynamic data on the body's surface adjacent to the outer domain, the original panel model of the cylinder might be used in the radiation diffraction calculation to obtain all the panel pressures. Subsequently the set S_o contains only the panels associated with the cylinder's outer surface (white panels in figure 5-2a) and the top surface panels (red in figure 5-2a) are disregarded in the pressure integration. This will results in the hydrodynamic data on the body's outer surface.

Research by [8] however has shown that the pumping mode which arises due to the presence of the top surface panels, influences the remaining panel pressures in such a way that even erroneous pressures are obtained on the bottom surface panels. As a consequence the original panel model is not suitable for providing the hydrodynamic data on the outer surface. Therefore an adjusted panel model of the body will be used to obtain the outer surface data. Several geometries are compared with each other to determine which of them could approach the original hydrodynamic data best. The 1 m submerged cylinder is used in this comparison as the reference case and only surge and heave degrees of freedom are examined. An overview of adjusted panel models is given in figure 5-2b to d below.

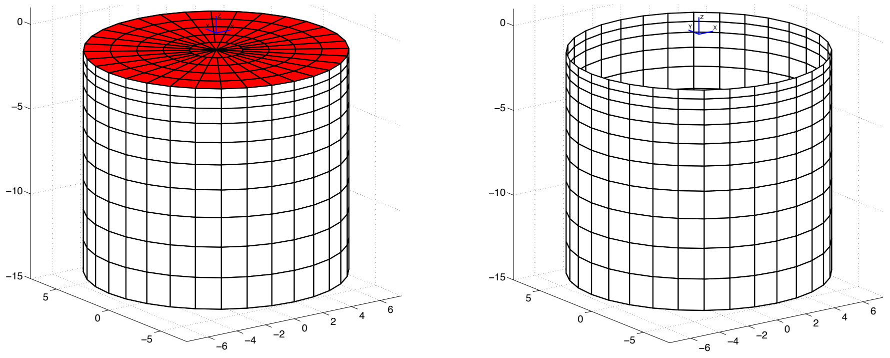

(a) *Original model* **(b)** *Dipole panel model*

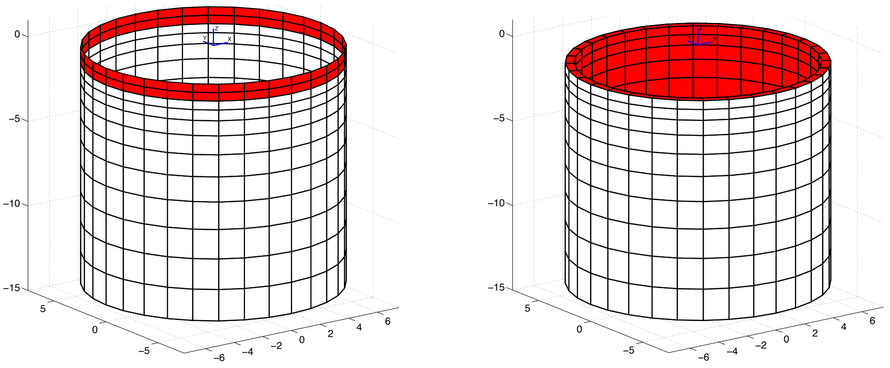

(c) *Raised panel model* **(d)** *Double panel model*

Figure 5-2: *Panels models used for the comparison.White panels are part of the outer surface, red panels are additional. Submergence is 1m.*

The dipole panel model, shown in 5-2b, is obtained by removing the top surface panels of the original body. The model is fitted with dipole panels since fluid is present at both sides of each panel.

The raised panel model, shown in 5-2c, uses a raised version of the original cylinder. This model is obtained by removing the top surface panels and subsequently raising the sides to the still water surface by adding extra panels.

The double panel model model, shown in 5-2d, uses an open model of the cylinder with a finite thickness. This model is obtained by removing the top surface panels, subsequently placing a cylinder with a slightly smaller diameter and height inside and finally adding a small ring of panels on top to close the model.

It should be noted that it is known in advance that the dipole panel model is not suitable for the numerical model, as WAMIT provides the sum of the pressures at both sides of a dipole panel only. Therefore it is not possible the apply the pressure integration technique on the outer side of this model, as explained in section 5-1. For this reason the double panel model is added. The double panel model mimics the dipole panel model for decreasing wall thickness, whereas the ability to acquire the pressure solely on the outer surface is still present.

5-2-1 Physical acceptance of the panel models

In case of small submergence, only a relatively thin layer of water is present on top of the body. In this case the majority of the wave will be diffracted by the body, whereas only a small part of the energy is lost on top. By raising the sides of the cylinder to the water line, it is assumed that the entire wave is diffracted and that the wave is not able to enter the shallow water region on top. This additional assumption is valid for small submergences only. In case of larger submergences this assumption is less valid, since the waves tend to roll over the body.

For larger submergences the double panel model might be more valid, since this models does not block the flow of water on top. In addition, the model tests and CFD simulations indicated that a small pumping mode is present. This follows from water flowing on top of the cylinder over the entire circumference. As soon as this water comes together, a pumping mode arises. The presence of a pumping mode is completely lost with the raised panel model. This is not the case for the double model. With this model it is expected that the pumping mode is still present, whereas the erroneous results at the top surface disappear.

5-3 Double panel model dimensions

The sides of the double panel model can be considered as thin elements with a finite thickness. As a general rule within diffraction theory this thickness must be comparable to the size of the panels. Four variations are used for this model where the bottom and side wall thickness are varied (and the panel size to satisfy the general rule). The first variation has an inner diameter D of 13 m and a bottom wall thickness B of 1 m (referred to as D13B1), the second has dimensions D14B1, the third variation has dimensions D14B0.5 and the fourth has the same dimensions as the third, however it has larger panels such that it does not fulfill the general rule (indicated with D14B0.5$_C$). The latter is added to the comparison to indicate the appearance of potential errors due to panel sources being to close to each other. The four variations will be compared with each other.

The main purpose of the comparison is to examine the effect of the varying wall thickness and additionally to check for any potential errors due to panel sources being to close to each other. The dipole panel model is added to this comparison since it is expected that the results of the double panel models approach the results of this model for decreasing wall thickness. In this comparison *all* panels are taken into account in the pressure integration. The dimensions which result in the most optimal balance between computational time and accuracy is selected. In section 5-4 this model is further compared to the other adjusted panel models by focusing specifically on the outer surface.

5-3-1 Added mass and damping coefficients

To check for convergence and to reveal any potential errors, the added mass and damping coefficients are compared. Figure 5-3 shows the coefficients for the various double panel models and the dipole model.

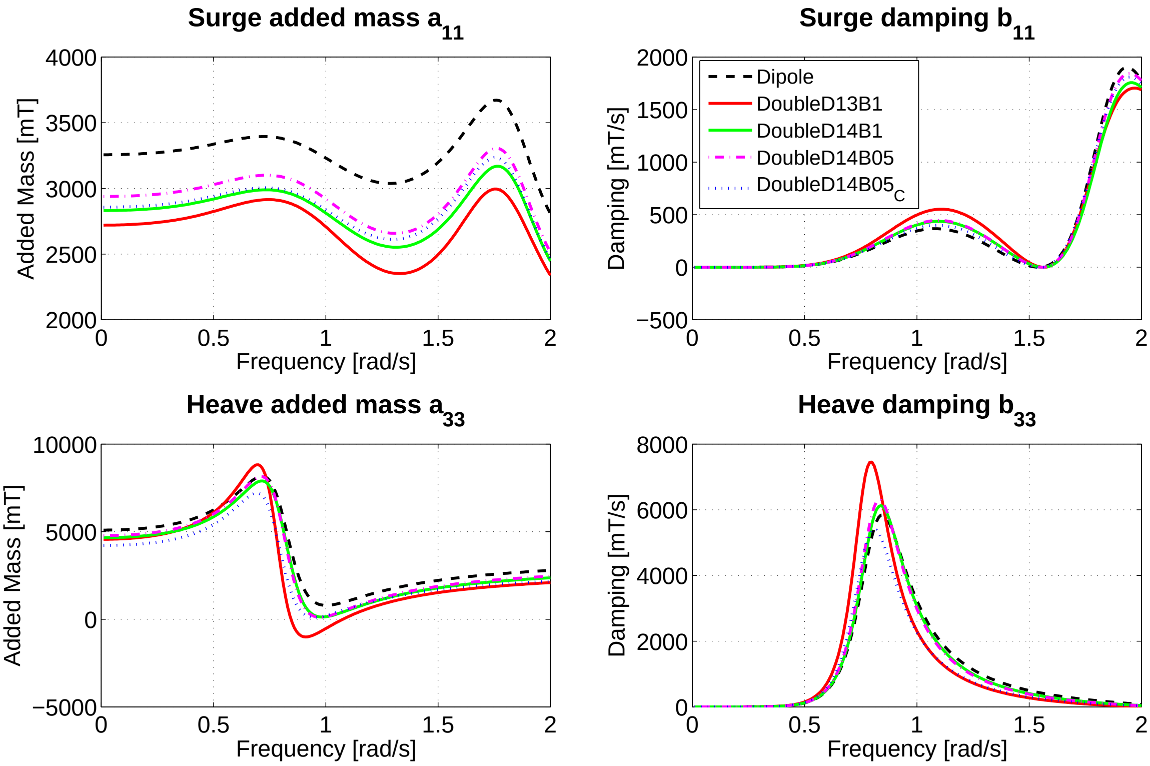

Figure 5-3: *Hydrodynamic coefficients for surge and heave of the dipole and double panel models*

At each graph it can be seen that the curvature of the D13B1 model deviates most from the others. In heave added mass a different negative slope, a higher peak and lower trough is observed. The heave added mass even becomes negative at approximately 0.90 rad/s. Focusing on heave damping it is clearly visible that the higher peak shifted to a lower frequency. It is expected that these deviations in the D13B1 model are caused by the larger horizontal area at the top of the double panel model walls. This is not further investigated in this research.

For surge added mass its clearly visible that the models approach the dipole model for decreasing wall thickness. However, the coarse D14B0.5 model does not follow this trend. At low frequencies it is more in line with the D14B1 model, whereas for higher frequencies it follows its finer grid variant. For heave it can be observed that this model underestimates the coefficients compared. This indicates that errors are present due to panel sources being to close to each other, which was expected for this model.

Note that the added mass and damping coefficients shown in figure 5-3 are merely used to check for any numerical errors in the double panel models. The coefficients are not of interest for the first part of this research since we focus on a captive body. These coefficients will be covered again in chapter 7.

5-3-2 Wave forces

Wave forces (left graphs) and the phase shifts (right graphs) are shown in figure 5-4 for surge and heave direction.

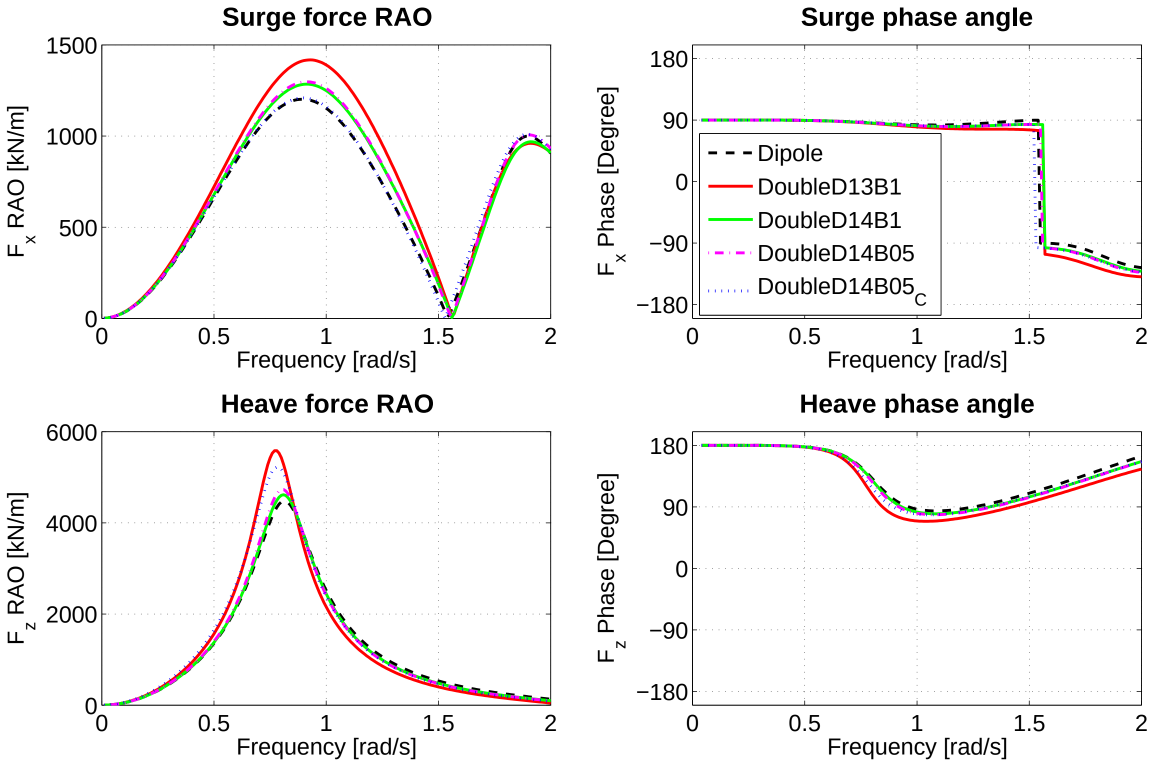

Figure 5-4: *Wave forces of the dipole panel model compared to the various double sided panel models.*

The same trends can be observed as for the hydrodynamic coefficients. The D13B1 model shows the largest deviation from the dipole model for both surge and heave force. All panels models show a similar but smaller peak in the heave force RAO around 0.75 rad/s as was obtained for the original cylinder. Visualization of the surface elevations show that a similar but smaller pumping mode is present, as was observed for the original cylinder. This was expected already, as stated in section 5-2-1. Further investigation of this peak is performed in section 5-4.

5-3-3 Conclusion dimension selection

Varies geometries of the double panel model are compared. Here the dipole panel model was added for reference. Most deviations were found at the D13B1 model. The wall thickness of 1 m is too large to obtained accurate results. The coarse D14B0.5 model showed deviating results due to the panel sources being to close to each other. For this model the wall thickness is too small compared to the panel size.

Both the D14B0.5 and D14B1 showed approximately similar results. The refined geometry of the D14B0.5 model did not give significant improvements in the results, whereby the computational time to perform the radiation diffraction calculation was significantly longer; 35 min compared to approximately 5 min for the D14B1 model. Therefore the D14B0.5 dimensions will be eliminated as well. From now on we will use the dimensions of the D14B1 model for the double panel model.

5-4 Wave forces on the outer surface

In section 5-3 the integration was performed on all panels to acquire the added mass and damping coefficients and the wave loads on the entire body. From now on the pressure integration technique of equation (5-2) is used to acquire the forces on specifically selected areas. Decomposition of the double sided cylinder is shown in figure 5-5. In the upcoming figures the labels will be included as subscript in the legend to indicate which areas are taken into account. Note that the outer surface is indicated with Outer.

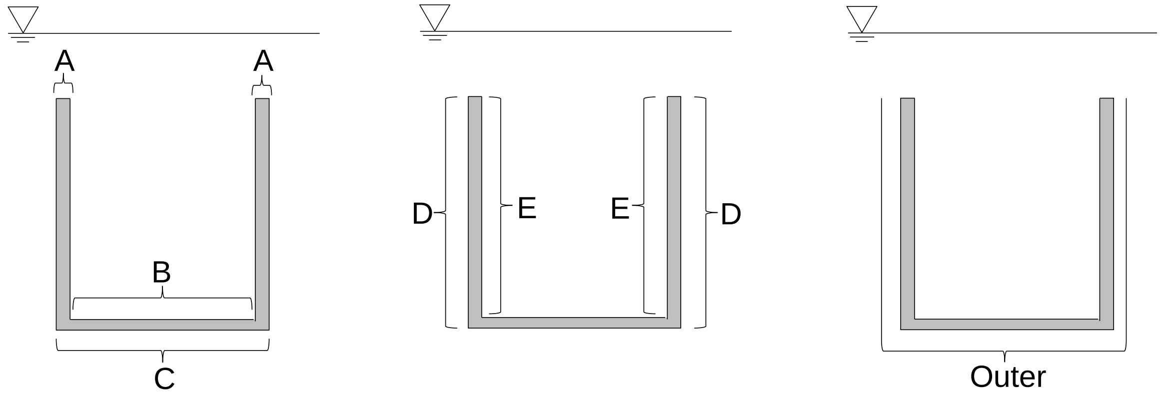

Figure 5-5: *Area indication of the double panel model*

5-4-1 Double versus dipole panel model

During the comparison of the various double panel models, a peak in the heave force RAO was observed due to a pumping mode. Starting with the upper two graphs of figure 5-6 showing the heave force RAO and phase for the dipole panel model, the full double panel model and the double panel model including the bottom and inner areas only. It can be seen that disregarding the small ring of panels on top has an insignificant effect on the peak in the heave force RAO, despite the fact that these panels being in close proximity of the free surface.

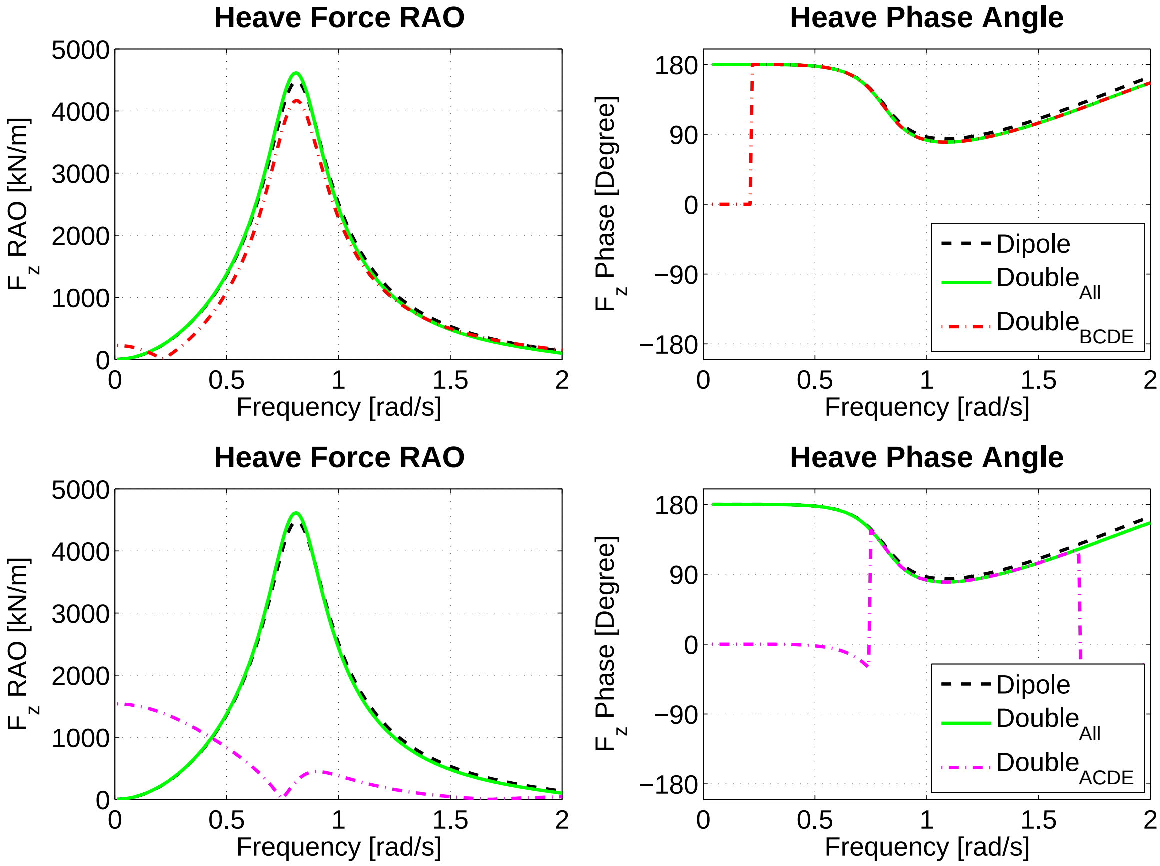

Figure 5-6: *Components of the heave force RAOs and phase for the dipole and double panel model.*

In the lower two graphs of figure 5-6 only the bottom and top panels are taken into account. Here it can be seen that the peak vanishes completely and the heave force experiences a 180° phase shift around 0.75 rad/s. The significant change indicates that the inner panels are the main contributors of the peak. This can be supported by considering the orbital motions of the water particles. The water inside the cylinder tends to follow the orbital motion induced by the incoming waves, however the motion is restrained by the cylinder walls in horizontal and downward direction. The only way out for the entrapped water is to go upwards. The blockage of the motion in downward direction by the inner panels induces high pressures, resulting in the peak in the heave force RAO.

5-4-2 Double versus raised panel model

Figure 5-7 shows the force RAO and phase for surge and heave for the double and raised panel model. Here only the outer surface is taken into account in the pressure integration.

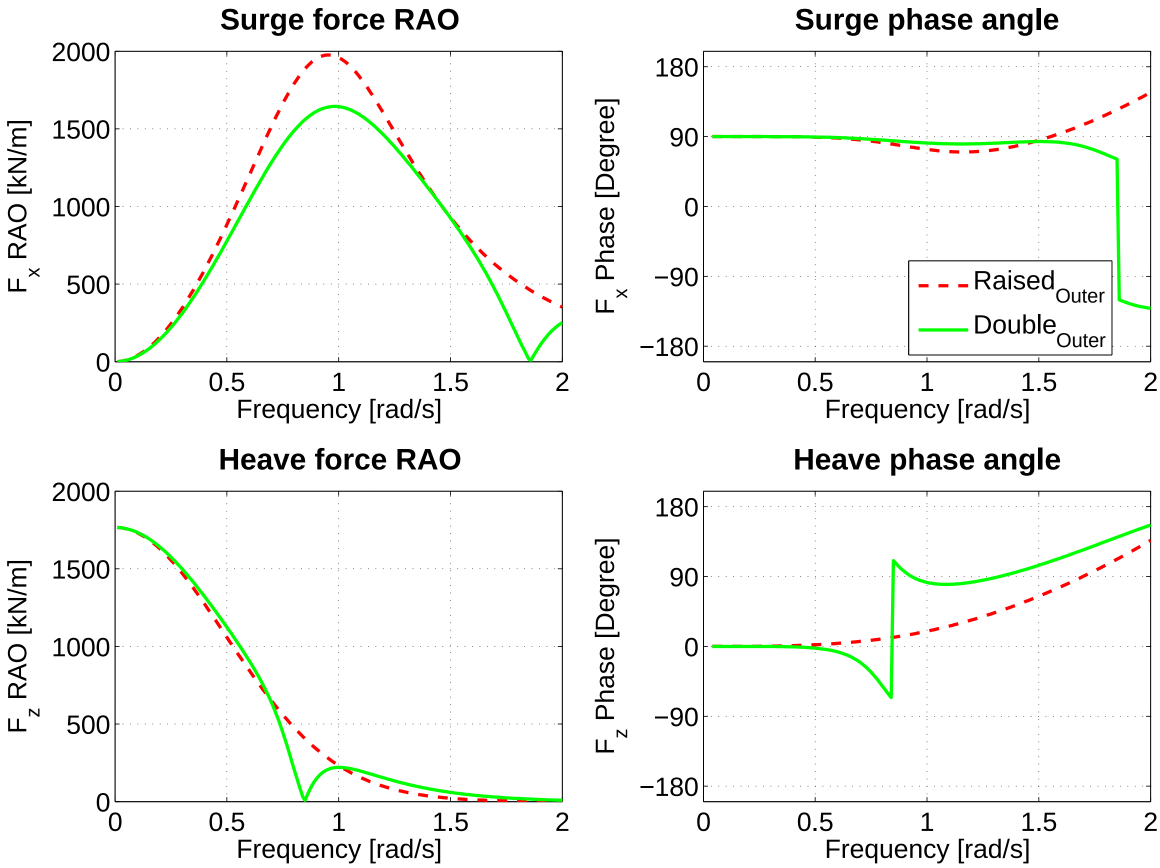

Figure 5-7: *Force RAOs and phase on the outer surface of the raised and double panel model.*

The peak in surge force of the raised panel model is around 20% higher than the peak of the double panel model. This can be explained based on the geometry used for the raised panel model, as shown in figure 5-2d. Although the additional panels are not taken into account during the pressure integration, they are present while solving the diffraction problem. The fluid has to fulfill the boundary condition of zero velocity normal to these additional panels, whereas for the double panel model the fluid can flow through the small gap. This leads to an overall increase in fluid pressure for the raised panel model in this area, which has an effect on the uppermost panels of the outer surface. Next to the deviation in the RAO, the double panel models shows an additional phase shift at the higher frequencies.

For heave the two panel models show the same RAO values in the low and high frequency limit. Same holds for the phase angle (to a lesser extend at high frequencies). The double panel models experiences a phase shift around 0.8 rad/s, whereas the phase shift is not present at the raised panel model. A similar phase shift was found at the original submerged cylinder by [8] at a slightly lower frequency. Therefore these results should be handled with care.

5-5 Panel Model Selection

At the beginning of this chapter, two adjusted panels models are proposed to capture the hydrodynamic data of the cylinder's outer surface: a raised panel model and a double panel model. Additionally a dipole model is used to validate the wall thickness of the double panel model. Each of the two proposed models has a different physical motivation.

The raised panel model followed by the additional assumption that waves are not able to reach the shallow water region on top of the cylinder. This assumption is applicable to small submergences only. At larger submergences the waves tend to roll over the body, such the assumption is less valid.

By raising the sides up to the water surface, the presence of any pumping mode is lost for the raised panel model. This is not the case for the double panel model. Visualization showed the a pumping mode is present for this model, whereas it is significantly smaller than the original cylinder. In addition, this panel model is still valid at larger submergence.

Both models showed minor differences in the surge and heave force RAOs for the outer surface. The raised panel model gave a 20% higher peak in surge RAO. This can be explained by the adjusted geometry used in WAMIT while solving the diffraction problem. The double panel model showed a phase shift in heave force RAO, caused by the pumping mode. A similar phase shift was found for the original cylinder, which indicates that the phase shift should be handled with care.

The differences do not provide enough information to rule out one of the compared panel models. Additionally, the two different physical motivations gives the models both advantages and disadvantages. Therefore the choice is made to continue with both the raised panel model as the double sided panel model.

This chapter continues with determining the tank boundary conditions for both models. Subsequently in chapter 8, the numerical model is applied using the input of both the raised as the double sided panel model. With the obtained force RAOs the selection is made which panel model represents the model test results best.

5-6 Tank boundary conditions

Next to acquiring the hydrodynamic data on the outer surface of the body, the purpose of the radiation diffraction analysis is to obtain the tank boundary conditions. These boundary conditions consists of two components:

1. The free-surface elevation in front of the tank domain, and;
2. The wave induced pressure on the tank domain boundary.

These two components in turn consists of two subcomponents: (a) caused by the incoming and diffracted waves on a still body and (b) caused by radiated waves due to a moving body in still water. For the captive cylinder the components 1b and 2b will be zero since the body is fixed. For the freely-floating SSCV these components are present. However, in this work they are not taken into account due to time constraints. The tank boundary conditions will be outputted and passed onto the time domain solver in the form of RAOs, which in turn will be used in section 5-7 to create deterministic time traces. Similar as a motion or force RAO, a surface elevation RAO and corresponding phase gives the surface elevation at a specific location due to an undisturbed wave at the hydrodynamic origin. The pressure RAO and phase gives the dynamic pressure at a specific location due to an undisturbed wave at the hydrodynamic origin.

5-6-1 Surface elevations

The free-surface elevation in front of the tank domain is used to determine the height of the flow opening and to determine the static pressure distribution, both at the outer side of the tank. A similar option as for the panel pressures is used within WAMIT to output the separate components of the diffraction and radiation free-surface elevation at predetermined field points (by assigning the parameters IOPTN(6)=1 and INUMOPT6=1 in respectively the force control file and the configuration file). The x, y and z-coordinates of the field points are defined in the force control file, whereas the z-coordinate should be zero such that WAMIT regards the field point as a free-surface elevation point. Multiple field points are equally distributed around the cylinder, all within a distance on the order of the dimensions of the adjacent panels away from the body. The blue dots in figure 5-10 indicate the field points used for both panel models.

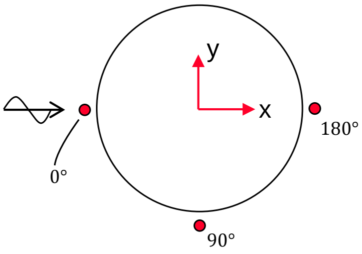

Figure 5-8: *Locations of the field points shown in figure 5-9.*

Figure 5-9 shows the diffraction surface elevation RAO and phase for both panel models at the leading, side and trailing edge of the cylinder (according to figure 5-8). Here it can be seen that all RAOs equal unity and all phases equal zero for long waves, implying that the surface elevation points follow the wave at the origin. The RAO at the leading edge (0°) of the raised panel model approaches 2 m/m for shorter waves. Here the wave is nearly fully reflected resulting in a nearly standing wave, caused by the boundary condition of zero velocity normal to the body's surface. The RAOs of the double panel model vary significant more over the frequency range. At 0.8 rad/s (where the peak in the heave force RAO was observed, figure 5-6) a similar peak is observed due to the pumping mode, especially at the trailing edge. The peak here could be amplified by waves traveling around the cylinder and focusing behind it.

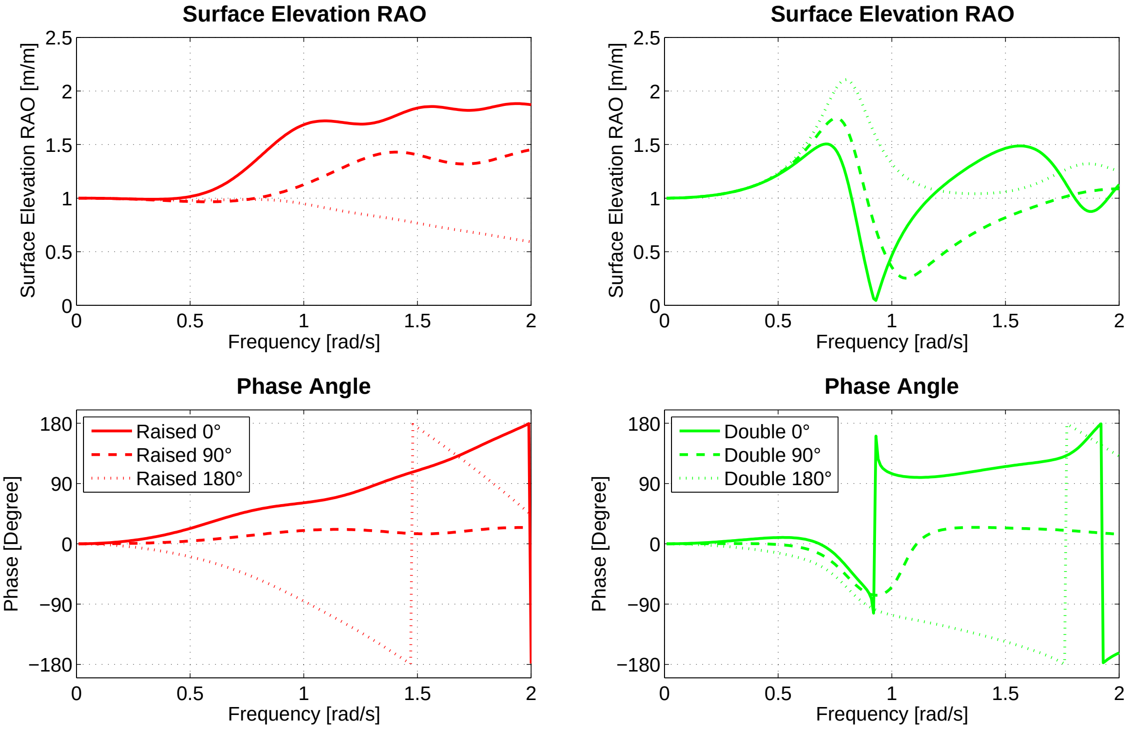

(a) *Raised Panel Model* **(b)** *Double Panel Model*

Figure 5-9: *Diffraction surface elevation RAO and corresponding phase at three locations for both panel models*

5-6-2 Pressures

The outer pressure is induced by the waves and gives, together with the hydrostatic pressure, the total pressure at the outer side of the tank domain boundary. For the raised panel model we take the advantage of the additional panels which are already present. The pressures on these panels were disregarded while determining the hydrodynamic data but can be used as tank boundary conditions. This results in a piecewise constant distribution of the pressure over the tank boundary.

The double panel model is not in the possession of these panels. Here the outer pressure will be acquired by defining the same kind of field points as for the free-surface elevation. The x, y and z-coordinates of these field points are defined in the force control file. The coordinates are taken the same as the coordinates of the centroids of the additional panels of the raised panel model. Since the z-coordinates are now negative values, WAMIT regards the field points as pressure points instead of a free-surface elevation points. The green dots in figure 5-10b give an overview of the pressure points used for the double panel model.

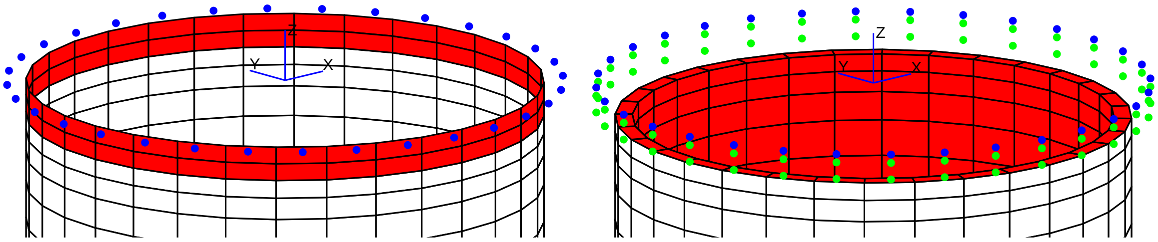

(a) *Raised panel model. Pressures on the red panels are used as pressure boundary conditions.*

(b) *Double panel model. Pressures at the green dots are used as pressure boundary conditions.*

Figure 5-10: *Overview of the tank boundary conditions. Blue dots represent surface elevation points.*

Since the double panel model is not in the possession of the raised panel, the pressure at the tank boundary is described by a discrete set of points only. To avoid unnecessary complexity in the flow module, it is assumed that the pressure provided by a field point is applicable on the same panel area as for the raised panel model. This results in a similar piecewise constant distribution of the pressure over the tank boundary.

5-7 Frequency to Time Domain

The wave forces and boundary conditions are obtained from frequency domain calculations. To use them in the time domain-based flow and motion modules, deterministic time records are required. Since the response of the wave forces and boundary conditions are linear phenomena, time histories for a certain sea state can be obtained by using the wave spectrum and the response frequency characteristics.

In case of an irregular sea state simulation, the wave spectrum $S_\zeta(\omega)$ can be discretized in N frequency components with equally spaced intervals of $\Delta\omega$. For each frequency component ω_i a separate wave component with amplitude ζ_{a_i} can be determined:

$$\zeta_{a_i} = \sqrt{2S_\zeta(\omega_i)\Delta\omega} \qquad \text{where} \qquad i = 1..N \tag{5-11}$$

As soon as all wave amplitude components are known, a complete wave record can be created by summing up all N components (wave superposition):

$$\zeta(t) = \sum_{i=1}^{N} \zeta_{a_i} \cos\left(\omega_i t + \varepsilon_i\right) \tag{5-12}$$

where ε_i is a randomly chosen phase shift between 0 and 2π for the i-th wave component.

In a similar way a time history of a response can be obtained. By taking $H(\omega)$ as the complex valued frequency response function of a certain phenomena, each wave amplitude ζ_{a_i} can be multiplied by the corresponding RAO-value $|H(\omega_i)|$ to obtain the response amplitude. Then by adding the additional phase $\varepsilon_{H\zeta_i}$ the time history of the response becomes:

$$H(t) = \sum_{i=1}^{N} |H(\omega_i)| \, \zeta_{a_i} \cos(\omega_i t + \varepsilon_i + \varepsilon_{H\zeta_i}) \qquad \text{where} \qquad \varepsilon_{H\zeta_i} = \arg\, H(\omega_i) \tag{5-13}$$

This can be done for each of the six wave force RAOs, for each surface elevation RAO and for each pressure RAO. This in turn will result in a force time trace for each of the six modes, a surface elevation time trace for each field point and a pressure time trace for each additional panel (raised panel model) or pressure point (double panel model).

In case of a regular wave simulation one wave component is present, i.e. $N = 1$ in (5-12). With a predetermined wave amplitude ζ_{a_1}, frequency ω_1 and phase $\varepsilon_1 = 0$ a sinusoidal wave signal is obtained. In a similar way the response is obtained by taking the corresponding response value $H(\omega_1)$ in equation (5-13).

Due to time constraints in this research, the incorporation of the wave forces, tank pressures and surface elevations in the time domain is simplified by assuming that no phase shift is present due to a surge or sway motion. Additionally, no dependency on the yaw angle is taken into account.

Chapter 6

Implementation of the Flow Module

The time-domain simulation consists of two modules. The Motion Module is used to solve the equations of motions of the body numerically. In order to solve these equations, the force exerted by the flooding tanks on the top surface of the body is required. This force component is calculated by the Flow Module. The implementation of the Flow Module is covered in this chapter.

During a time step the Flow Module partitions the tank boundary in multiple sections. These sections are based on the still water level, outer surface elevation, tank level and the panels at the tank boundary (as was shown in figure 5-10a). Subsequently the pressure distribution at both sides of each section is calculated. At the outer side a hydrostatic pressure and an additional dynamic pressure induced by the waves are present. Due to the still water assumption inside the flooding tanks, only a hydrostatic pressure acts on the inner side of the tank boundary. This hydrostatic pressure is based on the tank filling grade. The flow velocity at each section follows by applying the Bernoulli Equation including the outer and inner pressures. With the flow velocity at each section, the total discharge through each section is acquired. Here, a flow coefficient is used to take into account pressure losses, viscous effects and general resistance of the floodwater. Summing up the individual discharges yields the total discharge through the tank boundary, after which the new tank filling grade is obtained.

First different types of flow are considered, followed by the fluid pressures in the outer domain. Here, two different options are found to incorporate the static pressure. Subsequently the partitioning of the tank boundary is further elaborated on. Thereafter the application of fluid flow based on the Bernoulli equation is discussed, including the determination of the flow coefficients. This chapter ends with an elementary test case to validate the flow module and to determine the required step size for the time-domain simulation.

6-1 Types of Flow

There are several cases to be considered in relation to the type of flow, see figure 6-1. Here, the red dashed line represents the tank boundary. Left of the boundary is the outer domain with a free surface elevation and dynamic pressure due to the incoming wave. The right side represents the tank domain with a certain tank filling grade.

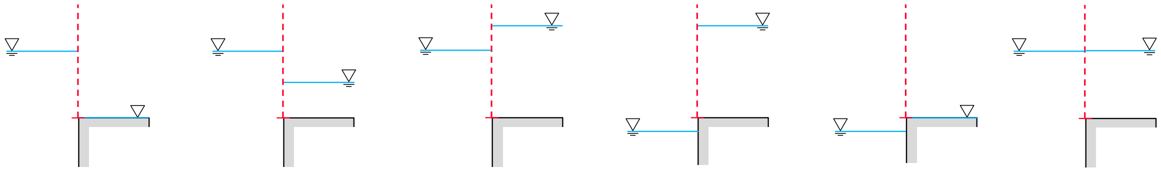
Case 1 Case 2 Case 3 Case 4 Case 5 Case 6

Figure 6-1: *Various types of flow depending on the outer surface elevation and the tank filling grade.*

A flow is generated by means of a pressure difference at both sides of the tank boundary. In case of pure hydrostatics, a distinction can be made between tank inflow (case 1 and 2), outflow (case 3 and 4) and no flow (case 5 and 6). Note that the presence of an additional wave-induced dynamic pressure at the outer domain may cause an opposite flow, such as inflow at case 3.

Figure 6-1 shows four cases which will result in a fluid flow. However, in the sense of fluid flow physics, only two elementary cases have to be distinguished [14]. Based on the static water levels on both sides of the boundary we have either a section of:

- Free flow, or
- Submerged flow.

The former occurs where fluid is present at only one side of the boundary and the latter occurs where fluid is present at both sides. By splitting the tank boundary into one or two sections, the four types of flow from figure 6-1 can be developed from these two elementary cases by superposition. For example case1 consists of one section with free inflow, whereas case 2 can be split into free inflow from the outer free surface elevation down to the tank water level and submerged flow from the tank water level to the upper edge of the body.

6-2 Fluid Pressures

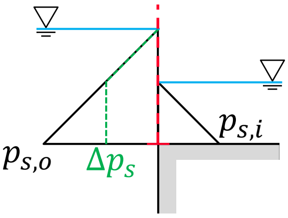

Figure 6-2: *Static pressure distribution of case 2*

The pressure difference which causes the fluid to flow consists of a static and dynamic component. The hydrostatic pressure difference Δp_s is defined as the difference in outer hydrostatic pressure $p_{s,o}$ and inner $p_{s,i}$, see figure 6-2. Based on the two elementary flow cases we are able to describe the hydrostatic pressure difference Δp_s as two simple expressions. At the upper section where free flow is applicable Δp_s increases linearly with the submergence below the water surface. At the lower section including submerged flow, the hydrostatic pressure difference results in a constant value over the height. This value follows from the difference in outer surface elevation and inner tank water level.

Inside the tank still water is assumed during the time step. As a result only the static pressure $p_{s,i}$ is taken into account. At the outer side an additional wave-induced dynamic pressure is present. Two options are found to incorporate this dynamic wave pressure component. Either it is supposed that the dynamic pressure can be added to the fluctuating static pressure $p_{s,o}$ or the *total* pressure distribution is obtained according to linear wave theory.

6-2-1 Fluctuating static pressure

If the hydrostatic principle is followed, $p_{s,o}$ fluctuates with the outer water level. This water level in turn is predefined by the time trace of the surface elevation boundary condition. The wave-induced dynamic pressure is then added to obtain the total pressure at the outer domain. This dynamic pressure is predefined by the time trace of the pressure boundary condition and follows from the radiation diffraction analysis as well. Linear wave theory is used here, such that the pressure is defined up to the still water line. Figure 6-3 shows the total pressure distribution along the vertical beneath a wave crest and a wave trough for an undisturbed wave:

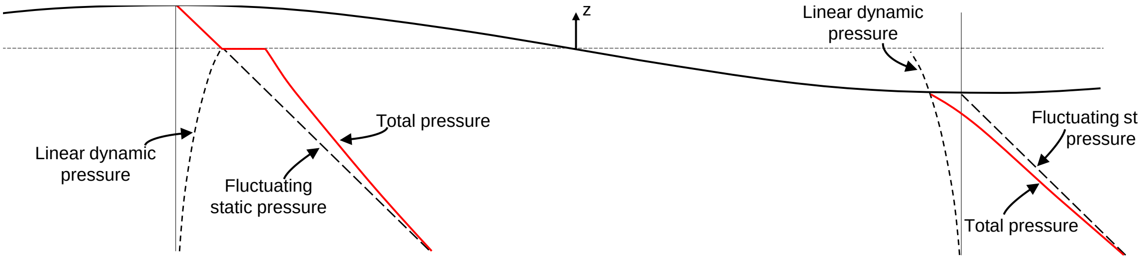

Figure 6-3: *The wave-induced dynamic pressure superimposed on the fluctuating hydrostatic pressure under a wave crest and a wave trough.*

6-2-2 Fixed static pressure

Instead of adding the dynamic wave pressure to the fluctuating hydrostatic pressure, the total pressure field under a wave can be obtained according to linear wave theory entirely. The pressure in linear wave theory follows from the substitution of the wave potential Φ_w into the linearized Bernoulli equation (a more detailed description is included in appendix A). After rewriting this expression yields the following expression for the wave pressure p in deep water:

$$p = -\rho g z + \rho g \zeta_a e^{kz} \cos(kx - \omega t) \tag{6-1}$$

The first term on the RHS gives the hydrostatic pressure at height z and the second term is the dynamic pressure owing to the wave-induced particle acceleration. Figure 6-4 shows the total pressure distribution according to linear wave theory.

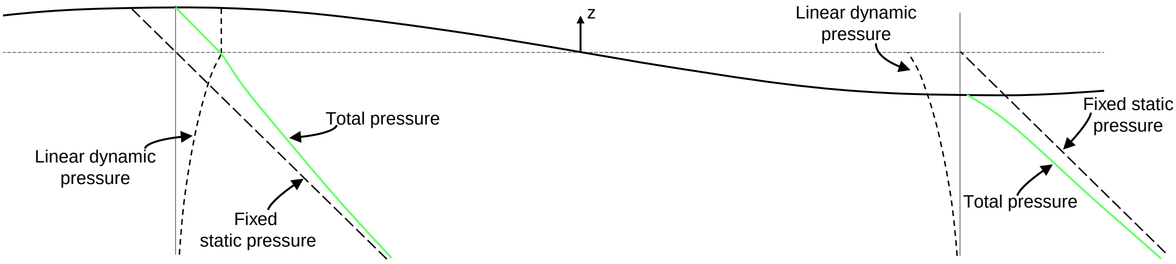

Figure 6-4: *The wave-induced dynamic pressure superimposed on the* <u>*fixed*</u> *hydrostatic pressure under a wave crest and a wave trough according to linear wave theory.*

Above the still water line the z-coordinate is positive resulting in a negative static pressure distribution. To make sure that above the still water line the pressure regularly decreases to zero at the water surface, a constant extension of the dynamic pressure above $z = 0$ is used. In this case the hydrostatic pressure cancels the dynamic pressure exactly at the free surface of the wave crest, whereas a second-order error or higher is present at the wave through [15].

Both the fluctuating as the fixed static pressure option is incorporated in the Flow Module. At the end of this chapter several elementary flow cases are used to determine the correct interpretation of the static pressure.

6-3 Flow Sections

At the beginning of section 6-2 it is stated that, in case of a static pressure distribution only, the total tank boundary can be split into two sections, as shown in figure 6-5a. Here, free flow is present at section A and submerged flow is present at section B.

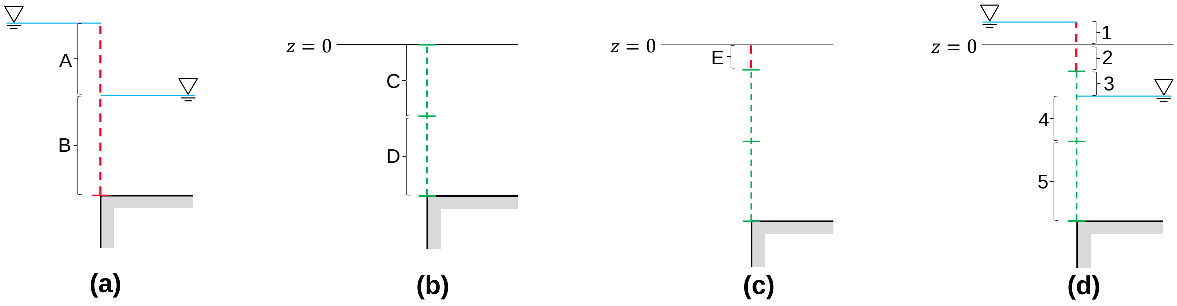

(a) (b) (c) (d)

Figure 6-5: *Flow sections of the tank boundary. The total partitioning of the tank boundary shown in* ***d****, follows from the static pressure sections (****a****), the dynamic pressure sections (****b****) and an additional section due to motions (****c****).*

For the dynamic pressure, it is not possible to consider the sections A and B, since the pressure distribution follows from the panel geometry used in the radiation diffraction analysis. In this analysis the dynamic pressure is acquired as a constant distribution over the surface of each panel. It fluctuates in time and is specified as the dynamic pressure boundary condition. In case the tank boundary is represented by two panels in vertical direction, the tank boundary can be split in two section with the geometry of the panels. These sections are indicated as C and D in figure 6-5b. At both these sections, the dynamic pressure is present at the side adjacent to the outer domain.

The dynamic pressure at sections C and D follows from linear theory. As a result, the panel geometry and the accompanying pressure is defined up to the still water line at $z = 0$. In the numerical model, a motion of the body will result in an additional section E as shown in 6-5c. At the outer side of this section the dynamic pressure of the uppermost panel is applied.

Combining the sections indicated in figure 6-5a to c will result in a total of 5 sections, as shown in figure 6-5d. At sections 1 to 5 a static pressure distribution is present at the side adjacent to the outer domain. At this side an additional dynamic pressure is present for sections 2 to 5, since the dynamic pressure is defined up to $z = 0$. At the inner side only a static pressure distribution is present at sections 4 and 5. Note that more sections are required as soon as more panels in vertical direction are used to represent the tank boundary. In general it can be stated that a total of $N = 3 + K$ sections are required, if K panels are used.

Application to a body

The tank boundary shown in figure 6-5d is partitioned in one dimensional sections. Applying it to a submerged body will be explained according to figure 6-6. Here, the submerged part of the tank boundary of the cylinder is indicated with the red panels. Each panel has its own dynamic pressure time trace. The blue dots indicate where the surface elevations time traces are acquired.

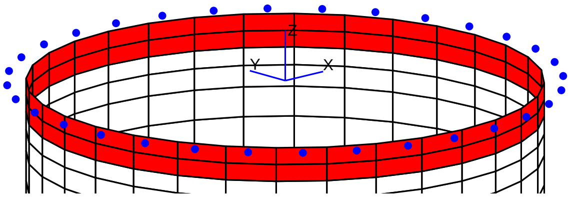

Figure 6-6: *Tank Boundary*

The entire circumference of the tank boundary is split into multiple slices, where the width of each slice is determined by the width of the red panels. Each slice has its own blue dot to indicate the surface elevation. At each time step, the Flow Module acquires for each slide the new outer surface elevation, tank level and orientation of the panels with respect to $z = 0$. Based on these values, all the slices are partitioned into 5 new sections. The remainder of this chapter regards the tank boundary as one slice only, unless stated otherwise.

6-4 Bernoulli Flow

The flow velocity at each of the N sections is based on the Bernoulli equation, shown hereafter. Similar application of the Bernoulli equation can be found for example in damage stability and progressive flooding simulations such as [16] and [17].

$$\rho g z_1 + \rho \frac{\partial \phi}{\partial t} = \rho g z_2 + \frac{1}{2} \rho v_2^2 \tag{6-2}$$

Here, the first and second terms on the LHS are respectively the hydrostatic and dynamic wave pressure acting on the outer side. On the RHS we have the inner hydrostatic pressure and the dynamic pressure due to the kinetic energy of the water particles. Rewriting (6-2) gives the expression for the flow velocity based on the a pressure difference Δp:

$$v = \sqrt{\frac{2}{\rho} \left(\rho g \left(z_1 - z_2 \right) + \rho \frac{\partial \phi}{\partial t} \right)} = \sqrt{\frac{2}{\rho} \Delta p} \tag{6-3}$$

The pressure difference ΔP at equation (6-3) is determined at the upper and lower edge of each section. Subsequently, the average value is used to determine the average flow velocity over the section. Taking the averaging pressure is valid for fully submerged sections since both the static and dynamic components are constant over the area. In case of a section where free flow is applicable, either z_1 plus the dynamic term or z_2 is zero and the pressure varies over the submergence. In 6-6-1 it is shown that the effect of taking the average pressure over the free flow section is insignificant. To take into account the direction of the flow at each section, (6-3) is modified to the following discretized form:

$$v_i = \operatorname{sgn} \left(\Delta p_i \right) \sqrt{2 \rho^{-1} \left| \Delta p_i \right|} \qquad \text{for} \qquad i = 1 \ldots N \tag{6-4}$$

Here equation (6-4) remains valid if the flow direction changes, as the signum function returns 1 for positive and -1 for negative arguments. The total discharge of water Q is then obtained by integrating the velocity over the tank boundary area A.

$$Q = C_f \iint\limits_A v dA = \sum_{i=1}^{N} C_{f,i} v_i A_i \tag{6-5}$$

where A_i is the area of the i-th section and $C_{f,i}$ is a flow coefficient (further elaborated in section 6-4-1). Discretization the integral is valid again since the velocity is averaged over the section. Subsequently the increase in tank water level $\Delta \tau$ is acquired by multiplying the total discharge Q with the time step Δt and dividing it by the tank ground plane area A_0. The new tank water level τ_{new} is then given by:

$$\tau_{\text{new}} = \tau_{\text{old}} + \Delta \tau \qquad \text{where} \qquad \Delta \tau = Q \frac{\Delta t}{A_o} \tag{6-6}$$

6-4-1 Flow coefficients

Equation 6-4 only gives an approximation of the true flow velocity. It is acknowledged that the true flow is highly turbulent and chaotic and therefore extremely complex. As a simplification it has been assumed that the flow can be adequately modeled by this equation with the addition of a discharge or flow coefficient C_f. Typical values for the coefficient applicable to this problem are not abundant in open literature. For damage stability and progressive flooding simulations, [18] (as cited in [19]) has compared numerical simulations against experimental data and concluded that $C_f = 0.6$ is a good approximation for damage openings. This value has been widely used in other flooding simulations, e.g. [16], [19] and [20].

The above mentioned coefficient however is based on damage openings shaped as sharp-crested orifices, which are submerged and full of fluid. The flooding tanks have large flow areas and the free surface inside the tank is exposed to ambient pressure. This might have more agreements with open channel flow containing a weir; a channel obstruction over which the flow is deflected. Figure 6-7 shows a common (broad-crested) weir where V is the upstream velocity and y_c is the critical fluid height on top.

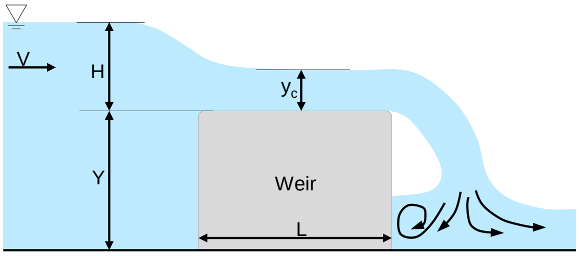

Figure 6-7: *Flow over a broad-crested weir*

At the top of the weir the fluid experiences a short run of nearly one-dimensional critical flow with velocity $V_c = \sqrt{gy_c}$ [21]. For a sharp-crested weir (i.e. $L \ll Y$) [22] (as cited in [21]) recommends the following flow coefficient:

$$C_f = 0.564 + 0.0846\frac{H}{Y} \qquad \text{for} \qquad \frac{H}{Y} \leq 2 \tag{6-7}$$

Here it can be seen that the sharp-crested weir approaches the flow coefficient used in the previous mentioned flooding simulations. The flow coefficient for a broad-crested weir becomes dependent on the surface roughness ϵ and the length L. For a broad-crested weir C_f is recommended by:

$$C_f = 0.544\left(1 - \frac{\delta/L}{H/L}\right)^{3/2} \qquad \text{where} \qquad \delta/L \approx 0.001 + 0.2\sqrt{\epsilon/L} \tag{6-8}$$

If it is assumed for the moment that L equals the diameter of the cylinder (15 m), H equals the submergence (1 m) and $\epsilon = 0.05\,\text{m}$ (sheet metal), then a flow coefficient of approximately 0.4 is applicable.

A flow coefficient in the order of $0.4 \sim 0.6$ is relevant if the stated literature is followed. To verify these values, an additional analysis on the flow coefficient is performed. Here the numerical model is applied to the submerged captive cylinder. The results of this analysis are included in appendix D. In the analysis the flow coefficient is split into an inflow and outflow coefficient. Both components are tuned using regular waves, such that the acquired heave force time trace has the most optimal fit to CFD results. Per wave height, the inflow and outflow coefficients are plotted against a dimensionless kD-value (wave number times length scale).

For low frequency waves (i.e. low kD-values) the analysis confirmed a coefficient of approximately 0.6 for both flow directions. For high frequency waves more discrepancy was found. The inflow coefficient converged to approximately 0.4, whereas for outflow a dependency on the wave height was found. Small wave heights resulted in an outflow coefficient of 0.4 and large wave heights required a coefficient of 1.0. However, the position of the cylinder and SSCV Thialf are indicted on the dimensionless kD-axis. Following these kD values, an inflow coefficient of $0.4 \sim 0.5$ and an outflow coefficient of $0.5 \sim 0.7$ are applicable. Therefore, for both regular as irregular wave simulations, a flow coefficient of 0.6 is maintained for both inflow and outflow.

6-5 Tank Forces

The tank level τ from (6-6) (the subscript $_{new}$ is omitted for clarity) exerts a static force on the top surface of the body. In case no waves are present and τ is equal to the still water level, no excitation force is present on the body. As a result, a vertical excitation force f_t is exerted by the tanks as soon as the tank water level deviates from the equilibrium position τ_0:

$$f_t = \rho g \left(\tau_0 - \tau\right) A_0 \tag{6-9}$$

In which τ_0 is determined as the submergence of the tank below $z = 0$ at the beginning of the time step. Note that for a fixed body τ_0 is constant and equals the submergence of the body.

Due to the still water and horizontal tank assumptions, an equal tank filling grade is present in the entire tank. Therefore the point of application of the force is at the center of the tank ground plane area A_0. No local moments are induced by the tank water on the body. The overall roll and pitch moments induced by the tank follow from the vertical force times a moment arm. The moment arm $\vec{r_t} = [x \;\; y]^T$ is defined as the distance from the tank's ground plane area center to the point of interest. This results in the following static tank force vector $\vec{F}_{\mathrm{st}}$:

$$\vec{F}_{\mathrm{st}} = \begin{bmatrix} 0 & 0 & f_{\mathrm{t}} & y f_{\mathrm{t}} & x f_{\mathrm{t}} & 0 \end{bmatrix}^T \tag{6-10}$$

Both the vector $\vec{F}_{\mathrm{st}}$ and the mass of water inside each flooding tank is passed onto the Motion Module. The mass is required to determine the inertia forces of the flooding tanks. This is further elaborated on in section 7-3.

6-6 Validation Flow Module

Validation and verification of the Flow Module is done using two different tests. In the first test an elementary inflow case is performed to verify the module. Here, the tank geometry of the submerged cylinder is used. No waves are assumed, such that the tank boundary conditions of the raised panel model and double sided panel model (section 5-6) nor the fixed or fluctuating static pressure (section 6-2) has an effect on the results; only hydrostatics are involved. The aim of this test is to verify whether it is valid to average the fluid pressure over each section and the determine the required time step. In order to do this, the analytical solution of the elementary flow case is derived and compared to the simulated tank level.

In the second test, the flooding tank on top of the submerged cylinder is imposed to long regular waves. Due to the presence of the wave, the boundary conditions and static pressure incorporation are taken into account. The four combinations are compared to each other, after which incorrect combinations are eliminated (if any).

6-6-1 Analytical flow case

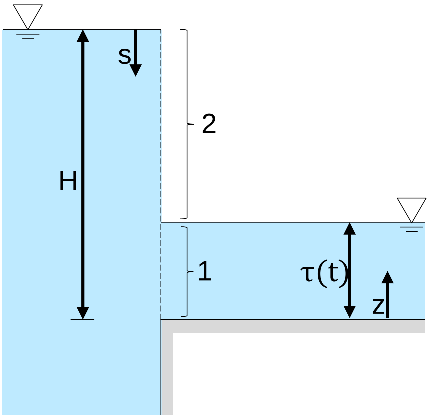

Figure 6-8: *Elementary inflow case*

An elementary but useful flow case is set up for verification of the flow module, see figure 6-8. No waves are assumed in the outer domain, such that a static pressure distribution is present at both sides of the tank boundary. According to the various cases discussed in the beginning of this chapter, the initial condition is similar to case 1, subsequently we should go to case 2 and end with case 6.

The outer surface elevation with respect to the body's top surface is H meter at all times and $\tau(t)$ represents the time varying tank level. The tank boundary is split in two sections; a lower section 1 and an upper section 2. At the lower section, fluid is present at both sides of the boundary such that submerged flow is present. As a consequence the pressure difference is constant over the height. At the upper section, fluid is present at only one side and the pressure difference increases with the submergence s. In case the depth into the paper equals B, the areas of both sections are respectively $A_1(t) = \tau(t)B$ and $A_2(t) = (H - \tau(t))B$. Note that the height of both sections varies in time, due to the increase in tank filling grade. According to equation (6-5), the total discharge $Q(t)$ is given by the sum of the separate discharges through section 1 and 2:

$$Q(t) = C_f \iint_{A_1} v_1(t) dA + C_f \iint_{A_2} v_2(t) dA \tag{6-11}$$

If we apply Bernoulli's equation at both sides of the tank boundary, the inflow velocity at both sections due to a static pressure difference is given by:

$$v_1(t) = \sqrt{2g\left(H - \tau(t)\right)} \qquad \text{(6-12)} \qquad\qquad v_2(s(t)) = \sqrt{2gs(t)} \qquad \text{(6-13)}$$

Here, is can be seen that the $v_1(t)$ is constant over the height of the area and only varies in time. Velocity $v_2(s(t))$ however varies over the height s, measured with respect to the submergence below the outer water level. Substituting the velocity equations into (6-5) and solving the integral gives us the analytical expression for the time varying discharge:

$$\begin{aligned} Q(t) &= C_f \int_0^{\tau(t)} \int_0^B v(t) dy dz + C_f \int_0^{H-\tau(t)} \int_0^B v(s(t)) dy ds & \text{(6-14a)} \\ &= C_f B \left(\sqrt{2g\left(H-\tau(t)\right)}\tau(t) + \frac{2}{3}\sqrt{2g\left(H-\tau(t)\right)}\left(H-\tau(t)\right) \right) & \text{(6-14b)} \end{aligned}$$

Where B is the width of the flow area. Note that if we assume the tank level $\tau(t)$ to be zero at all times (6-14b) changes to the discharge through a rectangular weir, which can be found in many text books on fluid flow such as [21]:

$$Q = C_f B \frac{2}{3} \sqrt{2g} H^{\frac{2}{3}} \qquad \text{(6-15)}$$

Semi-analytical solution

Equation 6-14b gives the analytical expression for the discharge over time, taking into account the varying velocity $v_2(s(t))$ over the height of the flow area. In the numerical model however, the pressure difference for free flow is averaged over the height resulting in an average fluid velocity. To examine the effect of this action a "semi-analytical" expression for the discharge is acquired; here the average velocity is taken into account. The resulting tank levels are compared to each other.

We average the velocity of section 2 by substituting the midpoint of the flow area into $s(t)$ of equation (6-13):

$$s(t) = \frac{H - \tau(t)}{2} \quad \rightarrow \quad v_2(t) = \sqrt{g\left(H - \tau(t)\right)} = \frac{1}{\sqrt{2}}\sqrt{2g\left(H - \tau(t)\right)} \qquad \text{(6-16)}$$

This gives the following semi-analytical expression for the fluid discharge:

$$Q(t) = C_f B \left(\sqrt{2g\left(H-\tau(t)\right)}\tau(t) + \frac{1}{\sqrt{2}}\sqrt{2g\left(H-\tau(t)\right)}\left(H-\tau(t)\right) \right) \qquad \text{(6-17)}$$

Comparing (6-14b) with (6-17) shows that the only difference is given by the fraction in front of the second square root: $\frac{2}{3}$ versus $\frac{1}{\sqrt{2}}$ respectively. The latter being slightly larger suggest that the semi-analytical expression provides a slightly larger discharge.

Resulting tank levels

The increase in tank water level over time $\dot{\tau}(t)$ is given by dividing the discharge $Q(t)$ with the tank surface area A_0, as shown hereafter. Substitution of expression (6-14b) and (6-17) for $Q(t)$ gives two differential equations for the tank water level τ.

$$Q(t) = \frac{dV}{dt} = A_0 \frac{d\tau(t)}{dt} \rightarrow \dot{\tau}(t) = \frac{1}{A_0} Q(t) \tag{6-18}$$

The solutions of both equations is shown in figure 6-9a. Here, the geometry of the cylinder is assumed such that $A_0 = \frac{\pi}{4} D^2$ and $B = \pi D$ for $D = 15m$. Furthermore, $H = 1$, $\tau(t = 0) = 0$ and $C_f = 0.6$. It can be seen that the semi-analytical approach indeed shows a slightly larger discharge. The overall effect however is insignificant, implying the average velocity approach for the numerical model to be valid.

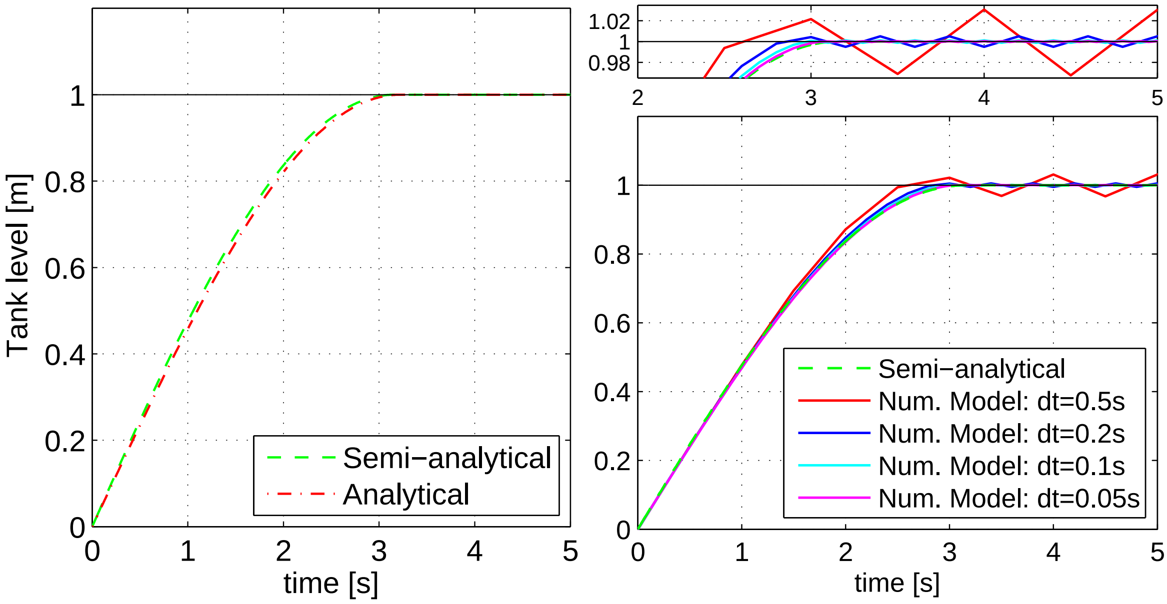

(a) *Tank level for the full and semi-analytical solution.* **(b)** *Tank inflow for a variation of time steps.*

Figure 6-9: *Resulting tank level for an elementary inflow case.*

6-6-2 Time step convergence

The flow module calculates the tank level of each tank at each time step. Therefore the time step size must be carefully selected for computational efficiency, numerical stability and convergence. Based on the same elementary flow case, the effect of the time step is examined and shown in figure 6-9b.

In general it can be observed that the numerical model approaches the semi-analytical solution for decreasing time step size. In the enlargement shown at the top it is clearly visible that the solution of the numerical model for $dt = 0.5$ and $dt = 0.2$ does not fully converge to the outer surface elevation of 1 m. Instead, it fluctuates around 1 m.

This fluctuation is caused by the fixed outer surface elevation. As soon as the tank level approaches this level, too much water will flow into the tank than required due to the long time interval. As a consequence the tank level does not equal the outer surface elevation, but it is slightly higher at the subsequent time step. Subsequently, too much water flows out of the tank due to the large time interval and the tank level is slightly lower, and so on. For smaller time steps the fluctuating behavior reduces. This phenomena can be removed by regulating the maximum flow as soon as the tank level approaches the outer surface elevation. However, in case waves are present in the outer domain, the outer surface elevation varies in time and this phenomena disappears. The resulting tank levels for a time step of 0.1 s and 0.05 s are nearly identical to the semi-analytical solution. Therefore, a time step of 0.1 s is chosen in further analysis.

6-6-3 Low frequency limit

In the second test, long waves are imposed to the flooding tank. The flooding tank on top of the submerged cylinder is used again. Intuition says that for very long waves the tank level should follow the outer surface elevation. Due to the presence of waves, the free surface elevation and the dynamic pressure on the outer side of the tank boundary vary. These are taken into account by the tank boundary conditions as discussed in section 5-6. Both the raised panel model and double panel model are used, combined with the fixed and fluctuating static pressure. This results in a total of four combinations.

A wave height of 1 m and a frequency of approximately 0.2 rad/s is used (i.e. a period of 30 s). For deep water waves this corresponds to a wave length of approximately 1500 m, which is long compared to the cylinder's diameter of 15 m.

Figure 6-10 shows the resulting tank level for each combination. It is clearly visible that the tank level does not follow the wave in case the fluctuating static pressure model is used. The tank levels are over predicted at wave crests and the tanks even runs dry at the trough. For the fixed static pressure the expected result is acquired.

6-6-4 Conclusions validation tests

At the first validation test, an elementary inflow case is used. Purpose of this test was to verify whether it is valid to average the fluid pressure over each section and the determine the required time step. A full analytical solutions and a semi-analytical solution including the average pressure distribution are compared to each other. This showed that the effect of the average pressure is insignificant. Therefore, the average pressure over each section is used in further analysis.

Subsequently, the same elementary flow case is used to determine the time step. The solutions of the numerical model using a time step of 0.5 s, 0.2 s, 0.1 s and 0.05 s are compared to the semi-analytical solution. The largest two time steps resulted in a clearly visible fluctuation of the final tank level. For the smaller two time steps this effect reduced. A final time step of 0.1 s is chosen for further analysis.

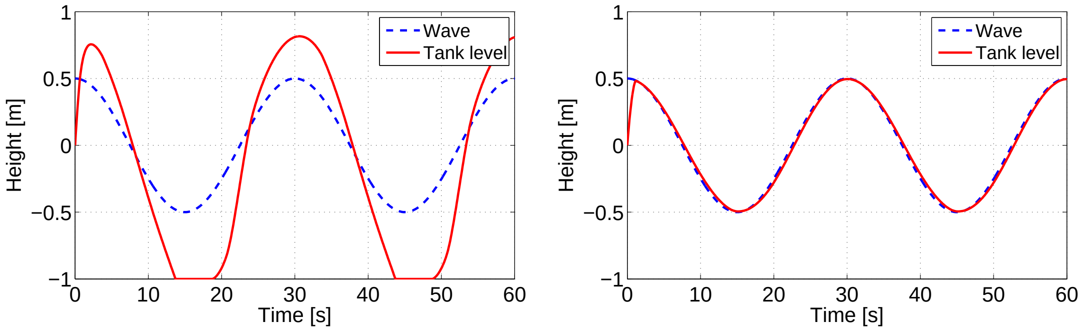

(a) *Raised panel model, fluc. static pressure* **(b)** *Raised panel model, fixed static pressure*

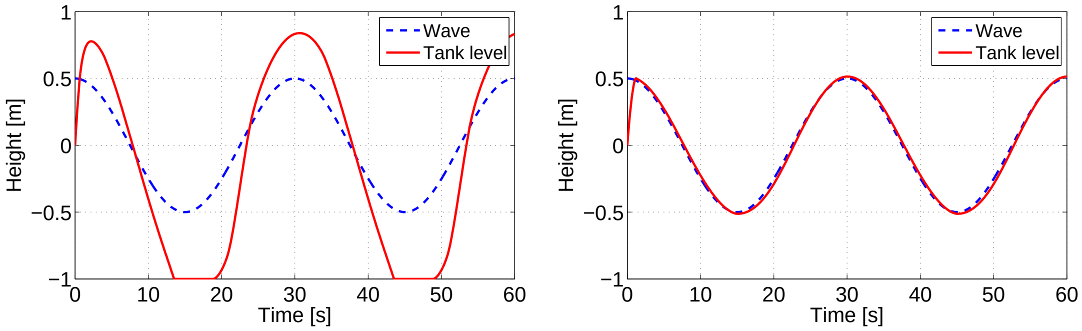

(c) *Double panel model, fluc. static pressure* **(d)** *Double panel model, fixed static pressure*

Figure 6-10: *Low frequency limit. Wave measured at origin,* $H = 1m$ *and* $\omega = 0.21rad/s$.

In the second test, long waves were imposed to the Flow Module. Here, the tank geometry and boundary conditions of the submerged captive cylinder were used. The raised and double panel model in combination with the fluctuating and static pressure incorporation are all compared, resulting in four combinations. The low frequency simulations showed that the incorporation of the fluctuating static pressure does not give the expected tank level for both panel models; the tank levels are over predicted. In case the fixed static pressure is used, the tank levels follow the regular wave as expected. Therefore, it can be stated that the fluctuating static pressure gives incorrect results and will not be used in further analysis. Further analysis is performed using the fixed static pressure.

Chapter 7

Implementation of the Motion Module

The main component of the time-domain simulation is the Motion Module. This module is used to solve the equations of motions using a numerical time integration scheme. Prior to solving these equations for a given time step, it passes the orientation of the body onto the Flow Module. This module in turn returns the force exerted by the flooding tanks on the top surface of the body and the mass of water inside each tank.

Subsequently, the retardation functions are evaluated with the velocity of the body. Thereafter a 4$^{\text{th}}$ order Runge-Kutta scheme is used to solve the equations of motion for a given time step. Output is the new orientation of the body. The latter is passed onto the Flow Module again during the new time step.

The Motion Module takes into account six degrees of freedom:

$$\vec{x} = \begin{bmatrix} x & y & z & \phi & \theta & \psi \end{bmatrix}^T \tag{7-1}$$

Indicating surge, sway, heave, roll, pitch and yaw. The flooding tanks contribute to the heave, roll and pitch motions only. The following equations of motion are solved by the Motion Module:

$$M\ddot{\vec{x}}(t) = \vec{F}^*_{diff} + \vec{F}^*_{rad} + \vec{F}_{rest} + \vec{F}_{tank} + \vec{F}_{add} \tag{7-2}$$

The term $\vec{F}^*_{diff}$ are the forces induced by the incoming and diffracted waves on the still body and $\vec{F}^*_{rad}$ are the radiation forces on an oscillating body in still water. The star* indicates that only the outer surface is taken into account. Furthermore, $\vec{F}_{rest}$ are the restoring spring forces, $\vec{F}_{tank}$ are the forces exerted by the flooding tanks on the remaining top surface and $\vec{F}_{add}$ involves additional viscous damping.

The wave forces $\vec{F}^*_{diff}$ follow from the radiation diffraction analysis and are already discussed in chapter 5. The only remark to be made on $\vec{F}^*_{diff}$ is that, due to time constraints of this work, the incorporation of the wave forces is simplified by assuming that no phase shift is present due to a surge or sway motion. Additionally, no wave force dependency on the yaw angle is taken into account.

The term $\vec{F}_{add}$ involves additional damping due to viscosity. Only diagonal terms are taken into account, whereas the values are based on in-house experience of HMC.

The remaining force components are discussed in the upcoming sections.

7-1 Radiation Forces

Due to motions of the body, waves are generated at the free surface. The radiation forces $\vec{F}^*_{rad}$ are due to energy carried away by generated surface waves [23]. In frequency-domain calculations, $\vec{F}^*_{rad}$ can be split into two components: hydrodynamic inertia forces $A(\omega)\ddot{\vec{x}}$ and damping forces $B(\omega)\dot{\vec{x}}$. Here, $A(\omega)$ and $B(\omega)$ are respectively the frequency-dependent added mass and damping coefficients and are obtained from the radiation diffraction analysis. Acquiring $A(\omega)$ and $B(\omega)$ specifically for the outer surface is discussed in section 5-1.

The added mass and damping coefficients are used in the frequency-domain equations of motion. To use them in time-domain calculations, it can be stated that a wave generated at a certain time moment will, in principle, persist at all subsequent times affecting the motions of the body. This effect is known as fluid memory. [24] showed that the fluid memory effect can be captured in a convolution integral involving the velocities $\dot{\vec{x}}$ and a matrix of retardation functions R:

$$\vec{F}_{rad} = -A\ddot{\vec{x}}(t) - \int_0^\infty R(\tau)\dot{\vec{x}}(t-\tau)d\tau \tag{7-3}$$

where A is the frequency independent added mass, t is the current time step and τ are the previous time steps. Note that τ is not the filling grade as used in all other chapters; this notation is used here to remain consistent with literature. In the work of [24], A and R followed from two additional velocity potentials.[25] showed that the radiation forces in the time-domain can be related to the frequency-domain added mass and damping coefficients:

$$R(\tau) = \frac{2}{\pi}\int_0^\infty B(\omega)\cos(\omega\tau)d\omega \tag{7-4}$$

$$A = A(\omega) + \frac{1}{\omega}\int_0^\infty R(\tau)\sin(\omega\tau)d\tau \tag{7-5}$$

The numerical computations involved to evaluate the retardation functions are incorporated in the in-house developed time-domain script which is used for the Motion Module.

7-2 Restoring Forces

The hydrostatic reaction or restoring forces $\vec{F}_{rest}$ follow from the underwater geometry of the body and its mass distribution. In linear theory $\vec{F}_{rest}$ is given by:

$$\vec{F}_{rest} = -C\vec{x} \tag{7-6}$$

in which C is a six-by-six matrix including restoring spring coefficients.

The coefficients of C can be deduced by considering a forced motion and analyzing the resulting changes in buoyancy forces due to hydrostatic pressures. For both the cylinder as the SSCV at inconvenient draft, it was observed that part of the underwater geometry emerges occasionally. As a consequence the resorting forces become non-linear. In the numerical model $\vec{F}_{rest}$ is considered as linear, whereas the flooding tanks are used to capture the non-linear behavior. This will be explained according to figure 7-1. Three different conditions of an arbitrary body are shown here:

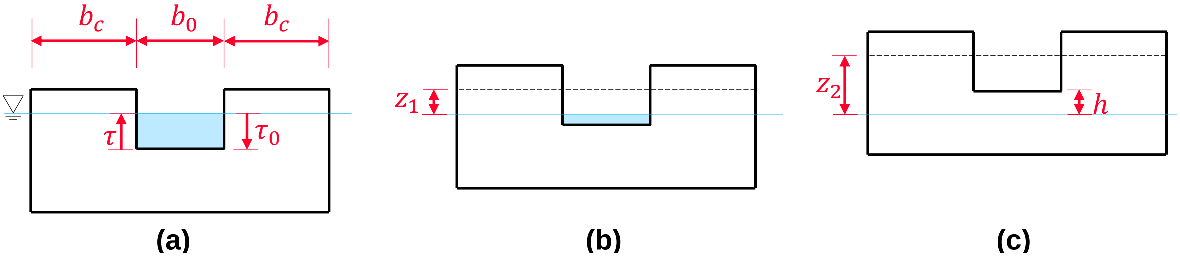

Figure 7-1: *Three conditions indicating emergence of the body.*

The left figure depicts the equilibrium or initial position. Two columns of width b_c pierce the water surface. If the depth into the paper is considered as unity, the water plane area A_{wl} equals $2b_c$. In between the columns a flooding tank is located with a width b_0 and bottom surface area A_0. The tank filling grade τ equals the submergence of the bottom surface below the still water level τ_0, such that no tank force is exerted on the body (according to equation (6-9) at section 6-5). For clarity, the equation for the vertical tank force is repeated here:

$$f_t = \rho g \left(\tau_0 - \tau\right) A_0 \tag{7-7}$$

At the second figure the body is moved upward with a distance z_1. The restoring force due to a change in buoyancy is equal to $-\rho g A_{wl} z_1$, where the minus sign indicates that the force is directed downwards. The amount of water inside the tank is reduced, such that it equals the still water level again and no tank force is present.

At the third figure the body moved further upward to a distance z_2. In this case the part of the body within the two columns is emerged. The linear restoring force equals $-\rho g A_{wl} z_2$. The tank level $\tau = 0$, whereas the submergence of the bottom surface below the still water level $\tau_0 = -h$ (the minus sign indicates a negative submergence, i.e. emergence). As a result the total force on the body is given by:

$$\begin{aligned} F_{total} &= -\rho g z_2 A_{wl} + \rho g \left(\tau_0 - \tau\right) A_0 && \text{(7-8a)} \\ &= -\rho g z_2 A_{wl} - \rho g h A_0 && \text{(7-8b)} \end{aligned}$$

Here, the first component on the right hand side is the linear part due to the restoring spring term and the second component is the non-linear part due to emergence of the body. This latter component is incorporated in $\vec{F}_{tank}$.

7-3 Tank Inertia

The force exerted by the water in the flooding tanks $\vec{F}_{tank}$ is build up out of two components; a static force $\vec{F}_{st}$ due to the mass of the water and a dynamic component due to inertia:

$$\vec{F}_{tank} = \vec{F}_{st} - M_t \ddot{\vec{x}}(t) \tag{7-9}$$

The static component $\vec{F}_{\text{st}} = \begin{bmatrix} 0 & 0 & f_{\text{t}} & yf_{\text{t}} & xf_{\text{t}} & 0 \end{bmatrix}^T$ is provided by the Flow Module and already discussed in section 6-5. The dynamic component follows from the tank mass matrix M_t times the acceleration of the body $\ddot{\vec{x}}$.

The mass matrix M_t is a six-by-six matrix including tank masses and moments of inertia. Here, no coupling terms are taken into account. Since the tanks only affect the heave, roll and pitch motions of a body, the only non-zero elements of M_t are the third, fourth and fifth diagonal terms. The third term, related to heave, is given by the sum of the tank masses. To determine the fourth and fifth term, related to respectively the roll and pitch mass moment of inertia around the axis through an arbitrary point of interest, use is made of the parallel axis theorem or Steiner theorem:

$$I = I_{cm} + md^2 \tag{7-10}$$

in which I_{cm} is the moment of inertia relative to the axis through the center of mass of the water itself, m is the mass, d is the perpendicular distance between the axis through the center of mass of the water and the axis through the rotation point of interest and I is the moment of inertia with respect to this latter axis. Due to the horizontal tank assumption, the first term in equation (7-10) is zero at all times and only the Steiner summand md^2 remains. As a result the following terms are used for M_t:

$$M_{t,33} = \sum_{i=1}^{N} m_i \qquad M_{t,44} = \sum_{i=1}^{N} m_i d_{y,i}^2 \qquad M_{t,55} = \sum_{i=1}^{N} m_i d_{x,i}^2 \tag{7-11}$$

where, m_i is the mass of the i-th tank, $d_{y,i}$ is the distance to the body fixed y-axis and $d_{x,i}$ is the distance to the body fixed x-axis. Subsequently, the mass matrix M_t is multiplied by the current acceleration of the body $\ddot{\vec{x}}$ to acquire the dynamic tank force, after which it is applied to the body as an external force.

7-4 Numerical Integration Scheme

Substitution of all the force components into the equations of motion results into the following expression:

$$(M+A)\ddot{\vec{x}}(t)+B_{add}\dot{\vec{x}}(t)+C\vec{x}(t)=\vec{F}^{*}_{diff}-\int_{0}^{\infty}R(\tau)\dot{\vec{x}}(t-\tau)d\tau+\vec{F}_{st}-M_t\ddot{\vec{x}}(t) \quad (7\text{-}12)$$

Equation (7-12) is solved using an in-house developed script based on the 4th-order Runge-Kutta scheme. In order to do this, equation (7-12) is written as the following matrix-vector equation:

$$\vec{q}=\begin{bmatrix}\vec{x}\\ \dot{\vec{x}}\end{bmatrix} \qquad \text{and} \qquad \dot{\vec{q}}=\begin{bmatrix}\dot{\vec{x}}\\ \ddot{\vec{x}}\end{bmatrix} \quad (7\text{-}13)$$

$$\dot{\vec{q}}=M^{-1}\begin{bmatrix}0 & I\\ -C & -B_{add}\end{bmatrix}\vec{q}+M^{-1}\begin{bmatrix}0\\ \vec{F}^{*}_{diff}-\vec{F}_{rtd}+\vec{F}_{tank}\end{bmatrix} \quad (7\text{-}14)$$

where I is a six-by-six identity matrix and $\vec{F}_{rtd}$ includes the integral with retardation functions. The full details of the script are left out of consideration here, only a brief description of the involved steps is given. The following actions are performed:

1. Determine current acceleration:

$$\ddot{\vec{x}}(t_n)=M^{-1}F(t_{n-1}) \quad (7\text{-}15)$$

2. Make guess on velocity:

$$v(t_{n+1})=\dot{\vec{x}}(t_n)+\ddot{\vec{x}}(t_n)\Delta t \quad (7\text{-}16)$$

3. Evaluate retardation functions:

$$\vec{F}_{rtd}=-\int_{0}^{\infty}R(\tau)\dot{\vec{x}}(t-\tau)d\tau \quad \text{where} \quad \dot{\vec{x}}(t-0)=v(t_{n+1}) \quad (7\text{-}17)$$

4. Solve equation (7-14) using 4th-order Runge-Kutta scheme:

$$\vec{q}_{n+1}=\vec{q}_n+\frac{1}{6}\left(k_1+2k_2+2k_3+k_4\right) \quad (7\text{-}18)$$

5. Difference between $v(t_{n+1})$ and $\dot{\vec{x}}(t_{n+1})$ smaller than threshold ϵ?

$$\left|v(t_{n+1})-\dot{\vec{x}}(t_{n+1})\right|<\epsilon \quad (7\text{-}19)$$

6. If false: return to step 3 and evaluate retardation functions with $\dot{\vec{x}}(t_{n+1})$;
   If true: continue to the next time step.

Finally, the time trace of the motions $\vec{x}$ is obtained.

7-5 Validation of the Motion Module

The Motion Module is validated by comparing the calculated RAOs from the Motion Module with the motion RAOs acquired by WAMIT directly. Here, the SSCV Thialf is used at transit draft and a wave direction $\mu = 90^\circ$ (i.e. beam waves). No flooding tanks are defined, such that the Flow Module can be disregarded; the static and dynamic components of the tank force $\vec{F}_{tank}$ are zero at all times.

First a radiation diffraction analysis is performed using WAMIT. The original geometry of the vessel, including the mass matrix M and additional damping matrix B_{add} are given as input. Output of the analysis are the motion RAOs of the vessel in beam waves.

Subsequently, a second radiation diffraction analysis is performed as part of the numerical model. Input is the geometry the vessel only, output are the radiation and diffraction pressures on all panels of the panel model. The pressures are integrated over the full wetted surface of the body to acquire the wave and radiation forces, as described in chapter 5. The wave force RAOs are used to obtain the wave force time traces. The radiation forces are converted to the added mass and damping coefficients. These coefficients in turn are used to obtain the frequency independent added mass and the retardation functions. Subsequently, the time-domain simulation is executed according to the scheme presented in section 7-4.

7-5-1 Standing waves

During both the first and second radiation diffraction analysis, large standing waves are observed between the two pontoons for sway, roll and yaw motions. In reality the non-linear effects in the waves, like breaking, tends to reduce the extreme waves [26]. However, linear potential theory over estimates this resonance behavior. As a consequence, sharp peaks are present at 1 rad/s in the added mass and damping coefficients. The peaks in the coefficients are shown in figure 7-2 for roll motions.

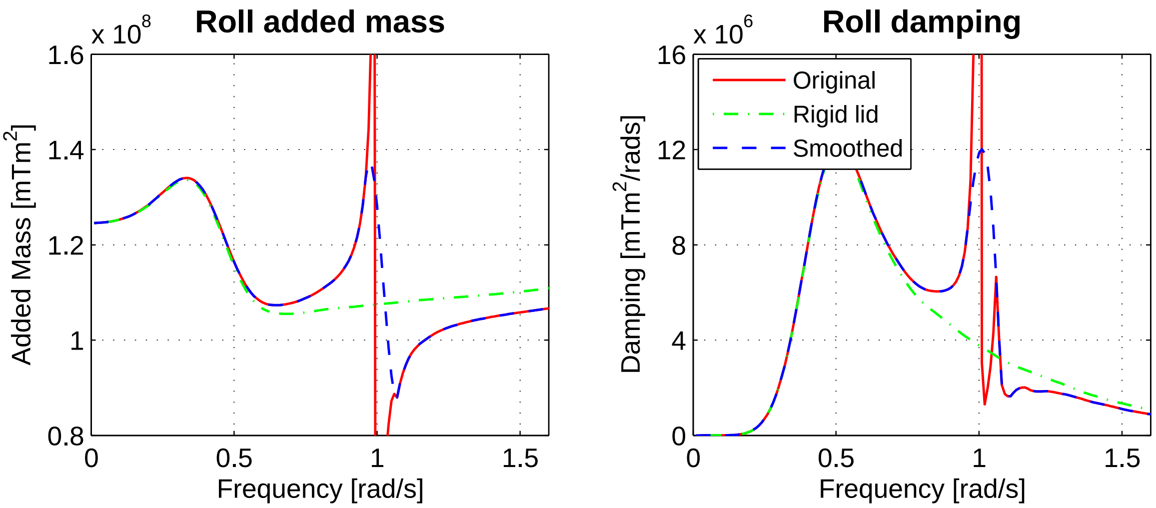

Figure 7-2: *Smoothing applied*

For the motion RAOs obtained by WAMIT directly, the standing waves do not affect the results significantly, since they are present at only one frequency component. Unfortunately, the time-domain simulation is heavily affected; the retardation functions do not convergence to zero due to the sharp peaks in the hydrodynamic coefficients. As a result the time-domain simulation becomes unstable. Three options are found to be available which might resolve this problem:

1. Smooth or truncate the peaks in the hydrodynamic coefficients;
2. Add a rigid lid between the pontoons during the radiation diffraction analysis;
3. Add a damping lid between the pontoons during the radiation diffraction analysis.

The first option is a more pragmatic approach. It is only applied to the sway, roll and yaw coefficients, including the coupling terms. In this option the peak in the acquired coefficients is located and subsequently the peak and a certain interval around the peak is deleted. The blank spots at the deleted interval are replaced by spline interpolation. The smoothed coefficients for roll are shown in figure 7-2. Interpolation of the added mass terms result in both the positive and negative peak near 1 rad/s being truncated. At the damping coefficients only one peak is present and truncated.

At the second option, a rigid lid is applied at the radiation diffraction analysis. This rigid lid is located at the still water surface between the pontoons and suppresses the standing waves completely. In figure 7-2 it can be observed that the peak in the coefficients has disappeared, as if no standing waves are present. The overall suppression of the free-surface elevation between the pontoons makes this option unsuitable for the numerical model. In case flooding tanks are present, the lid suppresses the tank boundary conditions as well. Besides, the wave forces are affected. Because of these reasons, the rigid lid option is not used in further analysis.

The third method is a more scientific or academic approach. Application of a damping lid is found in literature, e.g. at side-by-side offloading problems in [26] and [27]. Here it was found that the damping lid is most effective in reducing the second-order wave drift forces at the resonant peaks. Tuning the damping value of the lid has less effect on the first-order quantities, like absolute wave heights and motion RAOs. In this thesis work, a damping lid approach is not executed due to time constraints.

Finally the first option, smoothing of the peaks, is applied in the numerical model.

7-5-2 SSCV at transit draft

The time-domain simulation using the SSCV Thialf at transit draft in beam waves is executed, where the retardation functions follow from the smoothed hydrodynamic coefficients. The significant wave height and wave peak period are respectively 3 m and 20 s. The motion RAO for heave and roll are shown in figure 7-3. Both the RAO directly from WAMIT and the RAO calculated by the Motion Module are depicted.

It can be observed that the time-domain simulation is able to reproduce the WAMIT RAOs. The smoothing applied on the hydrodynamic coefficients does not affect the

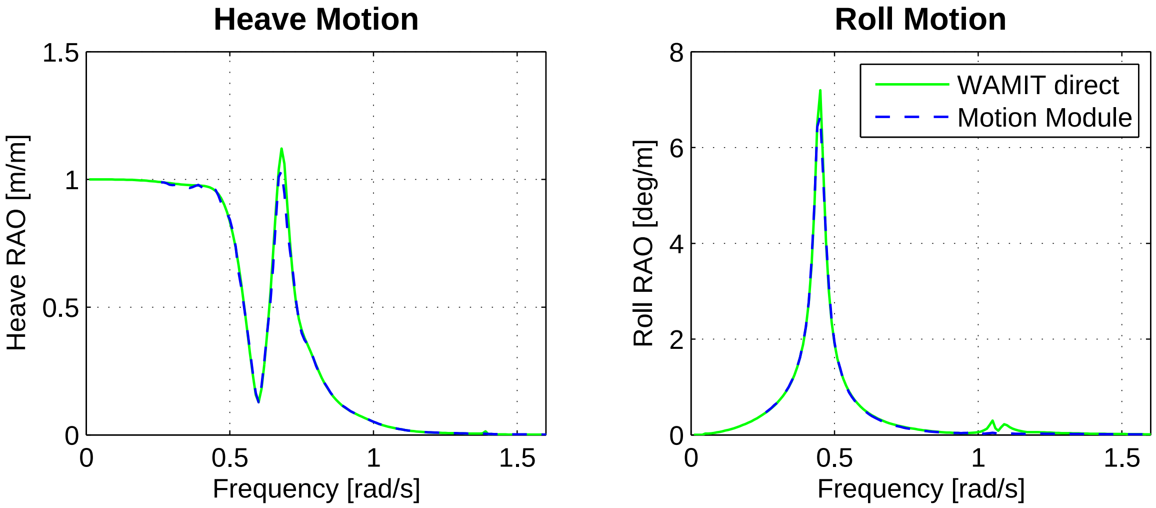

Figure 7-3: *Heave and roll RAO of SSCV Thialf at transit draft (13.3m in beam waves).*

overall result. Only minor discrepancy can be observed at a frequency just above 1 rad/s for roll and at both the peaks. It can be concluded that the Motion Module works as expected.

7-6 Coupling with the Flow Module

Three test cases are used to verify the coupling with the Flow Module. First case is an imposed positive roll moment, second case is an imposed negative heave force and the last case is an imposed positive heave force. No waves are present in each case, such that the resulting tank flow follows from the hydrostatic pressure only. The SSCV Thialf at 14.5 m draft is used as initial condition. This implies an initial tank filling grade of 0.9 m. The tank configuration is shown in figure 7-4:

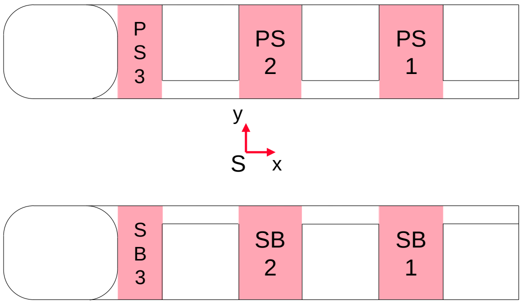

Figure 7-4: *Tank configuration SSCV Thialf.*

i	Name	x_i [m]	y_i [m]	A_i [m^2]
1	PS1	48.68	30.2	532.0
2	PS2	6.88	30.2	532.0
3	PS3	-32.07	30.2	372.4
4	SB1	48.68	-30.2	532.0
5	SB2	6.88	-30.2	532.0
6	SB3	-32.07	-30.2	372.4

Table 7-1: *General tank properties.*

Three rectangular tanks are used on top of each pontoon. The small strips next to the columns are disregarded. The general tank properties are shown in table 7-1. Here x_i and y_i are the coordinates of the center of the i-th tank with respect to the origin S of the ship fixed coordinate system and A_i is the ground plane area of the i-th tank.

7-6-1 Imposed roll moment

At the first test case a positive roll moment M_x of $2.75 \cdot 10^5$kNm is imposed to the SSCV. This should result in a positive roll angle and consequently submergence of the starboard pontoon. The left graph of figure 7-5 shows a resulting positive roll angle of 0.81°. The right graph shows that the tank level of the starboard tanks increase due to submergence of the pontoon. The port side tank levels decrease since this pot side pontoon is raised.

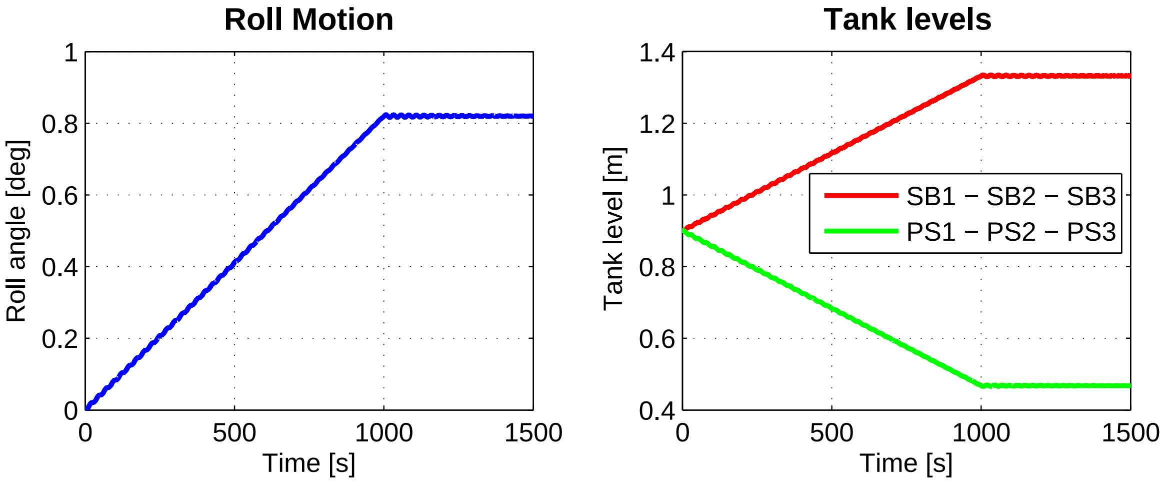

Figure 7-5: *Tank levels for an imposed roll moment.*

A verifying hand calculation shows a roll angle φ of:

$$\varphi = \frac{M_x}{C_{44}} = \frac{2.75 \cdot 10^5}{1.94 \cdot 10^7} \frac{\text{kNm}}{\text{kNm/rad}} = 0.014\,\text{rad} = 0.81^\circ \tag{7-20}$$

in which C_{44} is the roll stiffness coefficient. The corresponding tank level τ_i of the i-th tank is given by:

$$\begin{aligned} \tau_i &= \tau_i(t_0) - z + \quad x_i \sin(\theta) - \quad y_i \sin(\varphi) \\ \tau_{\text{SB1}} &= 0.9 \quad\; - 0 + 48.68 \sin(0) + 30.2 \sin(0.81) = 1.33\,\text{m} \\ \tau_{\text{PS1}} &= 0.9 \quad\; - 0 + 48.68 \sin(0) - 30.2 \sin(0.81) = 0.47\,\text{m} \end{aligned} \tag{7-21}$$

The tank levels from the time-domain simulation are in accordance with the hand calculation.

7-6-2 Imposed heave force

A similar calculation is performed in the second test case. Here, a heave force F_z of $-5.13 \cdot 10^4$kN is applied at the origin S of the ship fixed coordinate system. The center of flotation is located at $x = -3.69\,\text{m}$ and $y = 0\,\text{m}$, resulting in a heave-pitch coupling being present. The positive moment is induced by the heave force, such that the SSCV Thialf is slightly trimmed forward. The tank levels in tank PS1 and SB1 should be the highest, whereas PS3 and SB3 should be lowest. Figure 7-6 shows the heave motion and the tank levels for the second test case:

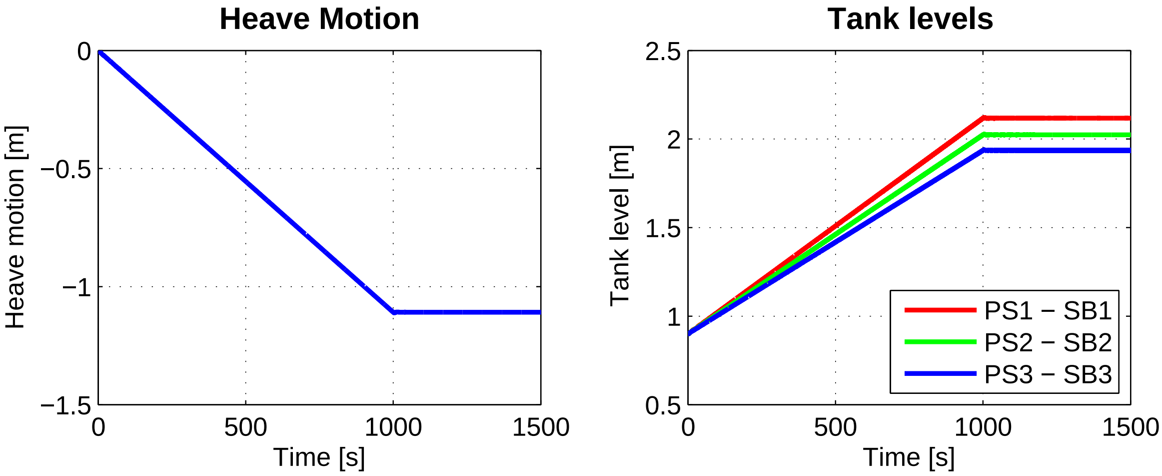

Figure 7-6: *Tank levels for an imposed heave force, including pitch coupling*

The tank levels of the forward, mid and aft tanks are as expected. Hand calculation shows a resulting heave motion z and pitch angle θ of:

$$z = \frac{F_z}{C_{33}} = \frac{-5.13 \cdot 10^4}{4.66 \cdot 10^4} \frac{\mathrm{kN}}{\mathrm{kN/m}} = -1.1\,\mathrm{m} \tag{7-22}$$

$$\theta = \frac{F_z x_{cof}}{C_{55}} = \frac{-5.13 \cdot 10^4 \cdot -3.69}{8.46 \cdot 10^7} \frac{\mathrm{kN \cdot m}}{\mathrm{kNm/rad}} = 0.13^\circ \tag{7-23}$$

By making use of equation (7-21), the resulting tank levels become:

$$\begin{aligned}
\tau_{\mathrm{PS1}} &= 0.9 + 1.1 + 48.68 \sin(0.13) - 30.2 \sin(0) = 2.11\,\mathrm{m} \\
\tau_{\mathrm{PS2}} &= 0.9 + 1.1 + \ \ 6.88 \sin(0.13) - 30.2 \sin(0) = 2.01\,\mathrm{m} \\
\tau_{\mathrm{PS3}} &= 0.9 + 1.1 - 32.07 \sin(0.13) - 30.2 \sin(0) = 1.93\,\mathrm{m}
\end{aligned}$$

These hand calculated tank levels are in accordance with the simulated tank levels.

7-6-3 Non-linear stiffness

At the last test case a positive heave force is applied to the SSCV Thialf, such that the pontoons emerge from the water surface. As a result the restoring force becomes non-linear. In the numerical model, the linear part of the restoring force is taken into account by the conventional hydrostatic spring terms. The non-linear part of the restoring force is taken into account by the flooding tanks, as explained in section 7-2.

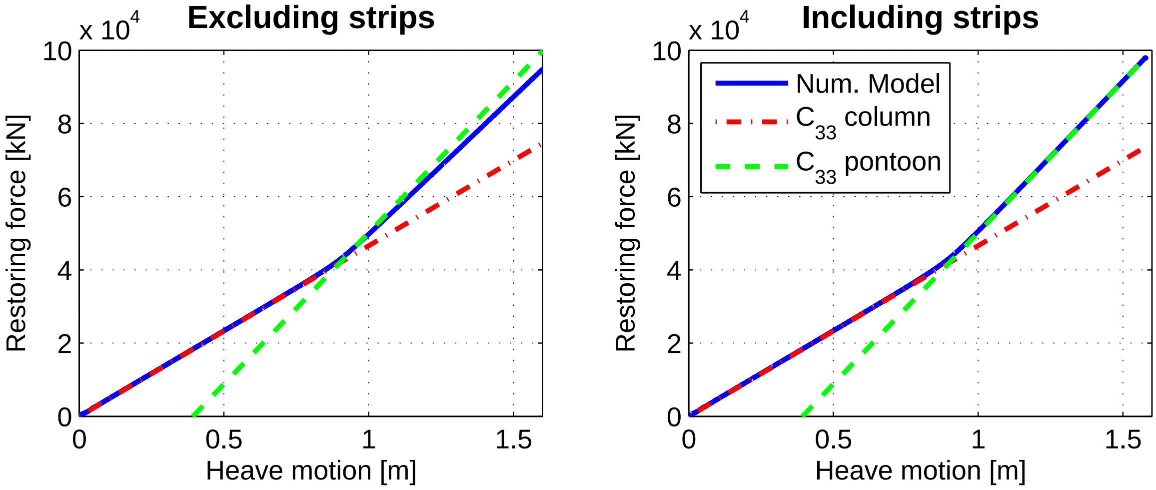

Figure 7-7: *Nonlinear force-displacement curve for heave motions. Left graph shows the curve excluding the small strips next to the columns, according to figure 7-4. In the right graph the area of the strips is included in the tank areas.*

The resulting force-displacement curve for the third test case is shown in the left graph of figure 7-7.

Two additional lines are shown here. The red dash-dot line has a slope which equals the heave stiffness coefficient C_{33} at column draft, whereas the green dashed line has a slope equal to pontoon draft. It can be observed that for increasing heave motion, the slope equals the slope of column stiffness until approximately 0.9 m. At this point the pontoons emerge from the water surface and the flooding tanks run dry. As a result the slope increases and approaches the pontoon stiffness.

In the left graph, a small discrepancy can be observed between the calculated slope and the theoretical slope for pontoon stiffness. This discrepancy is caused by the strips next to the columns which are disregarded, as was shown in figure 7-4. In the right graph, the areas of these strips are included in the tank areas. In this case the calculated slope equals the slope corresponding to pontoon stiffness.

Chapter 8

Application of the Numerical Model

Now that the implementation of both the Flow Module and the Motion Module is discussed, it is time to use the numerical model. The model will firstly be applied to the captive submerged cylinder. By using a captive body in the numerical model, all terms in the equations of motion including motions, velocities or accelerations are zero at all times. As a result, the wave forces on the outer surface and tank force on top surface are the only remaining components.

Two sets of time-domain simulations are performed with the captive cylinder. Firstly regular waves simulations are done to acquire time traces of the heave forces. These time traces are compared to the time traces of the in-house CFD simulations. The main findings are discussed. Secondly, irregular wave simulations are performed. The acquired force time trace is used to calculate the spectral density function of the response, which in turn are used to calculate the RAOs and phases. The force RAOs and phases for surge and heave are compared to the model test results.

Subsequently the numerical model is applied to the freely-floating SSCV Thialf at inconvenient draft. The diffraction forces on the outer surface, hydrodynamic coefficients and tank boundary conditions are acquired from the radiation diffraction analysis and discussed briefly. Subsequently the results from the time-domain simulation are shown. Six degrees of freedom are taken into account in the simulation, whereas only heave and roll are shown here. The results are discussed at the end of this chapter.

All simulations are done for both the raised panel model as the double panel model.

8-1 Captive Submerged Cylinder

The perform the time-domain simulation using the captive submerged cylinder, the wave forces on the outer surface and the tank boundary conditions are required. The tank boundary conditions consists of the surface elevation RAOs in front of the flooding tanks, and the wave-induced pressure RAOs on the outer side of the tank boundary. These quantities follow from the radiation diffraction analysis and are already discussed in chapter 5. In oder to avoid page scrolling back and forth to this chapter, the wave forces on the outer surface in heave direction and the surface elevation RAOs are rediscussed briefly. The wave-induced pressure RAOs are not discussed here.

Figure 8-1 depicts the wave force RAOs and phases in heave direction for both panel models, on the outer surface. The raised panel model shows a gradual decline of the heave force RAO for increasing frequency. The phase shift between the undisturbed wave increases from 0° to approximately 135°.

The double panel model shows the same declining trend in the heave force RAO. However, a phase shift in present at approximately 0.8 rad/s. This phase shift is caused by the pumping mode, due to water being captures inside the double walled cylinder.

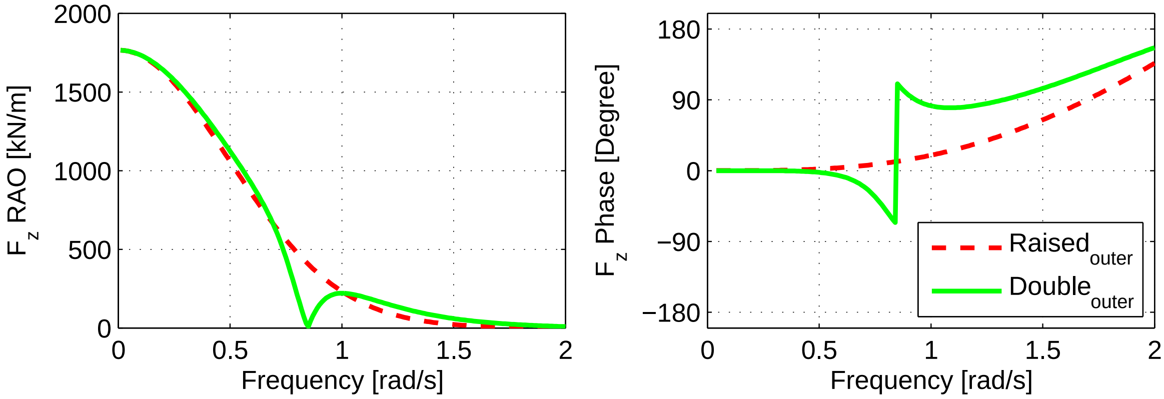

Figure 8-1: *Heave force RAOs and phase on the outer surface of the raised and double panel model.*

Figure 8-2 shows the surface elevation RAOs of the two panel models at three locations. At the leading edge 0°, the side edge 90° and the trailing edge 180° of the cylinder. The left graph shows the surface elevations for the raised panel model. At the leading edge it can be observed that the surface elevation approaches 2 m/m for higher frequencies, since the raised cylinder acts as a reflecting wall. The surface elevation RAO at the trailing edge reduces for increasing frequency, which may be assigned to shielding effects.

The surface elevation RAOs of the double panel model are shown in the right graph. Here, the pumping mode which causes the phase shift in heave force can be observed at 0.8 rad/s. At higher frequencies, the surface elevations RAO vary significantly more compared to the RAOs of the raised panel model.

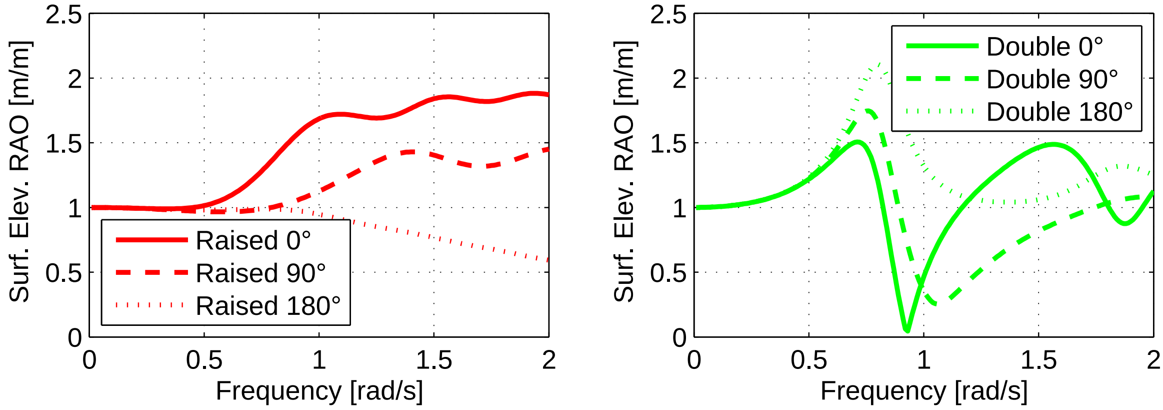

Figure 8-2: *Surface elevation RAOs for diffraction at three locations for both panel models.*

As discussed in chapter 5, both the wave force RAOs and the tank boundary conditions are obtained in frequency-domain calculations. They are converted to time signals to use them in the time-domain simulation.

8-1-1 Regular waves

A number of regular wave simulations is performed. Here, the wave height varied between 1 m, 2 m and 4 m and the wave frequency varied from 0.59 rad/s to 0.95 rad/s in steps of 0.16 rad/s. This results in a total of 15 simulations for both the raised and the double panel model. Output of these simulations is a time trace of the total vertical force on the cylinder, i.e. the sum of the tank force and wave force. Subsequently, these time traces are compared with in-house developed CFD time traces from [2]. It should be noted that no information was present of the waves used in the CFD simulations. Therefore the time traces are synchronized to each other based on the surge force time traces.

The acquired time traces are shown in appendix C. For each combination of wave height and frequency, two graphs are shown corresponding to the raised and double panel model. Each graph shows two time traces; first one of the CFD calculation, second one of the numerical model. A flow coefficient of 0.6 is used here.

Main observations

Results for a wave heights of 1 m are shown in figure C-1. The raised panel model shows for each frequency too small amplitudes compared to the CFD results. The double panel model shows better results. Spot on results for the two smallest frequencies are found. For 0.73 rad/s the troughs are slightly over estimated. At the two highest frequencies the amplitudes are correct, however a phase shift is present.

Figure C-2 shows the time traces of 2 m wave height. The raised panel model shows too small amplitudes for this wave height as well, however to a lesser extend as was observed for 1 m waves. Again, good results are found for the double panel model at the three smallest frequencies, but a small discrepancy is introduced in the troughs. The same phase shift is present at the two highest frequencies.

Time traces for a wave heights of 4 m are shown in figure C-3. The raised panel model shows good results, although non of the time traces is spot on. The double panel model captures the non-linear trends, however the trough are even more over estimated for all frequencies. The phase shift is again present at the two highest frequencies.

Discussion

At the regular wave time traces, two recurring phenomena are found. Firstly, a phase shift is present in the time traces of the double panel model at frequencies higher than 0.75 rad/s. An example is shown for one wave combination in the left graph of figure 8-3.

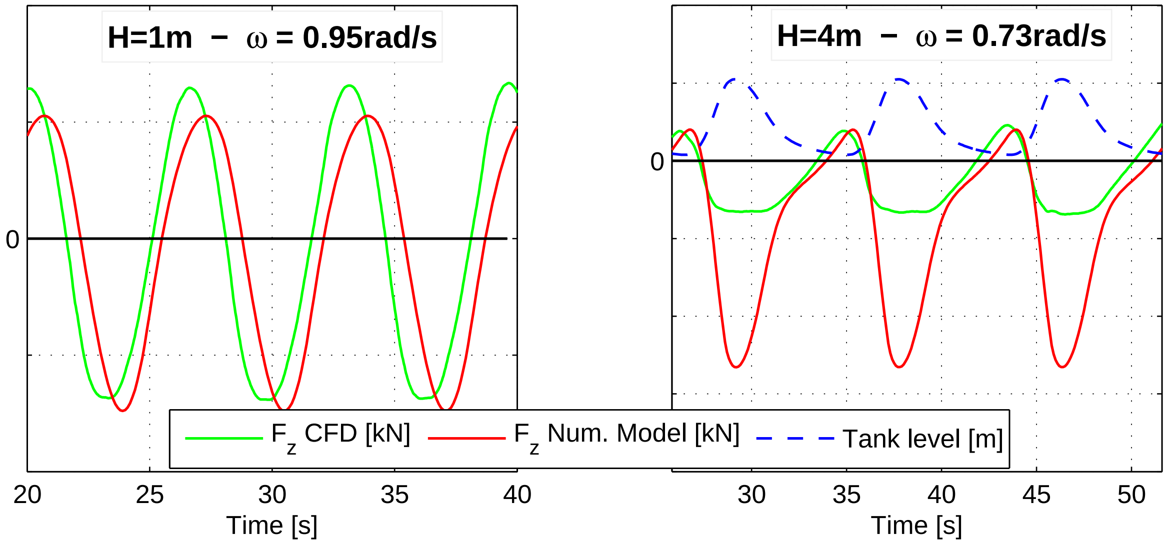

Figure 8-3: *Heave force RAOs and phase on the outer surface of the raised and double panel model.*

The cause of this phase shift may be found at the wave forces on the outer surface, see figure 8-1. Here, it can be seen that the wave force experiences a phase shift at this frequency. Furthermore, the surface elevation RAOs (figure 8-2) indicate that at approximately 0.75 rad/s the pumping mode is present. For higher periods large variations are observed in the boundary conditions. Both the phase shift in the wave force and the large variations in tank boundary conditions may be the cause of the phase shift in the force time trace. This is not further investigated.

The second recurring phenomenon applies to the double panel model as well. For wave heights of 2 m and 4 m, correct signal crests but incorrect signal troughs are observed in the time traces, see the right graph of figure 8-3. Here it can be seen that the troughs show large negative values, whereas the troughs acquired from CFD are truncated. For both wave heights, visualization of the CFD simulations show that a high velocity jet runs over the cylinder's top surface as soon as the wave breaks (see the snapshot of figure 2-4c in the problem description). This corresponds to the truncated trough in the force signal. Eventually the high velocity jet runs over the trailing edge of the cylinder and the amount of water on top reduces drastically (figure 2-4d), resulting in a sudden increase in upward force. The tank level in figure 8-3 on the other hand, shows a large pumping mode being present for 2 m and 4 m wave height at the double panel model. This pumping mode in not correct and results in the large negative troughs in the force time trace. Note that for 1 m wave height, CFD shows a pumping mode being present on top of the cylinder. In this case the numerical model show good correspondence.

8-1-2 Irregular waves

Subsequently, irregular wave simulations are performed on the submerged captive cylinder. According to the model tests, the JONSWAP spectrum is used with a peak enhancement factor γ of 3.3 and a peak period of 9 s. The significant wave height is varied between 1 m, 2 m and 4 m. The submergence is varied between 1 m, 3 m and 7 m. The simulation time equaled 3000 s or 50 min. The RAOs and phases for both surge and heave are acquired, however only the results for heave are discussed here. The surge force RAOs and phases are included in appendix E. The results using the (incorrect) fluctuating static pressure are included in this appendix as well.

8-1-3 Results

The heave force RAOs of the raised panel model are shown in figure 8-4a. For 1 m submergence, it is clearly visible that the numerical model underestimates the heave force RAOs for 1 m and 2 m wave height. The 4 m wave height RAO is at the same order of magnitude, but slightly to low. This was observed in the regular wave simulations as well. The wave height dependency is slightly present at 1 m submergence, whereas it vanishes at larger submergence. For 3 m submergence the numerical model is not able to reproduce the model test RAOs, whereas for 7 m submergence better correspondence is observed.

The accompanying heave phase angles are included in figure E-4b of appendix E. The numerical model predicts the correct phase for 4 m wave height at each submergence. The wave height dependency is not captured at the phase angles, such that the phases for 1 m and 2 m wave height are incorrect.

Figure 8-4b shows the heave force RAOs using the double panel model. Good correspondence is found at 1 m submergence and a wave height of 1 m. The peak at approximately 0.7 rad/s caused by the pumping mode is captured, but the simulated peak is slightly to narrow. The RAOs of 2 m and 4 m wave height show this peak as well, whereas it is not present in the model tests. This was also observed and discussed according to figure 8-3. At a submergence of 3 m and 7 m, both a correct order of magnitude as correct shape of the RAOs is observed. However, the wave height dependency is not present at 3 m submergence. Linear results are found at 7 m submergence, as expected

The heave phase angles (shown in figure E-6b) at 1 m submergence shows correct angles at 0.6 rad/s. However, at higher frequencies the phases show are too low compared to the phase angles of the model tests. The same observations can be made for larger submergences.

For surge it can be stated that the double panel model gives slightly better results compared to the raised panel model. Both the RAOs and phases are more in line with the model tests.

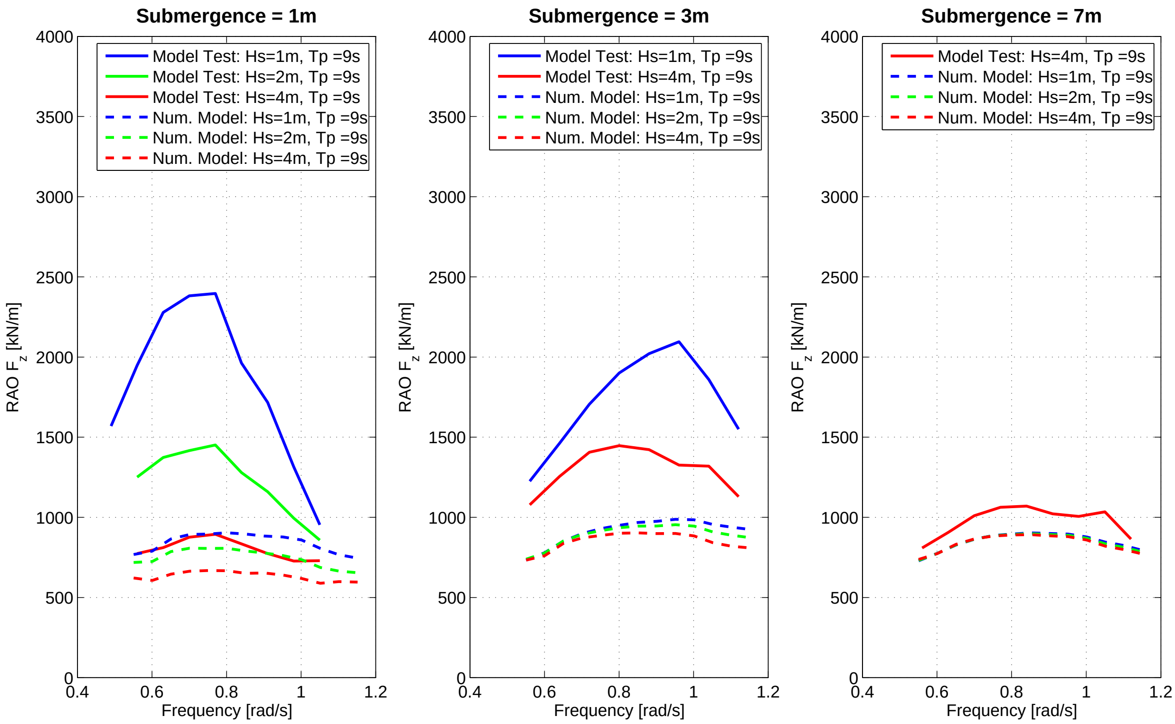

(a) *Raised panel model*

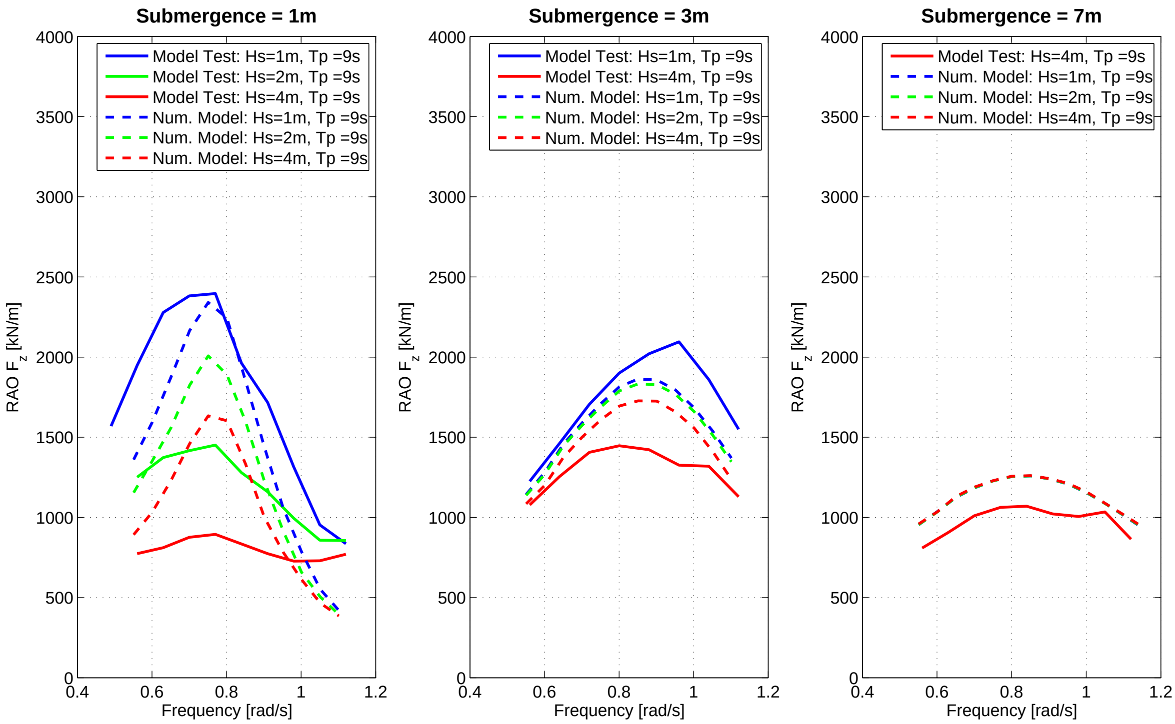

(b) *Double panel model*

Figure 8-4: *Heave force RAOs for both panel models at various submergences, taking into account a fixed static pressure.*

8-1-4 Discussion

As was stated in the discussion for regular waves, the visualization of the CFD simulations shows a pumping mode being present for 1 m wave height. For larger wave heights the waves break at the leading edge of the cylinder and a high velocity jet of water runs over the cylinder's top surface. Due to the momentum, the water runs over the trailing edge and the top surface runs dry quickly. This visualization indicates that two different phenomena are present in the force RAOs; for small waves the RAOs are dominated by the pumping mode, whereas for larger wave heights the RAOs are dominated by the emergence of the body.

The physical motivation of the double panel model is to take into account the pumping mode. The effect of this pumping mode is clearly visible in the tank boundary conditions. Since these boundary conditions are considered to be linear, the pumping mode is taken into account at each wave height. This results in correct results for 1 m wave height, since the pumping mode is present in reality. However, for larger wave heights the pumping mode vanishes in reality, whereas the double panel model still takes it into account.

If we introduce the dimensionless number $\kappa = S/H$, where S is the submergence and H is the wave height, we acquire the following values for κ:

Table 8-1: *1m submergence*

S[m]	H[m]	κ[-]
1	1	1.00
1	2	0.50
1	4	0.25

Table 8-2: *3m submergence*

S[m]	H[m]	κ[-]
3	1	3.00
3	4	0.75

Table 8-3: *7m submergence*

S[m]	H[m]	κ[-]
7	4	1.75

Based on κ, it might be stated that the force RAO of the cylinder is dominated by a pumping mode as soon as $\kappa \geq 1.0$. For these values, good correspondence with the double panel model is found

In case $\kappa < 1.0$ the incoming wave is large compared to the submergence. In this situation the cylinder runs dry, such that the RAO is dominated by the emergence of the body. This is not in line with the physical motivation of the double panel model, as a consequence the results show less correspondence with reality.

The raised panel model followed from the assumption that, in case of small submergences, waves are not able to enter the shallow water region on top of the body. This makes it valid to raise the sides up to the still water surface. The assumption can be interpreted as the cylinder running dry at all times; no pumping mode is present and waves are not able to enter the shallow water region at all.

Following the dimensionless number, this suggests the limiting case of κ approaching zero. In other words, a large wave height compared to the submergence. Following the decreasing trend in the force RAOs for increasing wave height, it might be stated that the raised panel model indeed calculates the RAOs as if large waves are present.

8-2 SSCV at Inconvenient Draft

Finally, the numerical model is applied to the freely-floating SSCV Thialf at inconvenient draft. Firstly, a radiation diffraction analysis is performed with the raised and double panel model of the vessel. Figures of the adjusted panel models are included in appendix F. Both analysis result in the wave forces and hydrodynamic coefficients for the outer surface and the surface elevation RAOs and dynamic pressure RAOs (i.e. the tank boundary conditions). The hydrodynamic coefficients and the surface elevation RAOs are discussed briefly in the upcoming two sections. Note that beam waves (starboard incoming) are used during the analysis and all six degrees of freedom are taken into account, whereas only heave and roll are shown here.

8-2-1 Tank boundary conditions

The surface elevations RAOs used to acquire the tank boundary conditions are shown in figure 8-6. Only four specific fiel points are depicted, according to figure 8-5 and table 8-4.

For the raised panel model a clear distinction can be made between the RAOs of the four field points. The first point is located at the leading side of the SSCV Thialf. At this point it can be observed that the RAO becomes 2 m/m for short waves, since the raised pontoon acts as a vertical wall. Point four is located at the trailing side of the SSCV Thialf. Here, the RAO approaches 0 m/m due to shielding effects. Points two and three are located between the pontoons. A significant peak is present at approximately 0.55 rad/s. Visualization of the free-surface between the pontoons shows the presence of a standing wave at this frequency. The time-domain simulations are performed using a peak period of 13 s, which corresponds to a frequency of approximately 0.5 rad/s. As a consequence, the surface elevation time traces which results from these RAOs, is significantly affected by this peak. At the higher frequencies some additional peaks are present in the RAOs. These peaks are less within the wave energy range.

The surface elevation RAOs of the double panel model are shown in the lower graph of figure 8-6. An unphysical peak of 8 m/m can be observed near 0.35 rad/s. Visualization of the free-surface at this frequency shows two standing waves, being 90° out of phase which each other. One standing wave is located at the port side pontoon and the other at the starboard pontoon, both between the two leftmost columns[1]. At 0.55 rad/s the same peak is observed as was observed for the raised panel model at this frequency. The remainder of the surface elevation RAOs is cluttered and full of peaks due to all kinds of standing waves between the columns and between the pontoons of the SSCV.

---

[1] The wave forces on the outer surface are included in appendix F. Here, the influence of these standing waves is clearly visible in the roll moment RAOs.

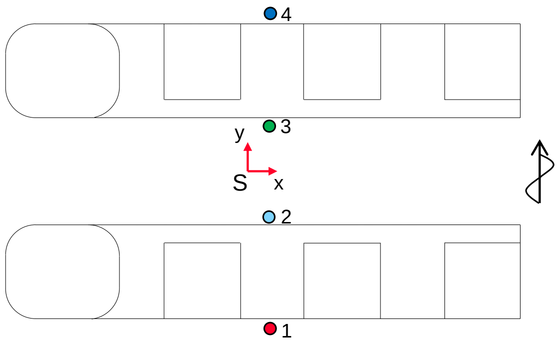

Figure 8-5: *Location of four field points, used for the surface elevation RAOs.*

#	x[m]	y[m]
4	1.08	45.2
3	1.08	15.2
2	1.08	-15.2
1	1.08	-45.2

Table 8-4: *Coordinates of the field points.*

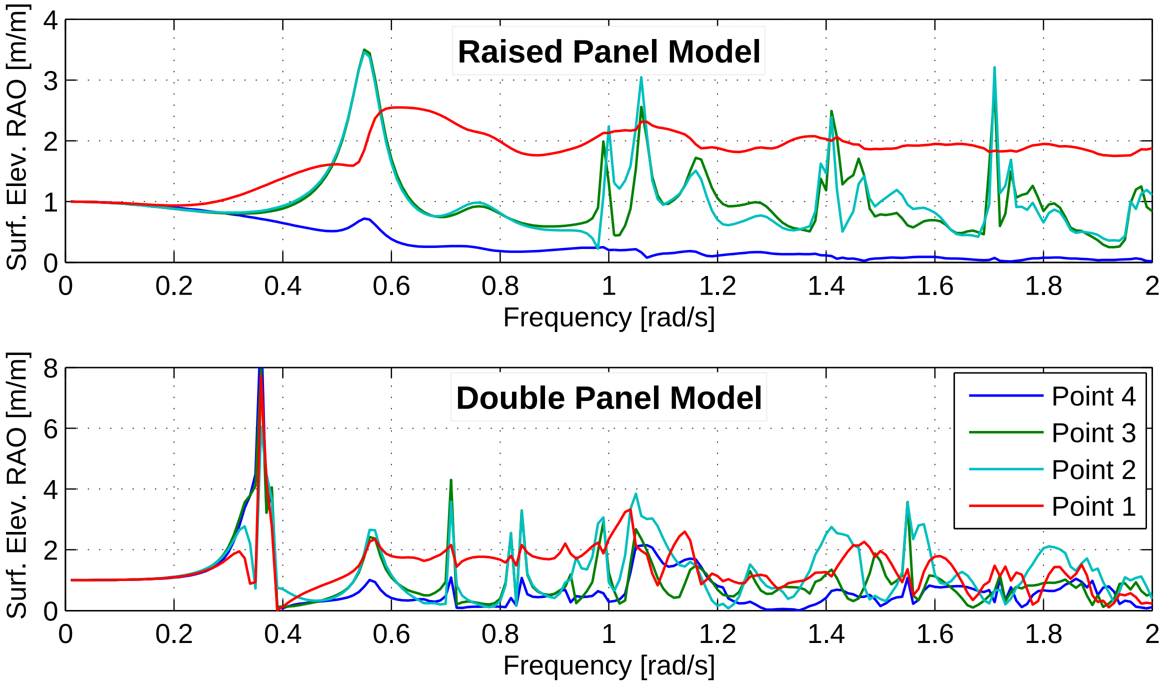

Figure 8-6: *Surface elevation RAOs for the SSCV Thialf at four field points, according to figure 8-5.*

8-2-2 Hydrodynamic coefficients

Figure 8-7 shows for both panel models the hydrodynamic coefficients for roll motions. The upper two graphs correspond to the raised panel model. It can be observed that the coefficients show large correspondence with the coefficients acquired in section 7-5-1 for the SSCV Thialf at transit draft, since basically the same geometry is used with the raised panel model. Smoothing is applied at the peaks at 1 rad/s as well.

The lower two graphs show the added mass and damping coefficients for the double panel model. Multiple sharp peaks are present due to standing waves between the columns. The peak near 0.35 rad/s results from the same standing waves as was observed in the tank boundary conditions. Unfortunately, the smoothing function is created to truncate peaks at one frequency only. Therefore, only the peak near 0.35 rad/s is truncated. The function could be extended to smooth the coefficients over the entire frequency range, however this tuning would go at the expense of the physical correctness. Therefore, it is decided not to do this. As a consequence, the retardation functions which follow from these coefficients do not converge to zero due to the remaining peaks.

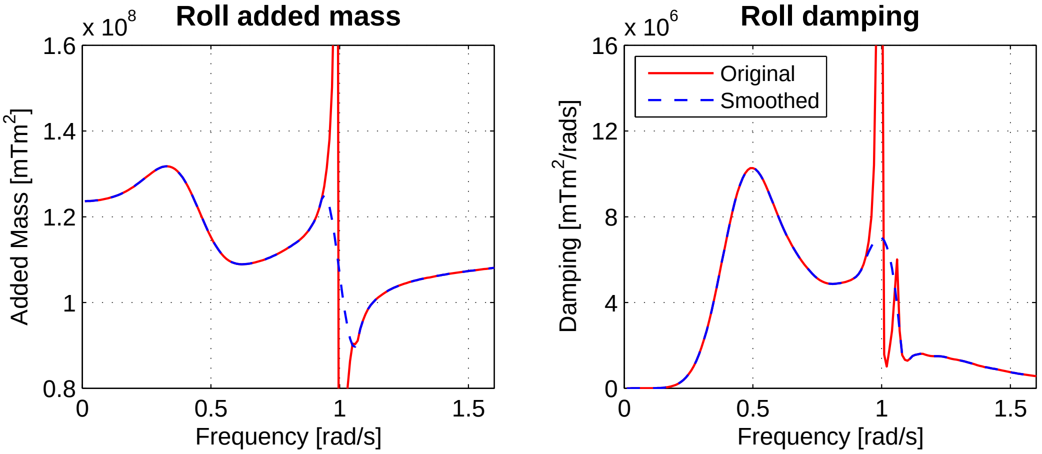

(a) *Raised panel model*

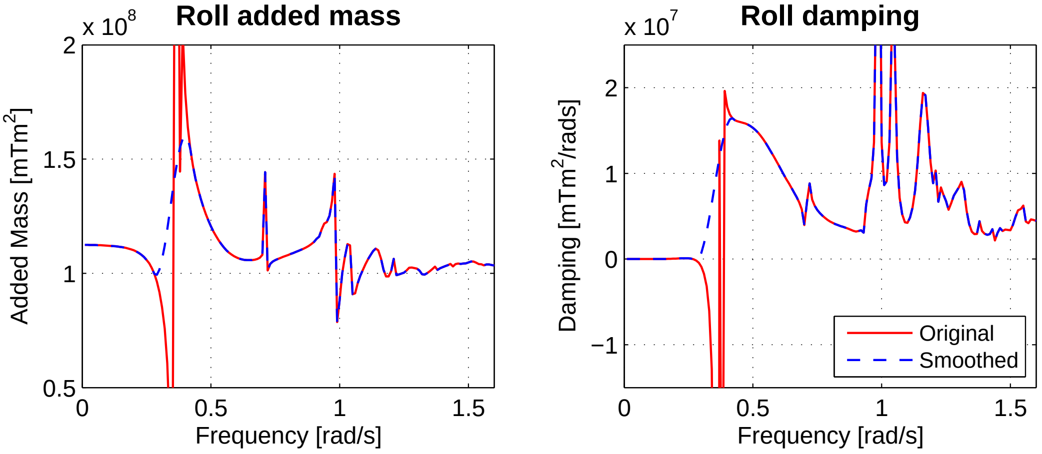

(b) *Double panel model*

Figure 8-7: *Added mass and damping coefficients at the outer surface of the SSCV Thialf.*

8-2-3 Results

The time-domain simulation using irregular waves is performed for both panel models. According to the model tests [28], the JONSWAP spectrum is used with a peak enhancement factor γ of 1.4 and a peak period of 13 s. The significant wave height is varied between 1 m, 2 m, 3 m and 4.3 m. The mass and load distribution and hydrostatic stiffness properties of the SSCV Thialf at 14.5 m draft are acquired from the model test reports as well. The simulation time equaled 3000 s or 50 min. The motion RAOs obtained by the numerical model and the model tests are shown in 8-8. In figure F-6 of appendix F the RAO obtained by the conventional radiation diffraction analysis using WAMIT is included.

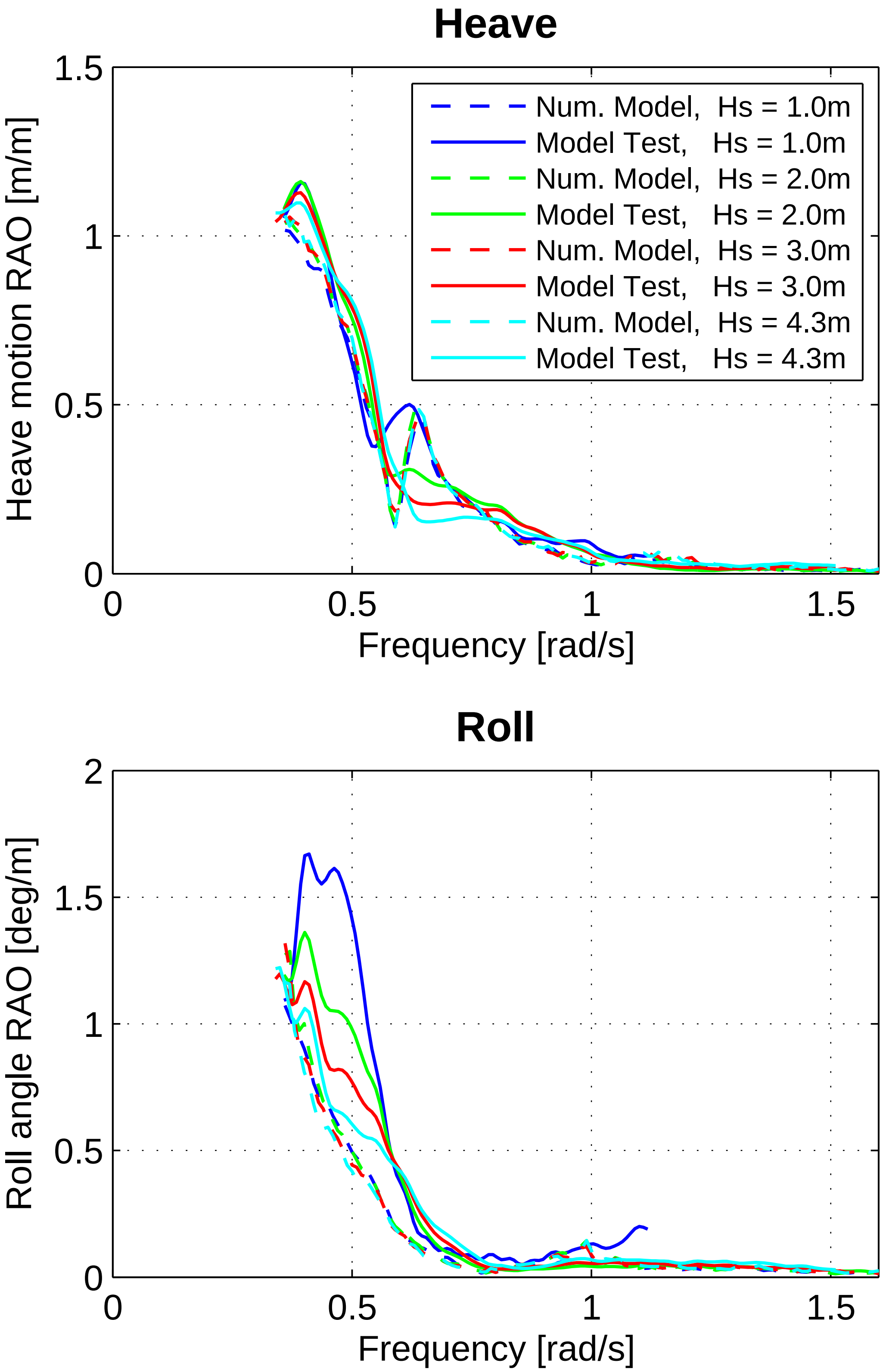

Figure 8-8: *Motion RAOs for heave and roll using the raised panel model.*

The upper graph of figure 8-8 shows the obtained heave motion RAO for various significant wave heights. In general it can be stated that the order of magnitude of the numerical model corresponds to the model test results. Furthermore, no incorrect peaks are present as were obtained by the conventional radiation diffraction analysis. At approximately 0.6 rad/s, the peak in the RAO for $H_s = 1m$ is captured. However, for increasing wave height the peak in the model test disappears. This is not observed in the numerical model; the numerical model does not show a wave height dependency in the motion response at all.

The roll RAOs are shown in the lower graph of figure 8-8. The conventional radiation diffraction calculations showed a clear peak near 0.45 rad/s. This peak is present to a lesser extend in the model tests for 1 m significant wave height. To numerical model however, does not show this peak. The RAOs are more in line with the model test RAOs of 4.3 m significant wave height. Similar as for heave, no wave height dependency is present in the roll RAOs.

8-2-4 Discussion

The numerical model using the raised version of the SSCV Thialf shows a linear motion response for both heave and roll. This is in line with the results of the raised cylinder.

As was stated in the problem description in section 2-2, the large peak in the roll RAO obtained by WAMIT follows from standing waves on top of the pontoons. In this case the RAO is dominated by the standing waves (i.e. a large κ-value). For larger wave heights, the pontoons emergence occasionally and no standing waves are able to occur. As a result the RAOs are dominated by the emergence of the pontoon (i.e. a low κ-value).

Similar as for the cylinder, by raising the panel model of the SSCV Thialf up to the water line, the presence of the standing waves is lost. This implies a low κ-value. This is confirmed by the calculated motion RAOs. The RAOs show the same trend as if large waves are present.

Unfortunately, the time-domain simulation using the double panel model of the SSCV Thialf is unstable. It is expected that this instability is caused by the peaks in the added mass and damping coefficients, which in turn results in non-converging retardation functions. The peaks in the hydrodynamic coefficients are caused by standing waves on top of the pontoons, while solving the radiation problem. In addition, high peaks are present in the diffraction forces on the outer surface and the tank boundary conditions. These peaks are caused by similar standing waves, while solving the diffraction problem.

Chapter 9

Conclusions and Recommendations

We main objective of this research is, as stated from chapter 1:

> *To develop a numerical model which is capable of calculating the motion behavior of a SSCV at a draft where the pontoons are 3 meter or less below the free surface.*

This objective is divided into to the following sub-objectives:

1. Perform a literature study to gain more insight in available methods and to select the most appropriate method for the numerical model;
2. Apply the numerical model to a captive body at inconvenient draft to acquire the excitation forces;
3. Extend the numerical model to simulate the motion behavior of a body at inconvenient draft.

For the numerical model, a free flooding tank approach is used to capture the non-linear behavior of a body at inconvenient draft. During a time-domain simulation, the water inside the tanks which exerts a static force on the top surface of the body, is calculated at each time step. The diffraction and radiation forces on the remaining wetted surface of the body are acquired using the results of a previously executed radiation diffraction analysis.

Two different panel models were found to be suitable for the radiation diffraction analysis. A raised geometry followed the assumption that, in case of small submergences, waves are not able to enter the shallow water region on top of the body. A double walled geometry followed from the physical motivation that the pumping model should be preserved, since both model tests and CFD simulations indicate that a pumping mode is present. Especially for smaller waves.

Application of the numerical model on a submerged captive cylinder is done to acquire the non-linear excitation forces on the body. Subsequently, the numerical model is applied to a freely-floating SSCV at inconvenient draft to acquire the non-linear motion response.

9-1 Conclusions

Cylinder

Firstly, the numerical model is applied to the submerged captive cylinder. It can be concluded that, using the raised panel geometry, the numerical model is not able to obtained the non-linear excitation forces. The resulting force RAOs are under predicted and the model does not fully capture the wave height dependency.

Secondly, the numerical model including the double walled geometry is applied to the submerged captive cylinder. Using this geometry, the obtained force RAOs are in correspondence with the model test RAOs, except for a submergence of 1 m and a wave height 2 m and 4 m. Visualization of the in-house CFD results indicate that the pumping mode is less present in these situations. Instead, the dominant factor in the RAOs for these wave heights is the emergence of the body. The cause of this discrepancy is assigned to the tank boundary conditions, acquired using the double walled geometry. These include the presence of the pumping mode. Since the boundary conditions are considered as linear, the effect of the pumping mode is taken into account for each wave height. For 1 m this is correct since the pumping mode is present in reality. However for 2 m and 4 m this is not. Therefore, it can be concluded that a wave height dependency in the tank boundary conditions is required to capture the full wave height dependency in the force RAOs.

SSCV Thialf

Subsequently, the numerical model is used to do a motion analysis of the SSCV Thialf at inconvenient draft. Using the raised geometry, linear results are found for both the heave and roll RAOs. The absence of the wave height dependency is in line with the results of the raised cylinder. Despite the absence of the non-linearities in the results, it can be concluded that the calculated RAOs are in much better correspondence with the model test RAOs, compared to the conventional RAOs using WAMIT directly.

Unfortunately, the time-domain simulation using the double walled geometry of the SSCV Thialf turned out to be unstable. The cause of the instability is already found in the preliminary radiation diffraction calculation. Large standing waves are present between the columns and pontoons for both radiation and diffraction. As a results, sharp peaks are present in the diffraction forces, added mass and damping coefficients and tank boundary conditions.

Thesis objective

Reflecting to the main objective of this thesis, it can be concluded that the numerical model does not entire fulfill the objective. The obtained RAOs do not show the wave height dependency for both heave and roll. Nevertheless, the numerical model shows a significant improvement in the results compared to the results using the conventional programs.

9-2 Recommendations

In order to improve the numerical model, the follow recommendations are made:

Model Tests

Model tests results on a captive submerged cylinder are used throughout this entire research. Although this data has been valuable, the cylindrical shape is complex from a fluid point of view. Water flows on and off the cylinder's top surface from all directions and waves tend to propagate around the cylinder, i.e. wave focusing. Furthermore, the model tests on the cylinder were done with irregular waves only, were regular waves are desirable for validation. Additionally, the radiation diffraction analysis is used to acquire the diffraction forces on the outer surface of the cylinder. This analysis shows different forces for the raised and double panel model; both the RAOs and phases vary. The influence of the bottom forcing seems to be significant on the total force. Because of these reasons, an additional model test is recommended.

The proposed tests will be applied on a submerged captive beam (figure 9-1). Only the forces in x and z-direction are measured and only one wave direction is considered, namely perpendicular to the beam. By taking the length of the beam (y-direction, out of the paper) significantly longer than the height and width, the problem can be considered as two dimensional. To gain more insight in the non-linearities involved the submergence, wave height and wave periods are varied. Furthermore both regular as irregular wave test are proposed, to gain more insight in the process of reproducing irregular wave results of a non linear problem with regular waves. Additionally, pressure sensors can be placed on at the surface of the beam to gain more insight in the forces on the outer surface

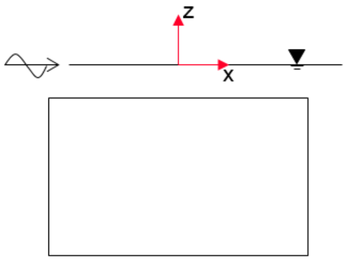

Figure 9-1: *Schematic side view of the beam*

The main objective of these model tests is to create and acquire accurate and sufficient validation material for the numerical model. In return, by making use of a simplified shape, the model tests give more insight in the problem on a more fundamental or academic level. The full proposal is attached in appendix B.

Tank Boundary Conditions

CFD visualizations indicates that the dominated factor in the force RAO changes with wave height. For small waves the pumping mode is present, whereas for larger waves the force RAO is dominated by the emergence of the cylinder. The physical motivation of the double walled geometry is to take into account the pumping mode. This turns out the be correct for small waves where the pumping mode is present in reality. For higher waves the boundary conditions still assume the presence of the pumping mode, whereas in reality it is less present. Gain more insight in the correct boundary conditions is therefore recommend. In order to do so, additional wave gauges can be placed on top of the beam during the previously proposed model tests.

Retardation Boundary Conditions

The tank boundary conditions are based on the incoming and diffracted waves only. As a result, the tank boundary conditions are taken into account as if the body is fixed at all times. It is recommended to take into the surface elevation and pressures due to radiation of waves as well. The radiation boundary conditions depend on the velocity and acceleration of the body. Therefore they need to be incorporated using retardation functions, similar as for the hydrodynamic added mass and damping. It is expected that this might decrease the sharp peaks which are obtained at the double panel model of the SSCV Thialf.

Damping lid

Standing waves are observed during the radiation diffraction analysis between the columns and pontoons. These standing wave occur for both radiated waves as for incoming and diffraction waves. It is expected that the effects on the retardation functions, wave forces and the tank boundary conditions makes the time-domain simulation for the double panel model of the SSCV Thialf unstable. It is encouraged to investigate the use of a damping lid between the columns. It suppresses the standing waves and therefore the peaks.

SSCV Thialf at 16.6m draft

The numerical model is not yet applied to the SSCV Thialf at 16.6m draft. This implies a submergence of 3 meter. It is known that the conventional radiation diffraction programs give incorrect motion RAOs at this submergence as well. The results of the double panel model of the cylinder at 3m submergence indicates that the numerical model is capable of giving improved results.

Appendices

Appendix A

Potential Theory

In order to describe most fluid flow phenomena associated with the waves and the motion of ships in waves, we need to know the velocity of the fluid and the pressure at different locations. The velocity of the fluid at the location $\vec{x} = [x, y, z]^T$ is given by the fluid flow velocity vector [23]:

$$\vec{v}\,(\vec{x}, t) = [v_1\,(\vec{x}, t)\,, v_2\,(\vec{x}, t)\,, v_3\,(\vec{x}, t)]^T \tag{A-1}$$

For the flow velocities involved in ship motion, the fluid can be considered incompressible, that is of constant density ρ. Under this assumption, the net volume rate at a volume V enclosed by a closed surface S is

$$\iint_S (\vec{v} \cdot \vec{n})\, dS = \iiint_V \operatorname{div}(\vec{v})\, dV = 0 \tag{A-2}$$

Since equation (A-2) should be valid for all regions V in the fluid, then by assuming that $\operatorname{div}(\vec{v})$ is continuous we obtain:

$$\operatorname{div}(\vec{v}) = \nabla \cdot \vec{v} = \frac{\partial v_1}{\partial x} + \frac{\partial v_2}{\partial y} + \frac{\partial v_3}{\partial z} = 0 \tag{A-3}$$

which is the continuity equation for incompressible flows. It is a linear equation in terms of the water particle velocities u, v and w and implies conservation of mass in the fluid. The conservation of momentum is described by the Navier-Stokes equations:

$$\rho \left(\frac{\partial \vec{v}}{\partial t} + \vec{v} \cdot \nabla \vec{v} \right) = \rho \vec{F} - \nabla p + \mu \nabla^2 \vec{v} \tag{A-4}$$

where $\vec{F} = [0, 0, -g]^T$ are accelerations due to volumetric forces, from which only gravity is considered, $p = p(\vec{x}, t)$ is the pressure in the fluid and μ is the viscosity coefficient of the fluid.

To describe the real flow of ships, it is then necessary to solve the Navier-Stokes equations (A-4) together with the continuity equation (A-3). These form a system of non-linear partial differential equations, which unfortunately do not have analytical solutions and the numerical solutions are still far from being feasible with current computational power.

If viscosity is neglected, the fluid is said to be an ideal fluid or inviscid. This is a common assumption that is made to calculate ship flows because viscousity ogten matters only in a thin layer close to the ship hull. By disregarding the viscosity term in (A-4), the Euler equations of fluid motions are obtained:

$$\rho\left(\frac{\partial\vec{v}}{\partial t}+\vec{v}\cdot\nabla\vec{v}\right)=\rho\vec{F}-\nabla p \tag{A-5}$$

A further simplification of the flow description is obtained by assuming that the flow is irrotational:

$$\operatorname{curl}\left(\vec{v}\right)=\nabla\times\vec{v}=0 \tag{A-6}$$

The term potential flow is used to describe irrotational flows of inviscid-incompressible fluids. Under these assumptions, mathematicians have found a scalar function $\Phi\left(t,\vec{x}\right)$ called the velocity potential. This is a function of which the spatial derivatives are equal to the velocities of the water particles:

$$\vec{v}=\nabla\Phi \tag{A-7}$$

Hence, if the potential Φ of the fluid is known, the fluid velocities can be calculated as:

$$v_1=\frac{\partial\Phi}{\partial x},\qquad v_2=\frac{\partial\Phi}{\partial y},\qquad v_3=\frac{\partial\Phi}{\partial z} \tag{A-8}$$

Using the velocity potential, the continuity equation (A-3) can be written in terms of the potential Φ by substituting the spatial derivatives, known as the Laplace Equation:

$$\nabla^2\Phi=\frac{\partial^2\Phi}{\partial x^2}+\frac{\partial^2\Phi}{\partial y^2}+\frac{\partial^2\Phi}{\partial z^2}=0 \tag{A-9}$$

Furthermore, the velocity terms in the Euler equations (A-5) can be written in terms of the velocity potential Φ. After some algebra this results in the Bernoulli equation:

$$\frac{\partial\Phi}{\partial t}+\frac{1}{2}\left(\nabla\Phi\right)^2+gz+\frac{p}{\rho}=C \tag{A-10}$$

A-1 Airy wave theory

Airy wave theory, or often referred to as linear wave theory, uses a velocity potential Φ to describe the motion of gravity waves on a fluid surface. In order to use this approach with waves, it is necessary to assume that the water surface slope or wave amplitude is very small (i.e. $ak \ll 2\pi$ and $a \ll d$) [29]. This means that terms in the equations of the waves with a magnitude in the order of the steepness-squared can be ignored. The profile of a simple, long-crested wave with a small steepness looks like a sine or cosine, therefore the two dimensional wave potential is written as [13]:

$$\Phi\left(x, z, t\right) = P(z) \cdot \sin\left(kx - \omega t\right) \tag{A-11}$$

in which $P(z)$ is an as yet unknown function, k is the wave number, ω the wave frequency and t represents time. In order to obtain the full expression for the velocity potential Φ of the harmonic waves, equation (A-11) is substituted in the Laplace Equation (A-9). Subsequently, the boundary value problem has to fulfill the following boundary conditions:

1. Sea Bed Boundary Condition. This implies that, at a water depth h, the vertical velocity of the water particles at the sea bed is zero:

$$\frac{\partial \Phi}{\partial z} = 0 \qquad \text{for} \qquad z = -h \tag{A-12}$$

2. Free Surface Dynamic Boundary Condition. This requirement states that the pressure p at the free surface of the fluid, $z = \zeta$, is equal to the atmospheric pressure p_0. By making use of the Bernoulli equation (A-10) and after linearization this yields:

$$\frac{\partial \Phi}{\partial t} + g\zeta = 0 \qquad \text{for} \qquad z = 0 \tag{A-13}$$

With these boundary conditions, the corresponding wave potential, depending on the water depth h, is given by:

$$\Phi\left(x, z, t\right) = \frac{\zeta_a g}{\omega} \frac{\cosh\left(k(h+z)\right)}{\cosh\left(kh\right)} \sin\left(kx - \omega t\right) \tag{A-14}$$

Additionally, the relation between the wave number k and the wave frequency ω follows from the Free Surface Kinematic Boundary Condition. This boundary condition states that the vertical velocity of a water particle at the free surface of the fluid is identical to the vertical velocity of the free surface itself (i.e. a particle at the free surface remains at the free surface):

$$\frac{\partial z}{\partial t} + \frac{1}{g}\frac{\partial^2 \Phi}{\partial t^2} = 0 \qquad \text{for} \qquad z = 0 \tag{A-15}$$

Substitution of the wave potential from equation (A-14) into the Free Surface Kinematic Boundary Condition gives the dispersion relation for an arbitrary water depth h. This expression gives the relationship between k and ω:

$$\omega^2 = kg \tanh(kh) \tag{A-16}$$

In order to obtain the pressure p in first order wave theory, the linearized version of the Bernoulli equation (A-10) is used:

$$\frac{\partial \Phi}{\partial t} + gz + \frac{p}{\rho} = 0 \qquad \rightarrow \qquad p = -\rho gz - \rho \frac{\partial \Phi}{\partial t} \tag{A-17}$$

Here the term including the quadratic velocities is neglected since it is of second order. The constant C is included in $\frac{\partial \Phi}{\partial t}$, this will not influence the velocities being obtained from the potential Φ. Substitution of the wave potential (A-14) gives the expression for the linearized pressure:

$$p\,(x, z, t) = -\rho gz + \rho g \zeta_a \frac{\cosh(k(h+z))}{\cosh(kh)} \cos(kx - \omega t) \tag{A-18}$$

A-2 Diffraction theory

According to linear potential theory, the potential of a floating body is a superposition of the potentials due to the undisturbed incoming wave Φ_0, the potential due to the diffraction of the undisturbed incoming wave on the fixed body Φ_7 and the radiation potentials due to the six body motions Φ_j:

$$\Phi = \Phi_0 + \Phi_7 + \sum_{j=1}^{6} \Phi_j \tag{A-19}$$

In regular waves with frequency ω the potential Φ, which is a function of the earth-fixed coordinates and time, can be written as a product of a space-dependent term and a harmonic time-dependent term:

$$\Phi(x, y, z; t) = \phi(x, y, z) \cdot e^{-i\omega t} \tag{A-20}$$

Here, the space-dependent part of the velocity potential ϕ_0 - associated with an undisturbed long-crested regular wave in deep water - is known and given by:

$$\phi_0(x, y, z) = \frac{g}{\omega^2} e^{kz} e^{ik(xcos\mu + ysin\mu)} \tag{A-21}$$

and the potentials ϕ_7 and ϕ_j can be evaluated by a continuous distribution of sources on the body surface S_0:

$$\phi_j(x, y, z) = \frac{1}{4\pi} \iint\limits_{S_0} \sigma_j(\hat{x}, \hat{y}, \hat{z}) \cdot G(x, y, z; \hat{x}, \hat{y}, \hat{z}) dS_0 \qquad \text{for } j = 1...7 \tag{A-22}$$

in which $\phi_j(x, y, z)$ is the space-dependent part of the potential function in a point (x, y, z), $\sigma_j(\hat{x}, \hat{y}, \hat{z})$ indicates the unknown complex source strength in a point $(\hat{x}, \hat{y}, \hat{z})$ and $G(x, y, z; \hat{x}, \hat{y}, \hat{z})$ is the Green's function, which gives the influence of the source σ_j at $(\hat{x}, \hat{y}, \hat{z})$ on the potential ϕ_j at (x, y, z). To determine the potential ϕ_j we need to know the source strength σ_j. To get this we need the make sure that the potential satisfies the boundary condition at the hull surface, for the radiation and diffraction potentials this is given by:

$$\frac{\partial \phi_j}{\partial n} = f_j \qquad \text{for } j = 1...7 \tag{A-23}$$

$$\begin{aligned} \text{where: } f_1 &= \cos(n, x) & f_4 &= (r \times n)_1 & f_7 &= -\frac{\partial \phi_0}{\partial n} \\ f_2 &= \cos(n, y) & f_5 &= (r \times n)_2 & & \\ f_3 &= \cos(n, z) & f_6 &= (r \times n)_3 & & \end{aligned}$$

Implementing equation (A-22) into equation (A-23) and discretization of the integral results in:

$$-\frac{1}{2}\sigma_{mj} + \frac{1}{4\pi}\sum_{n=1}^{N} \sigma_{nj} \frac{\partial G_{mn}}{\partial n} \Delta S_n = f_{mj} \qquad \text{for } m = 1 \ldots N, \quad n \neq m \tag{A-24}$$

here m is the panel at which the potential is evaluated and n are the surrounding panels. The latter N equations can be put in the following matrix form:

$$\begin{pmatrix} A_{11} & \cdots & A_{1N} \\ \vdots & \ddots & \vdots \\ A_{N1} & \cdots & A_{NN} \end{pmatrix} \begin{pmatrix} \sigma_{1j} \\ \vdots \\ \sigma_{Nj} \end{pmatrix} = \begin{pmatrix} f_{1j} \\ \vdots \\ f_{Nj} \end{pmatrix} \tag{A-25}$$

where: $A_{nn} = -\frac{1}{2}$
$A_{mn} = \frac{1}{4\pi} \frac{\partial G_{mn}}{\partial n} \Delta S_n$

This system of equations can be solved by, for instance, LU decomposition. It results in the unknown source strengths which can be used to determine the added mass, damping and wave forcing. Once these are known the equations of motion for the vessel can be solved:

$$\sum_{j=1}^{6} \left(-\omega^2 \left(M_{kj} + a_{kj} \right) - i\omega b_{kj} + c_{kj} \right) \zeta_j = F_k \qquad \text{for } k = 1...6 \tag{A-26}$$

A-3 Multi-Domain Diffraction

One of the problems encountered with standard radiation diffraction theory is the fact that the total potential domain contains both the normal water depth and the shallow water depth on top of the pontoon. This results in an inaccurate evaluation of the incoming wave in the shallow water region. Therefore, this method -based on a multi-domain approach in 3D diffraction calculations- considers the additional domain as a second potential domain [4]. By dividing the total domain into two sub domains, the potentials will be determined separately, each with their own water depth. A coupling between the potentials has to be made on the interface surface between the domains.

A-3-1 Theory

In the multi-domain approach the total fluid domain will be split up in the primary domain and the additional domain, shown as respectively domain I and domain II in figure A-1. The potential functions within each domain will be evaluated with the corresponding water depth of that domain. The surface of the body belonging to domain I or II is denoted with S_I or S_{II} respectively. The two domains are coupled to each other by the interface D. This interface is modeled by panels at both sides of the interface. Panels at the side of domain I are denoted by L, panels at the side of domain II by R. In order to make a proper connection between the two potentials of each domain, a set of interface conditions has to be set up at D. The flow between the two domains has to be continues with respect to the momentum, therefore the pressure and velocity at R should be equal to L.

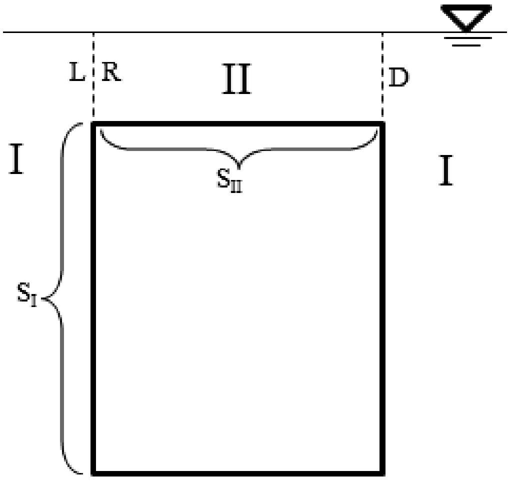

Figure A-1: *Domain boundary*

Potentials

The complex potential for the primary domain ϕ^I follows from the superposition of the undisturbed wave potential ϕ_0, the diffraction potential ϕ_7^I and the radiation potentials

ϕ_j^I associated with the j-modes of motion of the body ($j = 1...6$). The complex potential for the additional domain ϕ^{II} only contains the latter two, since there is no incoming wave. By making use of equations (A-19), (A-20) and (A-22) for $j = 1...7$, this results in the following potentials for both domains:

$$\phi^I = \phi_0 + \frac{1}{4\pi}\iint\limits_{S_I+D} \sigma_j^I G\,dS \tag{A-27a}$$

$$\phi^{II} = \frac{1}{4\pi}\iint\limits_{S_{II}+D} \sigma_j^{II} G\,dS \tag{A-27b}$$

To make sure the pressure at both sides of the interface is the same, we use the following condition:

$$\phi^I = \phi^{II} \tag{A-28}$$

After inserting the expressions for ϕ^I and ϕ^{II} into the interface condition for pressure and rearranging the terms leads to:

$$\phi_0 = \frac{1}{4\pi}\iint\limits_{S_{II}} \sigma_j^{II} G\,dS + \frac{1}{4\pi}\iint\limits_{D} \sigma_j^{II} G\,dS - \frac{1}{4\pi}\iint\limits_{S_I} \sigma_j^{I} G\,dS - \frac{1}{4\pi}\iint\limits_{D} \sigma_j^{I} G\,dS \tag{A-29}$$

Next to the pressures, we need to make sure the velocity normal to the surface of D is continuous. This is done by stating:

$$\frac{\partial \phi^I}{\partial n} = -\frac{\partial \phi^{II}}{\partial n} \tag{A-30}$$

Here, the minus sign is a results of the opposite normal vectors at D for both domains. Substituting both equations of (A-27) results in:

$$\frac{\partial \phi_0}{\partial n} = \frac{1}{2}\sigma_j^I + \frac{1}{2}\sigma_j^{II} - \frac{1}{4\pi}\iint\limits_{S_I+D} \sigma_j^I \frac{\partial G}{\partial n}\,dS - \frac{1}{4\pi}\iint\limits_{S_I+D} \sigma_j^{II} \frac{\partial G}{\partial n}\,dS \tag{A-31}$$

The two equations of (A-27) and equations (A-29) and (A-31) can be discretized to construct the following matrix, similar to (A-25):

$$\left(\begin{array}{c|c|c|c} \ddots & & & \\ I & D & 0 & 0 \\ \quad\ddots & & & \\ \hline D & & D & \\ \hline & & \ddots & \\ 0 & 0 & II & D \\ & & \quad\ddots & \\ \hline D & \ddots & D & \ddots \end{array}\right)\left(\begin{array}{c} \sigma_{1j} \\ \vdots \\ \vdots \\ \hline \sigma_{Nj} \\ \hline \sigma_{1j} \\ \vdots \\ \vdots \\ \hline \sigma_{Nj} \end{array}\right) = \left(\begin{array}{c} \phi_{1j} \\ \vdots \\ \vdots \\ \hline \phi_{Nj} \\ \hline \phi_{1j} \\ \vdots \\ \vdots \\ \hline \phi_{Nj} \end{array}\right) \tag{A-32}$$

This system of equations can be solved. It results in the unknown source strengths which can be used to determine the added mass, damping and wave forcing. Once these are known the equations of motion for the vessel can be solved.

A-3-2 Multi-Domain Diffraction on a captive submerged cylinder

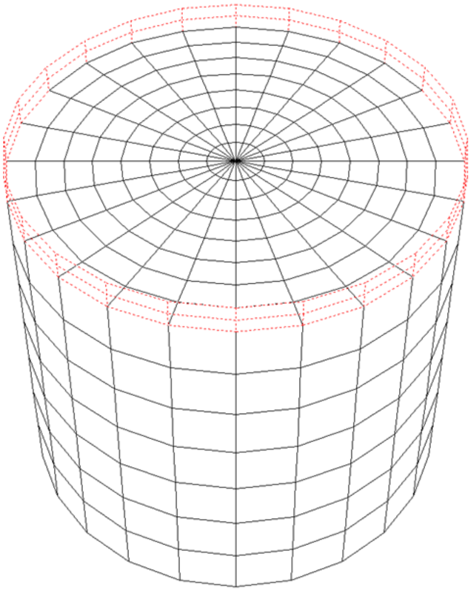

Figure A-2: *Panel model including interface used for the multi-domain approach*

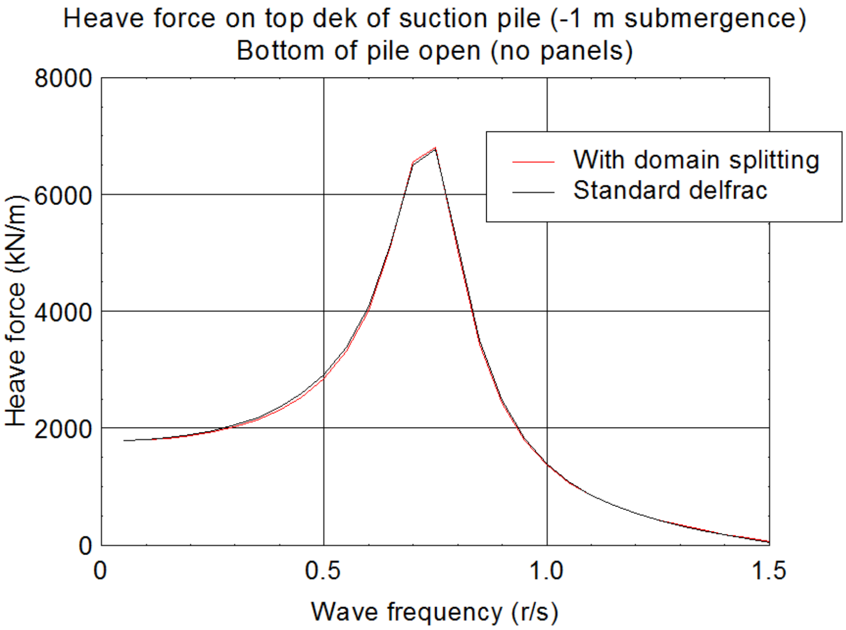

Figure A-3: *Results of conventional and multi-domain approach by Pinkster [4].*

Appendix B

Model Test Proposal

To validate the numerical model for a submerged captive body, the only data available within HMC is model test data on a cylindrical shape. Although this data is valuable for the numerical model of this thesis, the cylindrical shape is not the most optimal shape. Wave focusing will occur and a two dimensional analysis is not possible. Therefore a model test proposal is made during this thesis for a submerged captive beam

Objective

The main objective of these model tests is to create and acquire accurate and sufficient validation material for the numerical model. In return, by making use of a simplified shape, the model tests give more insight in the problem on a more fundamental or academic level and provides the university with scientific data related to submerged bodies in close proximity to the free surface. In addition to that, it allows the student to gain experience in model testing.

Model test setup

The tests will be applied on a submerged captive beam. Only the forces in x and z-direction are measured. To gain more insight in the non-linearities involved the submergence, wave height and wave periods are varied. Only one wave direction is considered, namely perpendicular to the beam. The test schedule is further considered in section B. The test will be performed on a scale of approximately 1:64. Two wave probes are placed in the towing tank, both at centre line of the tank. One between the wave maker and submerged beam model to measure the reference wave, the other on top of the submerged beam to measure the local water elevation, see figure B-1 and figure B-2. In figure B-2 the wave probe for the reference wave is depicted more to the right for clarity. If budget permits, an additional wave probe could be placed on top of the beam for better insight in the local wave elevation.

The submerged beam model has a length of 75cm, a width of 43.75cm and a height of 21.25cm. Width and height are based on the SSCV Thialf pontoon dimensions. The model is placed between two endplates, such that the problem can be considered as

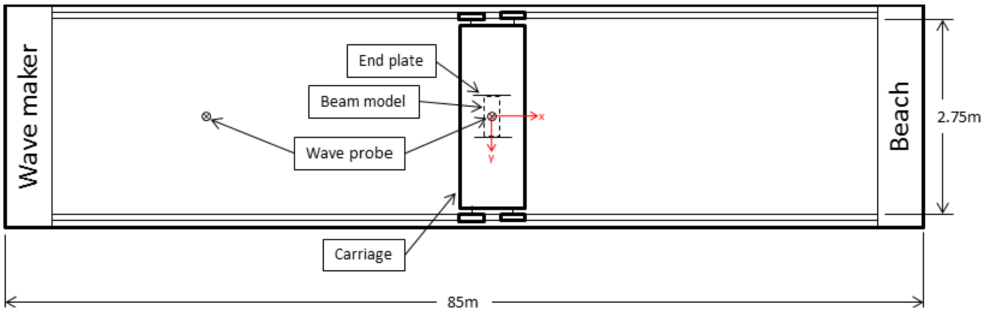

Figure B-1: *General overview model set up (top view)*

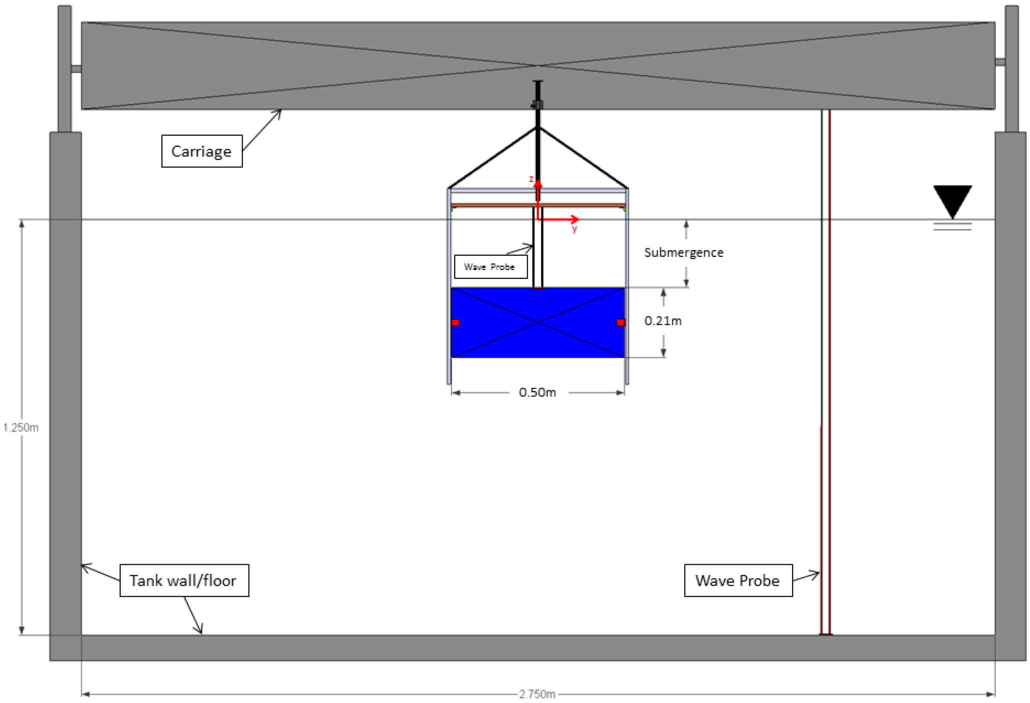

Figure B-2: *General overview model setup (front view)* two dimensional. The beam is suspended between the two endplates by the load cells or force transducers. The load cells are placed in a recess at the beam, such that the sides of the beam model and load cell are nearly in line with each other. This results in the clearance between beam model and endplates to be minimal, see figure B-3.

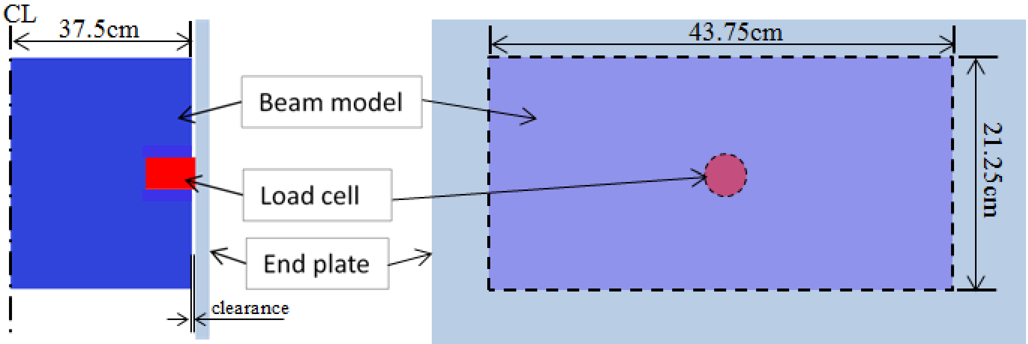

Figure B-3: *Load cell and end plate connection (left: front view/right: side view, not to scale)*

The endplates are connected to a frame which is suspended under the carriage of the towing tank. This frame is adjustable in height to vary the submergence depth. A cross bar is placed between the two endplates such that the wave probe can be connected to the cross bar and beam model. The connection plate of the probe at the beam should also be in a recess, resulting in the top surface of the beam model to be completely flat, see figure B-4.

Two adjustable frames are used, at both corners of the endplates. This ensures any pitch moment to be counteracted. The bars should be lowered exactly the same distance to prevent any inclination of the beam model. This can be achieved by adding depth marks on each frame.

Test Schedule

An overview of the test cases is shown on page 102. All wave height and wave period combinations (for regular and irregular) require calibration prior to setting up the model. Furthermore, model tests including 1m freeboard (transit draft) and a wave height of 1m need to be done to validate the results with conventional diffraction programs. Tests including 1m freeboard and 2m/4m wave height are done, since they are expected to give interesting results. The -7m and -13m freeboard tests are done to validate the results of diffraction programs at operational draft. A negative freeboard implies submergence of the beam.

It is assumed that model test basin will be operated 5 days a week, 8 hours a day (single shift, no overtime). Setting up the model and cleaning up afterwards is estimated to take approximately 2 days. It is expected that each wave test will take approximately 30 minutes (including start-up, transient, actual test and waiting for calm water). Thus the 114 cases will take a little bit more than 7 days to execute, resulting in 9 days total. Assuming two weeks test time, this leaves 1 day for extra test runs.

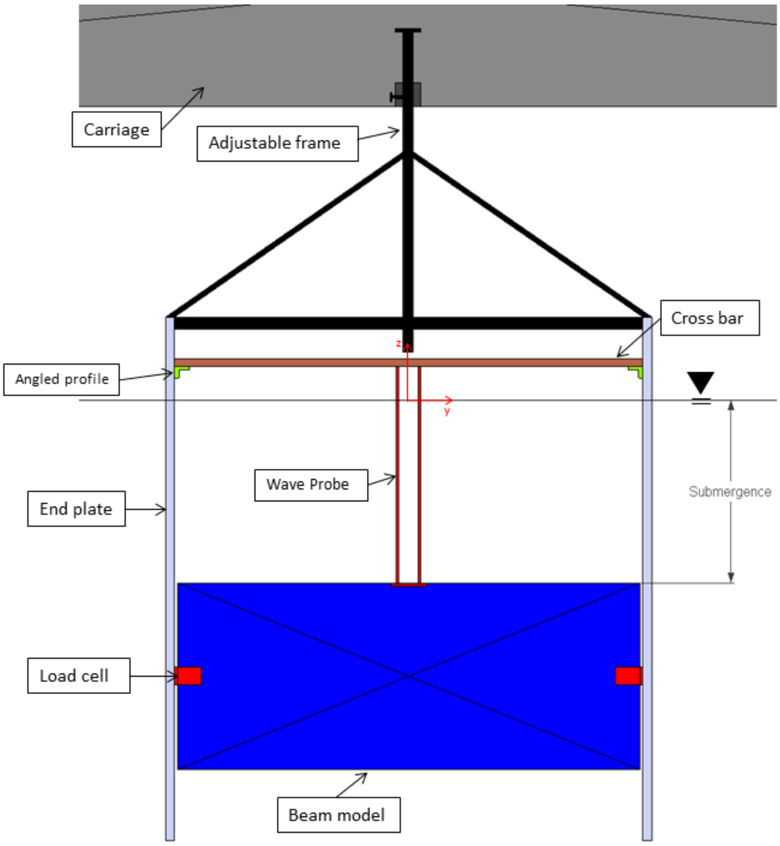

Figure B-4: *Detailed view model setup (front view)*

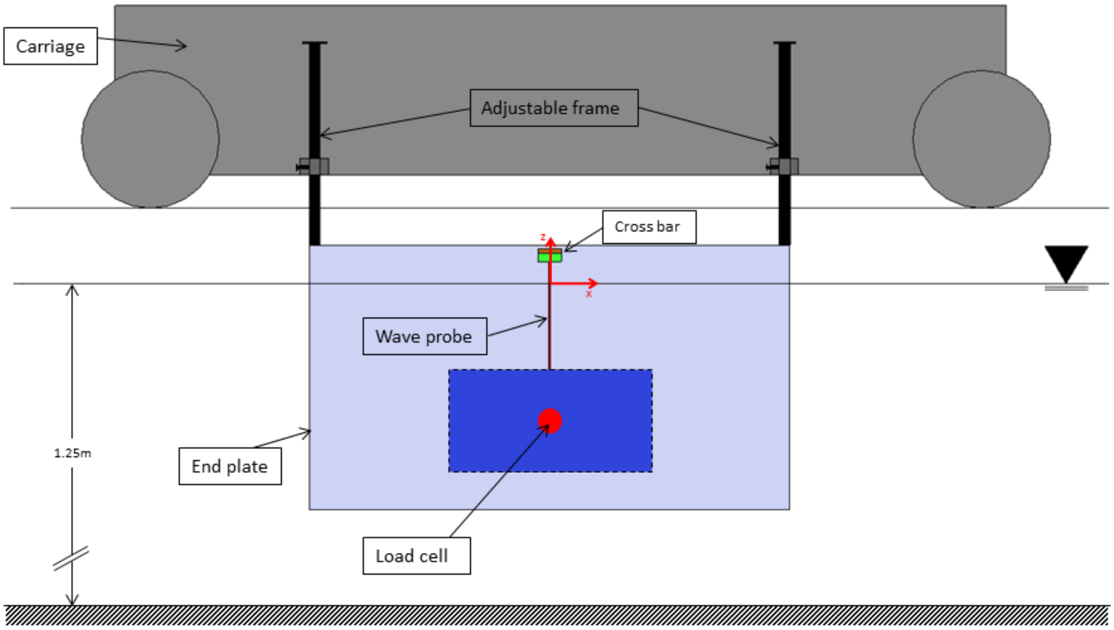

Figure B-5: *General overview of the model setup (side view)*

The following measurements are required:

- Calibration of wave probes
- Calibration of force transducers (including static load check on instrumented beam in the basin)
- Wave calibration prior to setting up the model.
- Wave height measurement during tests.
- Surge and heave force measurements during tests.

Table B-1: *Test case overview (FB = freeboard)*

Regular wave tests

Wave calibration			
H[m] T[s]	10	13	16
1	x	x	x
2	x	x	x
4	x	x	x

Draft: 12.6m (1m FB)			
H[m] T[s]	10	13	16
1	x	x	x
2	x	x	x
4	x	x	x

Draft: 14.6m (-1m FB)			
H[m] T[s]	10	13	16
1	x	x	x
2	x	x	x
4	x	x	x

Draft: 15.6m (-2m FB)			
H[m] T[s]	10	13	16
1	x	x	x
2	x	x	x
4	x	x	x

Draft: 16.6m (-3m FB)			
H[m] T[s]	10	13	16
1	x	x	x
2	x	x	x
4	x	x	x

Draft: 20.6m (-7m FB)			
H[m] T[s]	10	13	16
1			
2	x	x	x
4	x	x	x

Draft: 26.6m (-13m FB)			
H[m] T[s]	10	13	16
1			
2	x	x	x
4	x	x	x

Irregular wave tests

Wave calibation			
H[m] T[s]	10	13	16
1	x	x	x
2	x	x	x
4	x	x	x

Draft: 12.6m (1m FB)			
H[m] T[s]	10	13	16
1	x	x	x
2	x	x	x
4	x	x	x

Draft: 14.6m (-1m FB)			
H[m] T[s]	10	13	16
1	x	x	x
2	x	x	x
4	x	x	x

Draft: 15.6m (-2m FB)			
H[m] T[s]	10	13	16
1	x	x	x
2	x	x	x
4	x	x	x

Draft: 16.6m (-3m FB)			
H[m] T[s]	10	13	16
1	x	x	x
2	x	x	x
4	x	x	x

Draft: 20.6m (-7m FB)			
H[m] T[s]	10	13	16
1			
2	x	x	x
4	x	x	x

Draft: 26.6m (-13m FB)			
H[m] T[s]	10	13	16
1			
2	x	x	x
4	x	x	x

Appendix C

Regular Wave Time Traces Cylinder

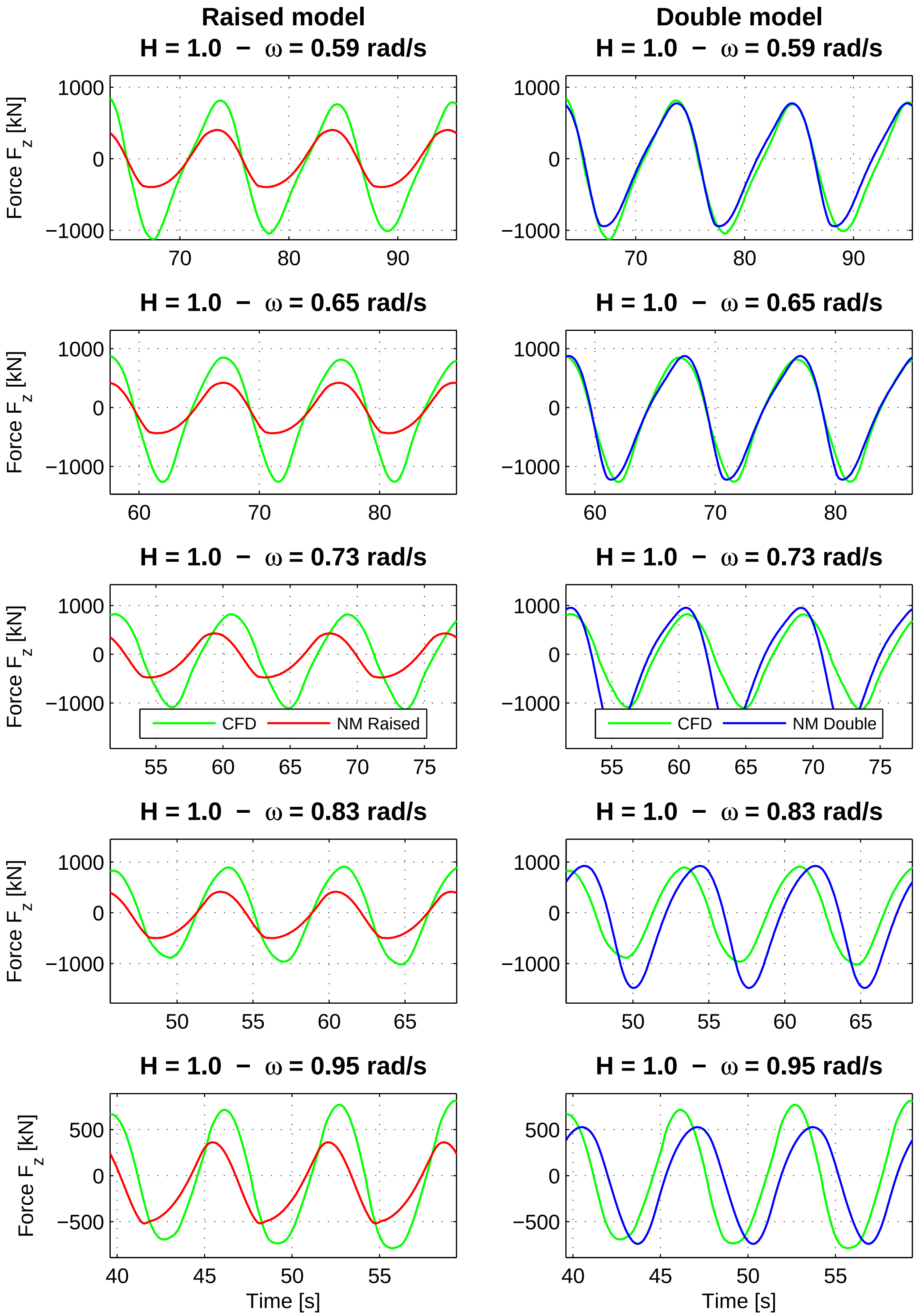

Figure C-1: *Heave force time trace using regular waves of 1m height.*

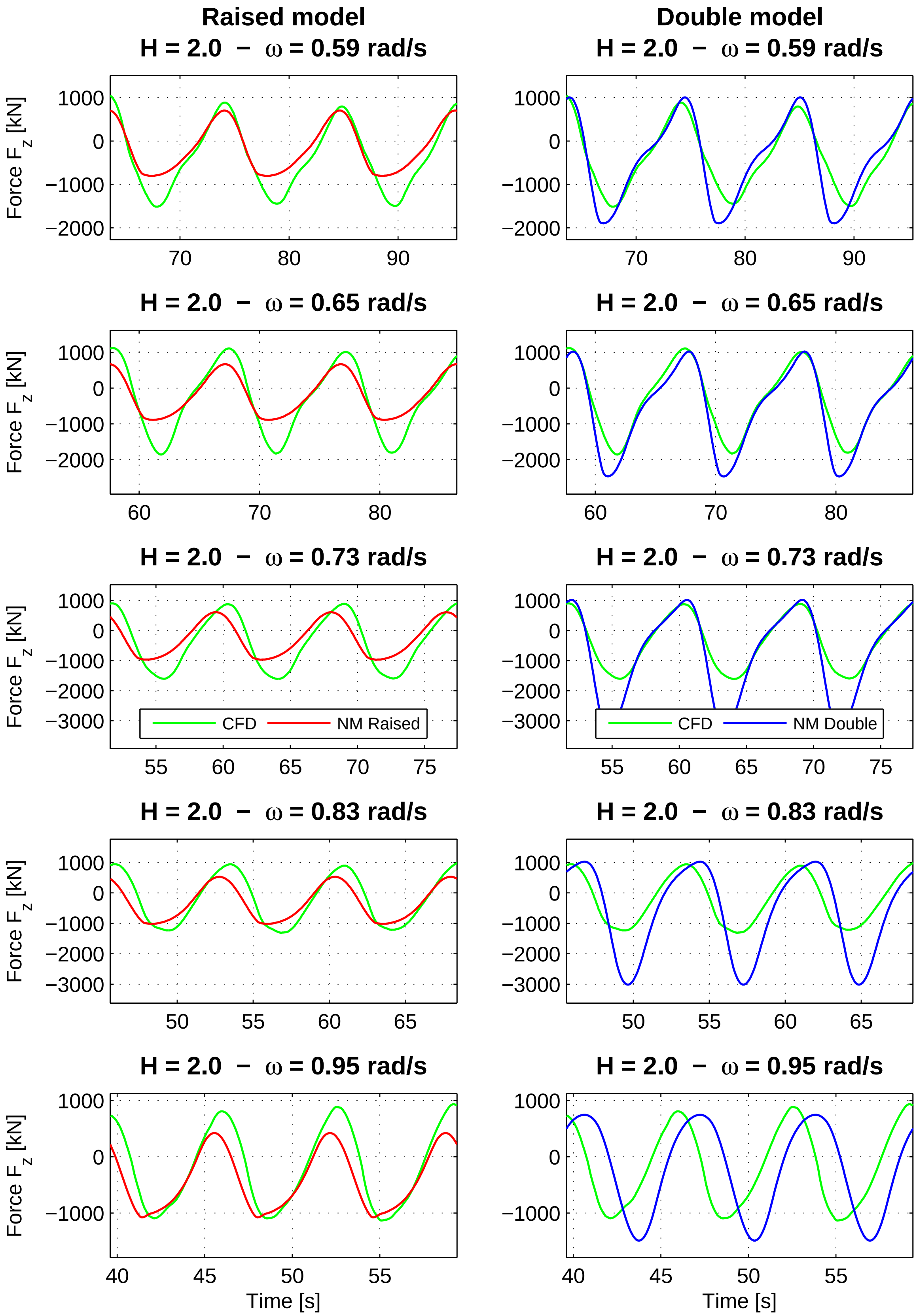

Figure C-2: *Heave force time trace using regular waves of 2m height.*

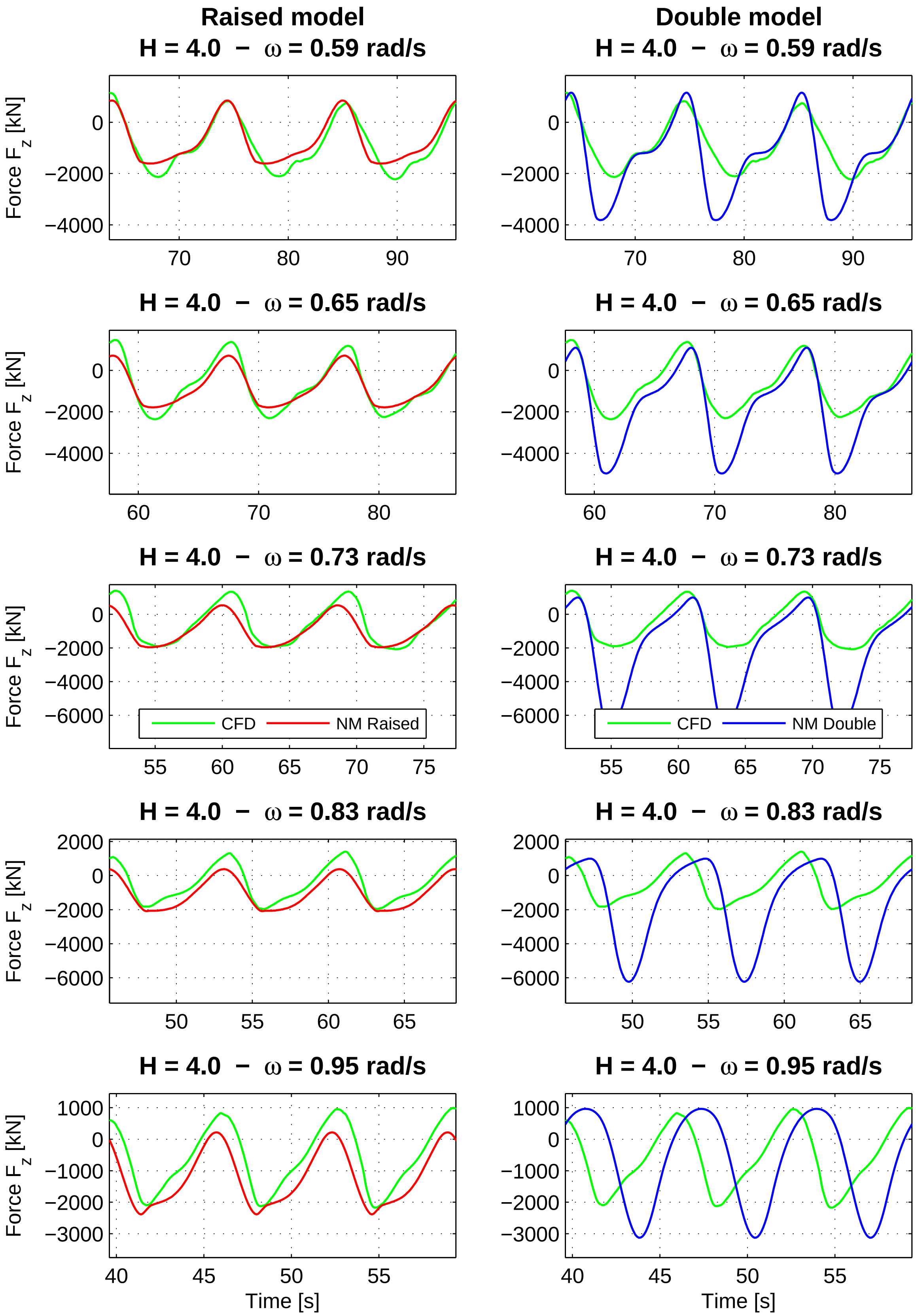

Figure C-3: *Heave force time trace using regular waves of 4m height.*

Appendix D

Flow Coefficient Tuning

During this research a flow coefficient of 0.6 has been used, which followed from relevant literature. An additional analysis if performed on this coefficient. Aim of the analysis is to verify the value of 0.6 and to gain more insight in the flow coefficient and how it affects the results. The analysis is performed on each of the four models of the submerged cylinder; the raised panel model with both the fluctuating and static pressure incorporation, and the double panel model including both pressure incorporations.

In the analysis the flow coefficient is split into two components, one applicable to inflow and the other for outflow. For each simulations the flow coefficients are tuned, such that the heave force time trace has the most optimal fit to CFD results. The resulting time traces are included at the end of this appendix.

The tuned coefficients are visualized in the graphs of figure D-1 on the next page. Here the first column of graphs indicate the tuned inflow coefficients and the second column indicates the tuned outflow coefficient. Furthermore each of the four rows corresponds with one of the four numerical model variations (see sub captions). Each individual graph shows the coefficient values for 1 m, 2 m or 4 m wave height against the dimensionless kD value (wave number times length unit). Gray colored lines indicate that no resembling fit was found with the CFD results.

At the upper two graphs of figure D-1, the position of the cylinder and SSCV Thialf are indicted on the dimensionless axis. For the cylinder the length unit equals the diameter $D = 15m$. The wave number corresponds to the frequency related to the peak in heave force RAO $k = \omega^2/g$ where $\omega = 0.73 rad/s$. For the SSCV Thialf the width of the pontoon is used $D = 28m$ and the peak period of the wave spectrum $T = 13s$ or $\omega = 0.48 rad/s$.

D-1 Tuning observations

In case the gray lines are left aside, the following four observations can be made:

(1) $\mathbf{C_f^{in}}$ is independent on the wave height: focusing on the left column of graphs, it can be seen that for each graph the three colored lines overlap each other. Increasing the wave height does not affect the inflow coefficient.

(2) $\mathbf{C_f^{in}}$ approach 0.5 for decreasing kD number: following the same lines, it can be observed that the inflow coefficients approach 0.5 $\sim$ 0.6 for decreasing kD number. This value is in line with the values stated in literature.

(3) $\mathbf{C_f^{out}}$ increases with wave height: focusing on the right column, it can be seen that the outflow coefficients increase for increasing wave height. This is most clearly shown in the upper left graph. This is explained by considering the emergence of the cylinder. For small wave heights, the top surface remains submerged during the entire wave cycle. There is no significant water outflow, thus the outflow coefficient can remain relative low. Visualization of the CFD results (as shown in the snapshots of figure 2-4 at page 11) showed that for higher waves the top of the cylinder runs dry in a wave trough. If the surface elevation in front increases again due to the incoming wave crest, the wave breaks and a high velocity jet runs over the cylinder. It continues over the top surface and eventually drops of the rear end of the cylinder. To capture this abrupt change in water mass, a high outflow coefficient is required.

(4) $\mathbf{C_f^{out}}$ converges to 0.6 for decreasing kD number: for the inflow coefficient a minor convergence to 0.6 was observed. For the outflow coefficient it is clearly visible. Based on the explanation of the previous observation, it can be added that for high frequency, the waves are steep and tend to break. This breaking wave results in the high velocity jet. At low frequencies the waves become less steep and instead of breaking, the water enters the top surface more gradually. This latter effect is more in line with the flow regimes of the literature which stated a flow coefficient of 0.6 (see section 6-4-1).

D-2 Conclusions

For low kD values (low frequency waves) the analysis confirmed a value of approximately 0.6 for both flow directions. For high frequency waves more discrepancy was found. Focusing on the upper right graph, the inflow coefficient converges to approximately 0.4, whereas for outflow a dependency on the wave height is found. Small wave heights result in an outflow coefficient of 0.4 and large wave heights require a coefficient of 1.0. However, these high kD values are outside the range of the cylinder and SSCV Thiaf. Following these kD values, an inflow coefficient of 0.4 $\sim$ 0.5 and an outflow coefficient of 0.5 $\sim$ 0.7 are applicable. Therefore, for both regular as irregular wave simulations, a flow coefficient of 0.6 is maintained for both inflow and outflow.

D-3 Overview

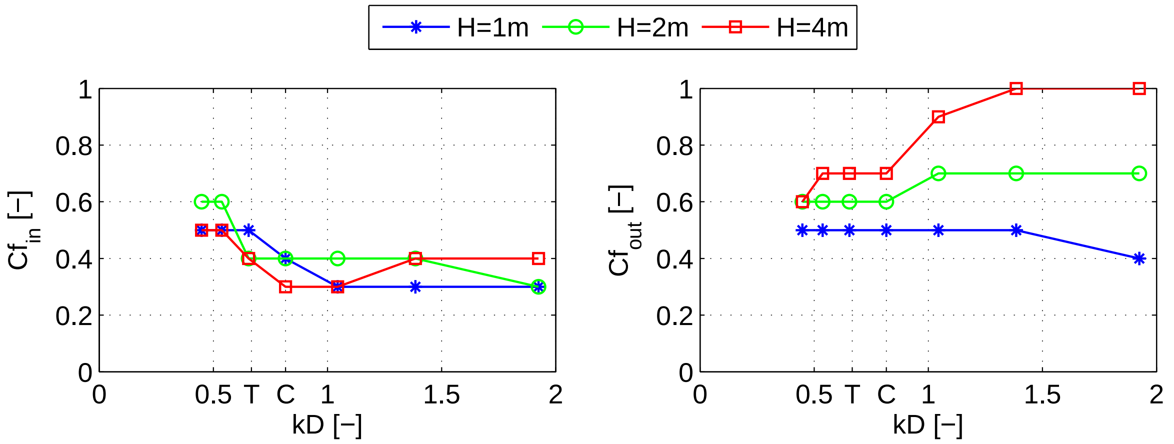

(a) *Raised panel model, fluctuating static pressure*

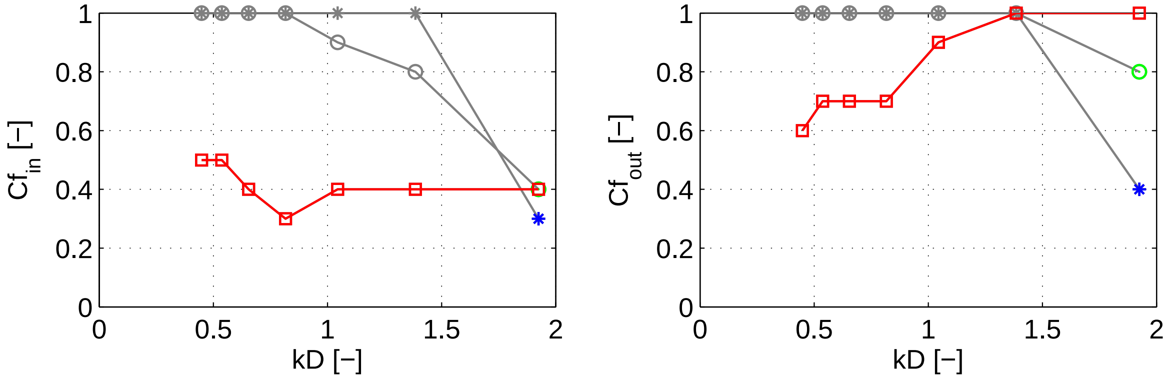

(b) *Raised panel model, fixed static pressure*

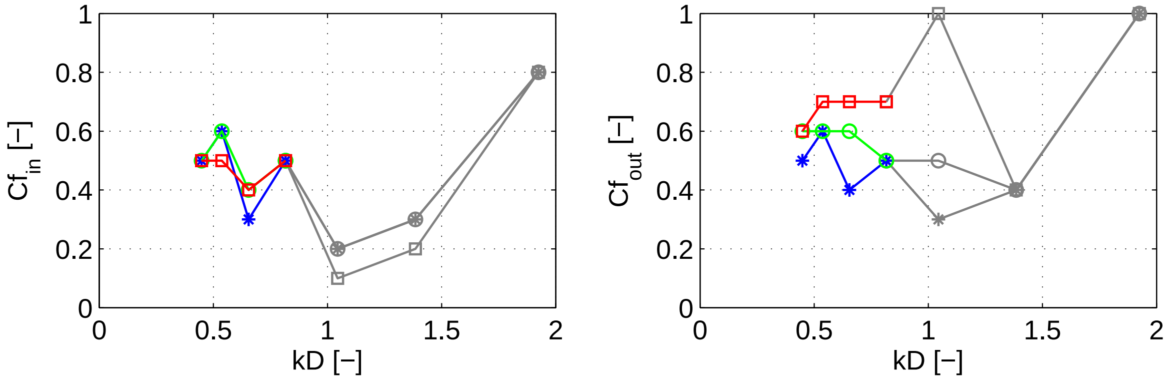

(c) *Double panel model, fluctuating static pressure*

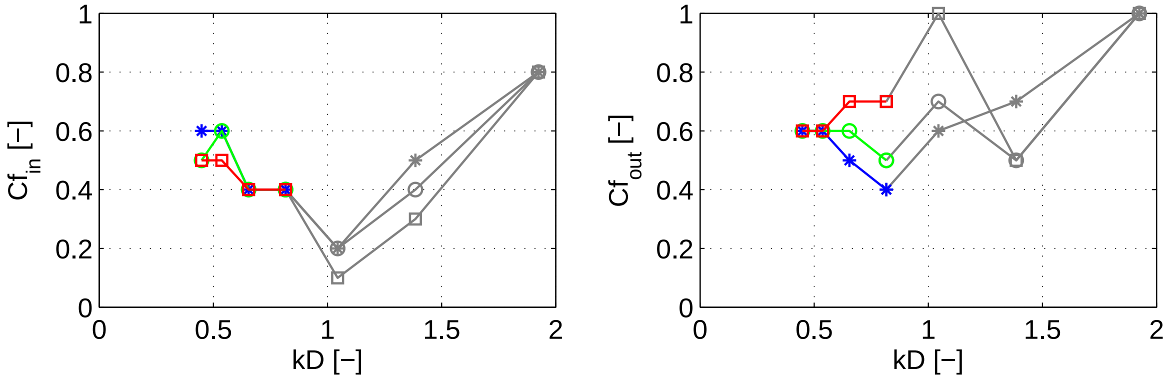

(d) *Double panel model, fixed static pressure*

Figure D-1: *Tuned flow coefficients for each of the model variations. Gray lines indicate that no resembling fit was found.*

H[m]	T[s]=5.6		6.6		7.6		8.6		9.6		10.6		11.6	
1	0.3	0.4	0.3	0.5	0.3	0.5	0.4	0.5	0.5	0.5	0.5	0.5	0.5	0.5
2	0.3	0.7	0.4	0.7	0.4	0.7	0.4	0.6	0.4	0.6	0.6	0.6	0.6	0.6
3	0.4	1.0	0.4	1.0	0.3	0.9	0.3	0.7	0.4	0.7	0.5	0.7	0.5	0.6

(a) *Raised panel model - Fluctuating static pressure*

H[m]	T[s]=5.6		6.6		7.6		8.6		9.6		10.6		11.6	
1	0.3	0.4	1.0	1.0	1.0	1.0	1.0	1.0	1.0	1.0	1.0	1.0	1.0	1.0
2	0.4	0.8	0.8	1.0	0.9	1.0	1.0	1.0	1.0	1.0	1.0	1.0	1.0	1.0
3	0.4	1.0	0.4	1.0	0.4	0.9	0.3	0.7	0.4	0.7	0.5	0.7	0.5	0.6

(b) *Raised panel model - Fixed static pressure*

H[m]	T[s]=5.6		6.6		7.6		8.6		9.6		10.6		11.6	
1	0.8	1.0	0.3	0.4	0.2	0.3	0.5	0.5	0.3	0.4	0.6	0.6	0.5	0.5
2	0.8	1.0	0.3	0.4	0.2	0.5	0.5	0.5	0.4	0.6	0.6	0.6	0.5	0.6
4	0.8	1.0	0.2	0.4	0.1	1.0	0.5	0.7	0.4	0.7	0.5	0.7	0.5	0.6

(c) *Double panel model - Fluctuating static pressure*

H[m]	T[s]=5.6		6.6		7.6		8.6		9.6		10.6		11.6	
1	0.8	1.0	0.5	0.7	0.2	0.6	0.4	0.4	0.4	0.5	0.6	0.6	0.6	0.6
2	0.8	1.0	0.4	0.5	0.2	0.7	0.4	0.5	0.4	0.6	0.6	0.6	0.5	0.6
4	0.8	1.0	0.3	0.5	0.1	1.0	0.4	0.7	0.4	0.7	0.5	0.6	0.5	0.6

(d) *Double panel model - Fixed static pressure*

Table D-1: *Tuned flow coefficients for each of the model variations. Red values indicate that no resembling fit was found. H = wave height, T = wave period, first column under period =* C_f^{in} *and second column under period =* C_f^{out}

D-4 Time Traces 1m Wave Height

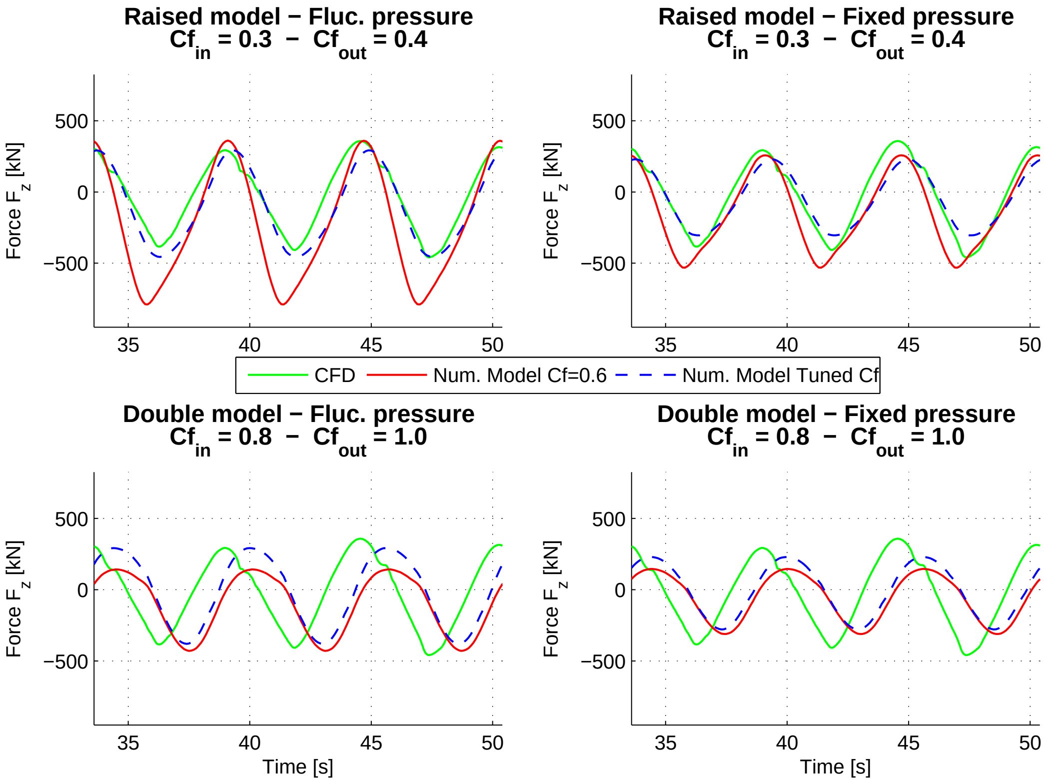

Figure D-2: *Heave force time trace. Wave height = 1m, wave period = 5.6s.*

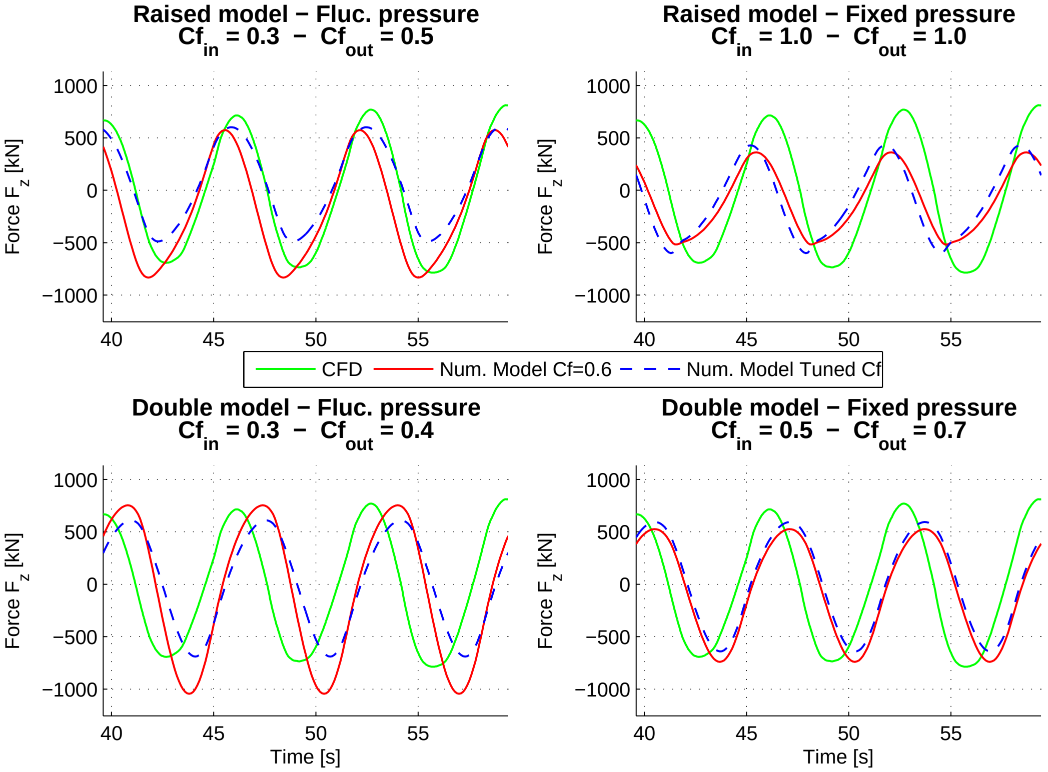

Figure D-3: *Heave force time trace. Wave height = 1m, wave period = 6.6s.*

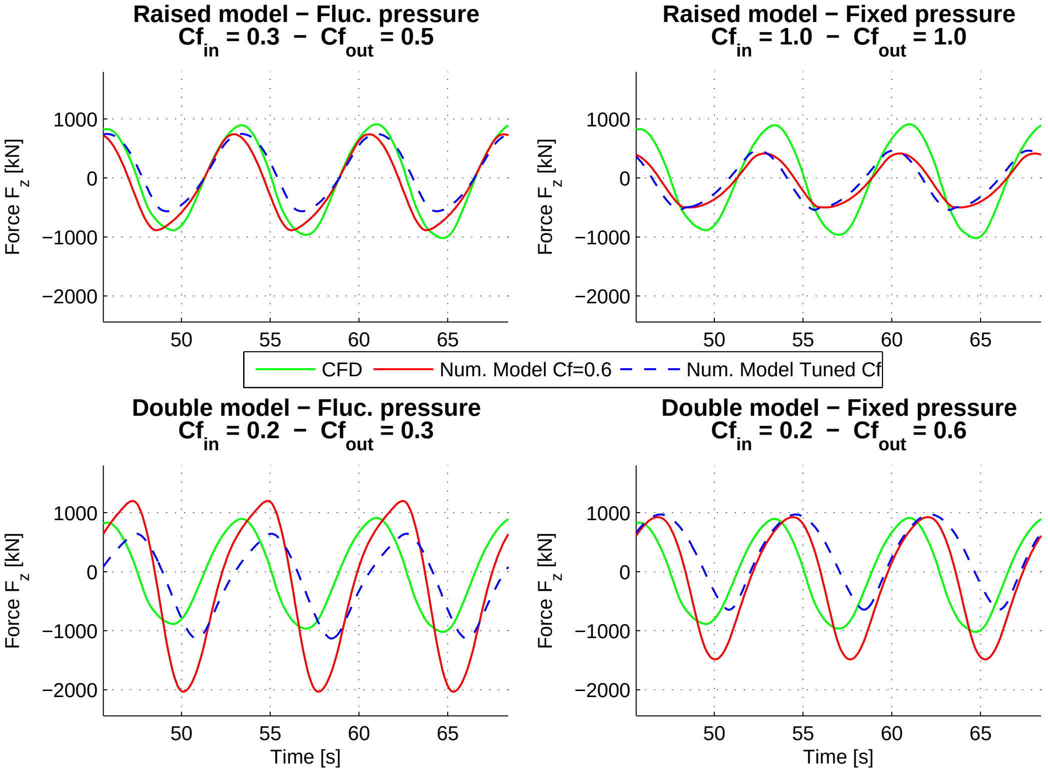

Figure D-4: *Heave force time trace. Wave height = 1m, wave period = 7.6s.*

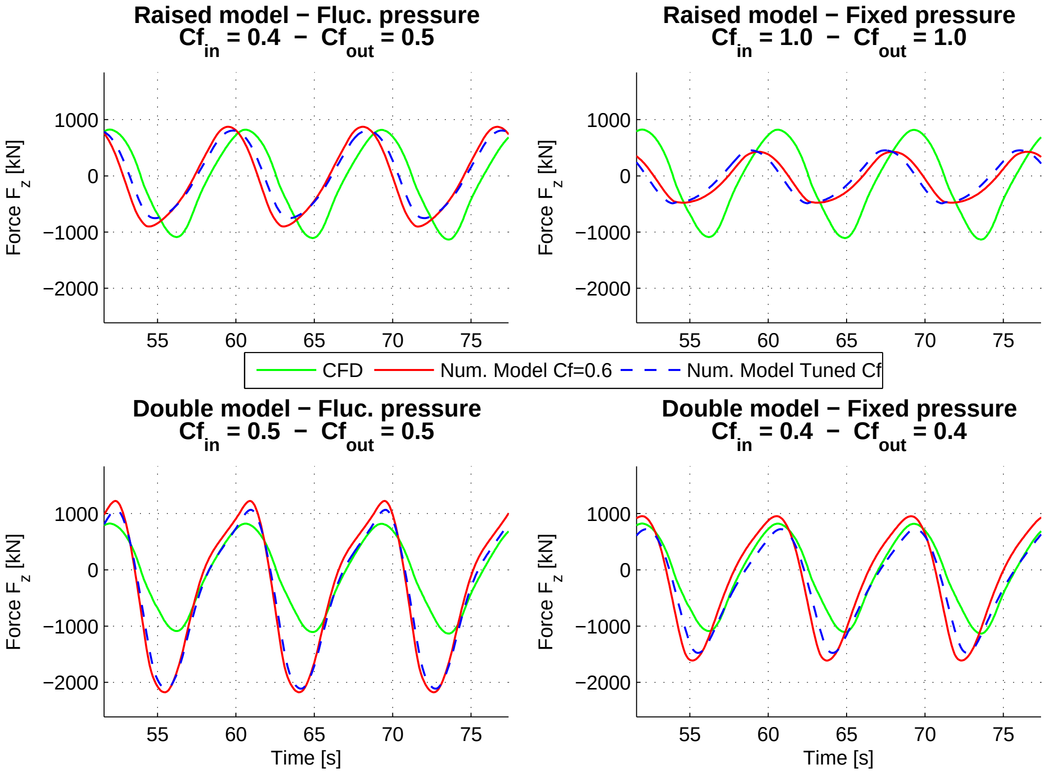

Figure D-5: *Heave force time trace. Wave height = 1m, wave period = 8.6s.*

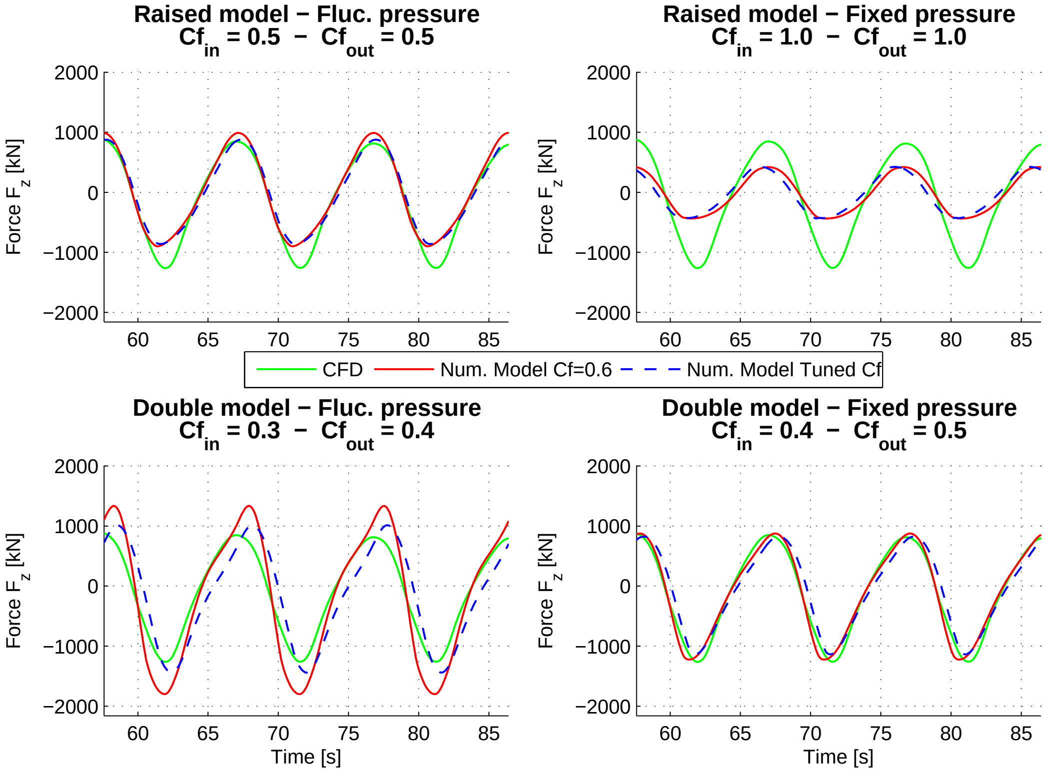

Figure D-6: *Heave force time trace. Wave height = 1m, wave period = 9.6s.*

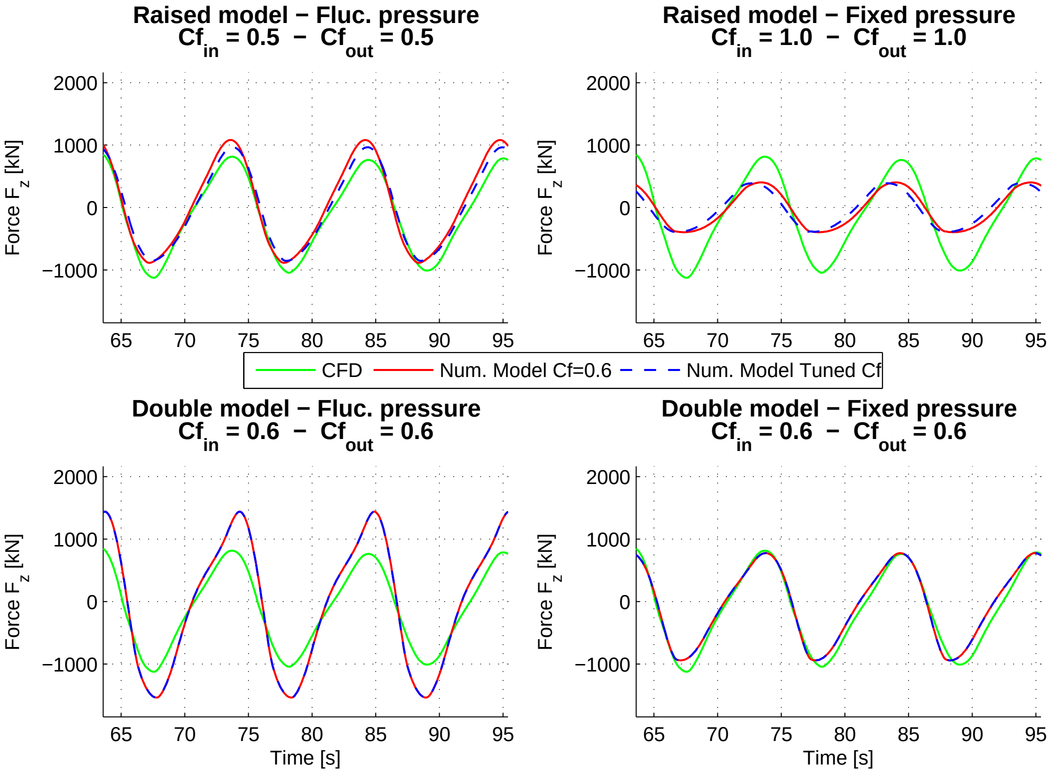

Figure D-7: *Heave force time trace. Wave height = 1m, wave period = 10.6s.*

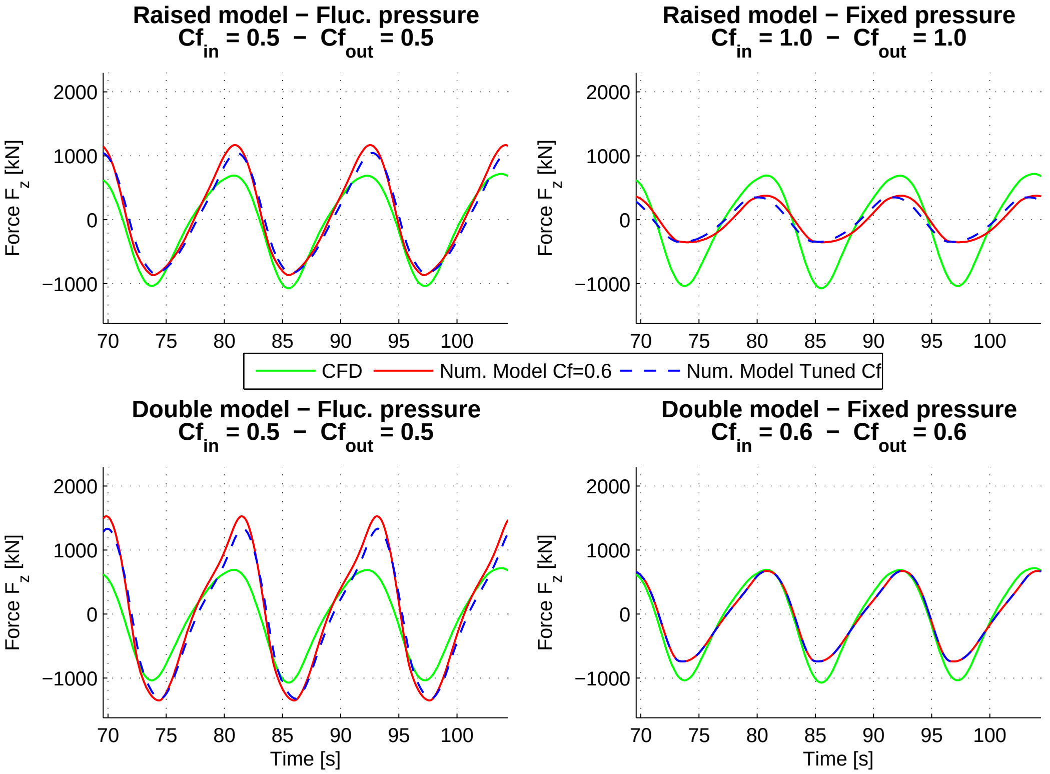

Figure D-8: *Heave force time trace. Wave height = 1m, wave period = 11.6s.*

D-5 Time Traces 2m Wave Height

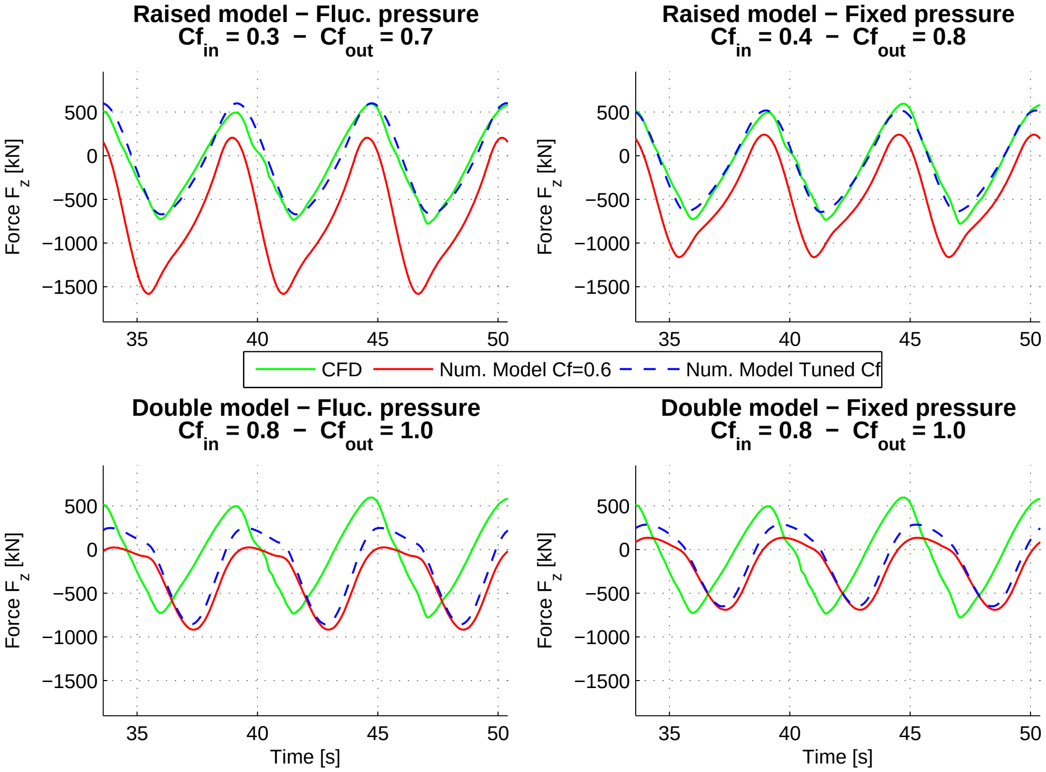

Figure D-9: *Heave force time trace. Wave height = 2m, wave period = 5.6s.*

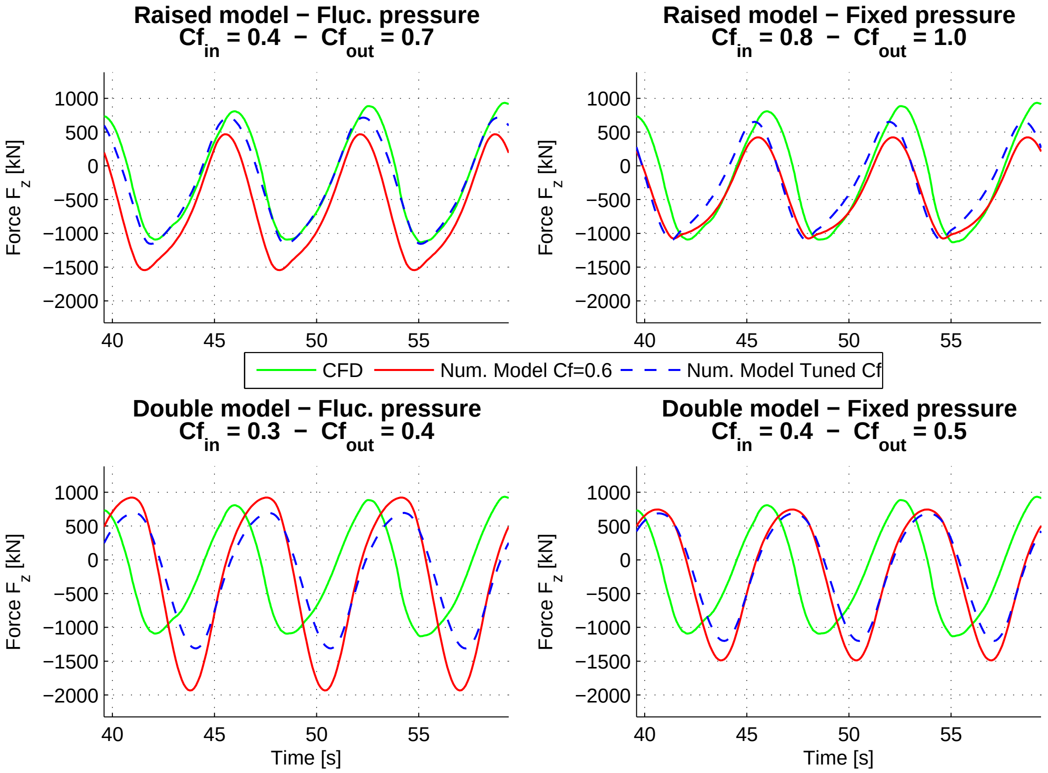

Figure D-10: *Heave force time trace. Wave height = 2m, wave period = 6.6s.*

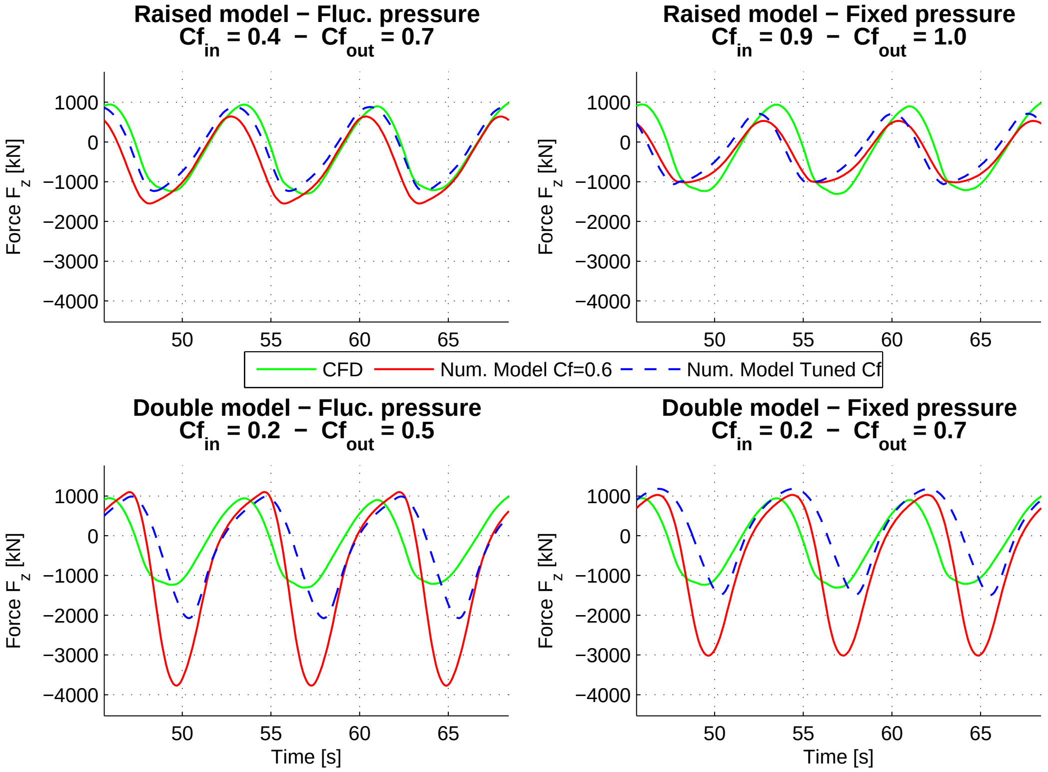

Figure D-11: *Heave force time trace. Wave height = 2m, wave period = 7.6s.*

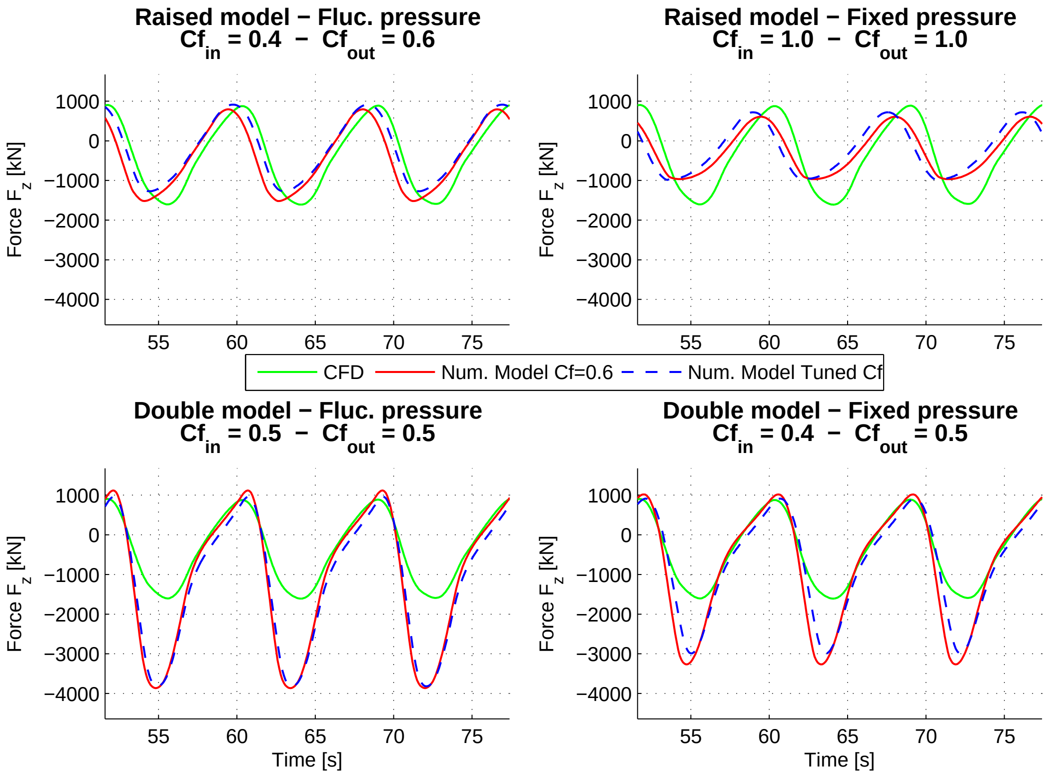

Figure D-12: *Heave force time trace. Wave height = 2m, wave period = 8.6s.*

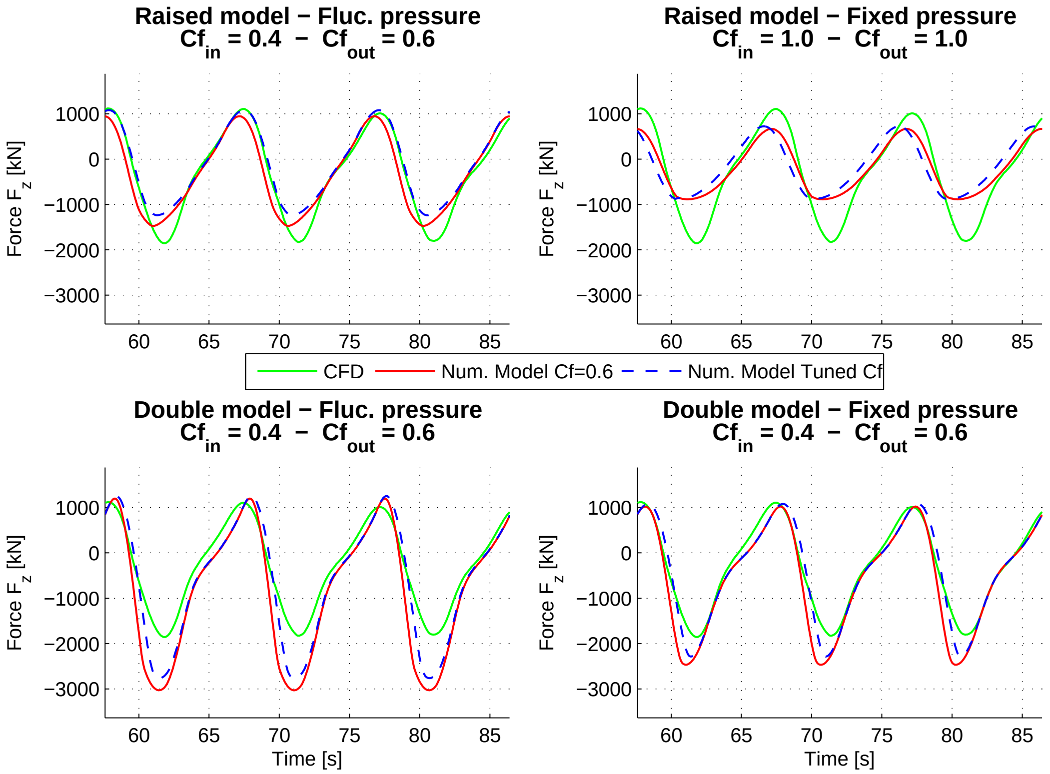

Figure D-13: *Heave force time trace. Wave height = 2m, wave period = 9.6s.*

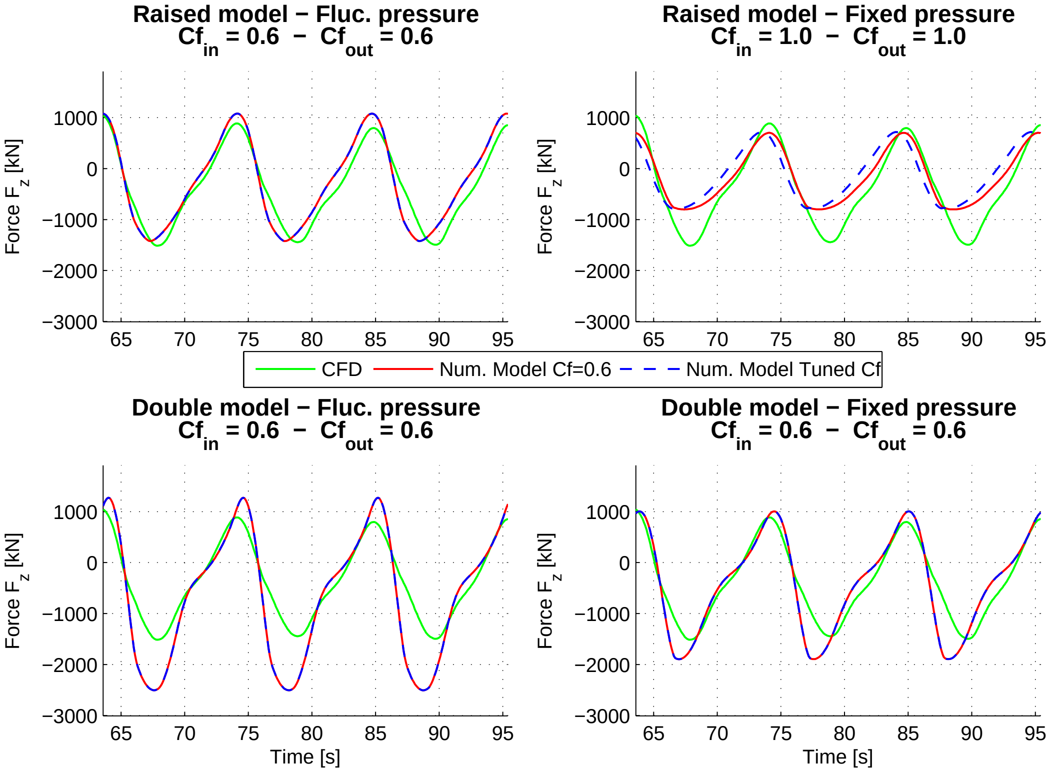

Figure D-14: *Heave force time trace. Wave height = 2m, wave period = 10.6s.*

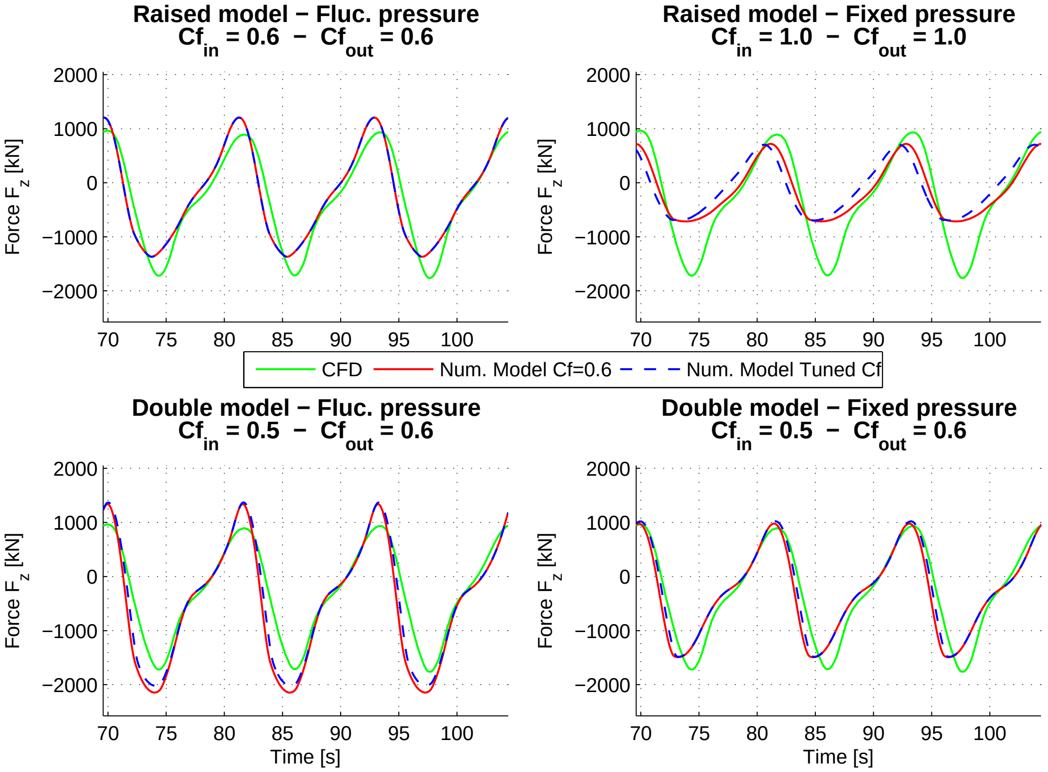

Figure D-15: *Heave force time trace. Wave height = 2m, wave period = 11.6s.*

D-6 Time Traces 4m Wave Height

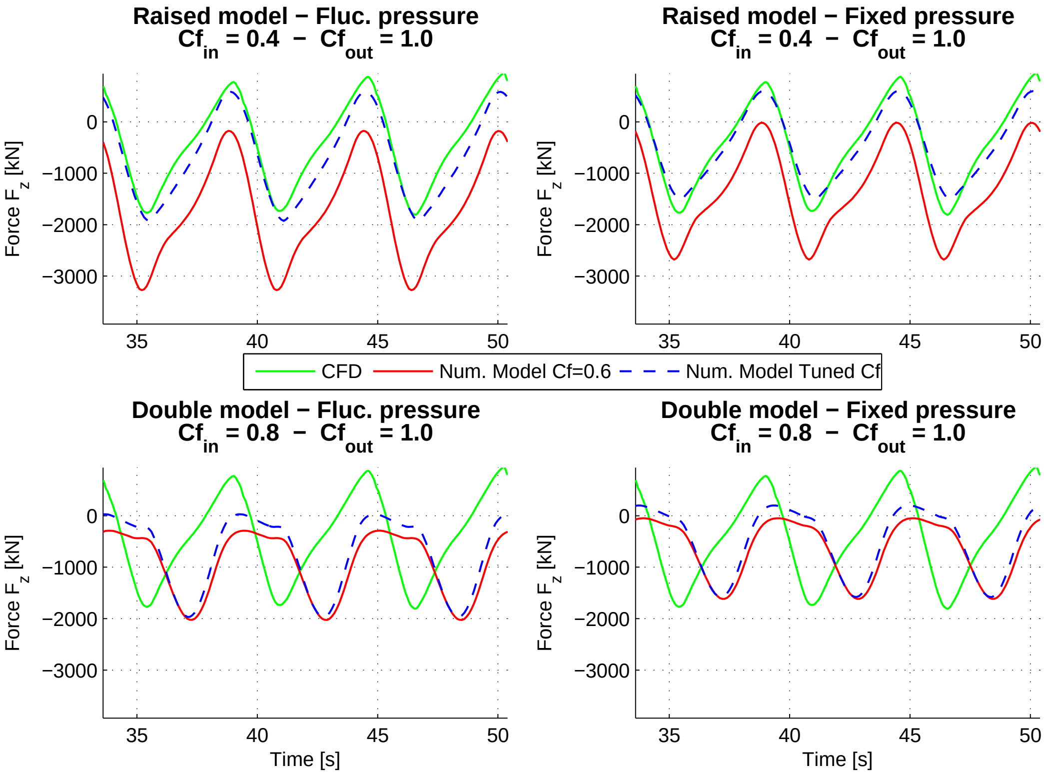

Figure D-16: *Heave force time trace. Wave height = 4m, wave period = 5.6s.*

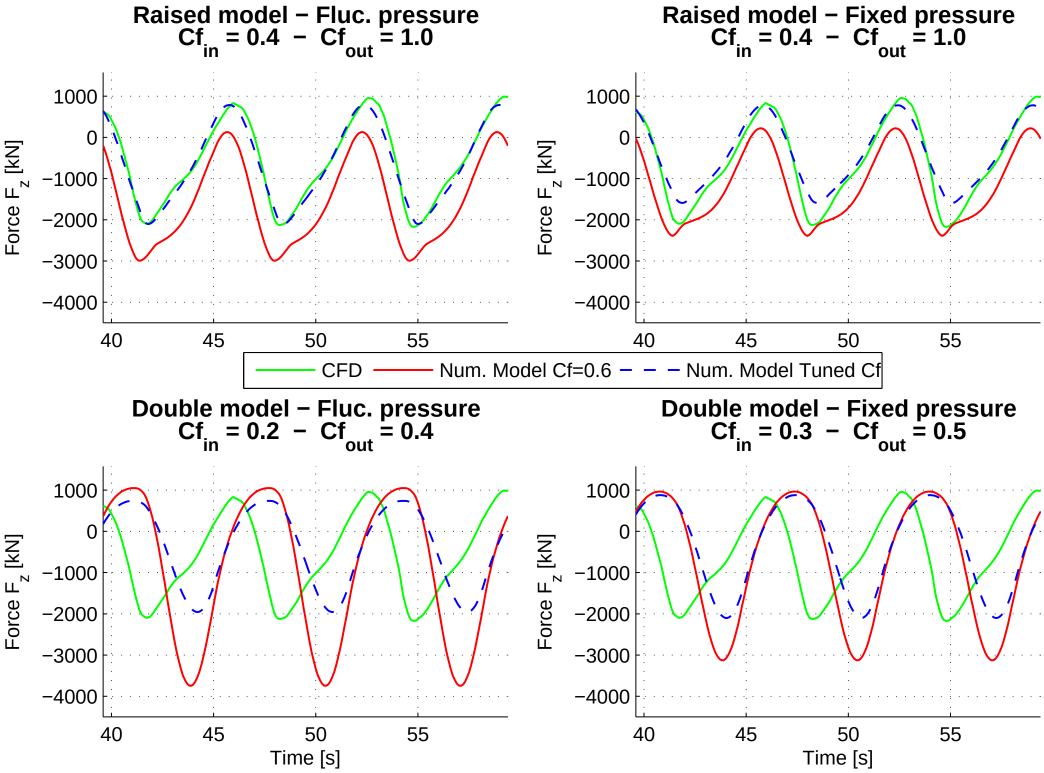

Figure D-17: *Heave force time trace. Wave height = 4m, wave period = 6.6s.*

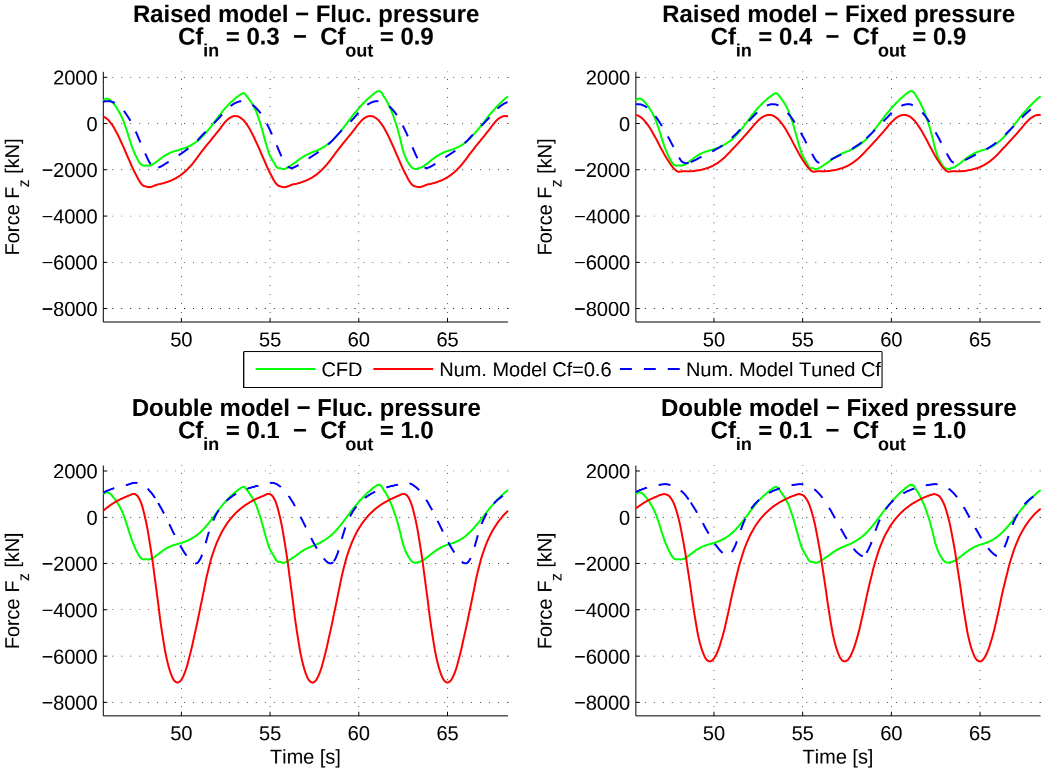

Figure D-18: *Heave force time trace. Wave height = 4m, wave period = 7.6s.*

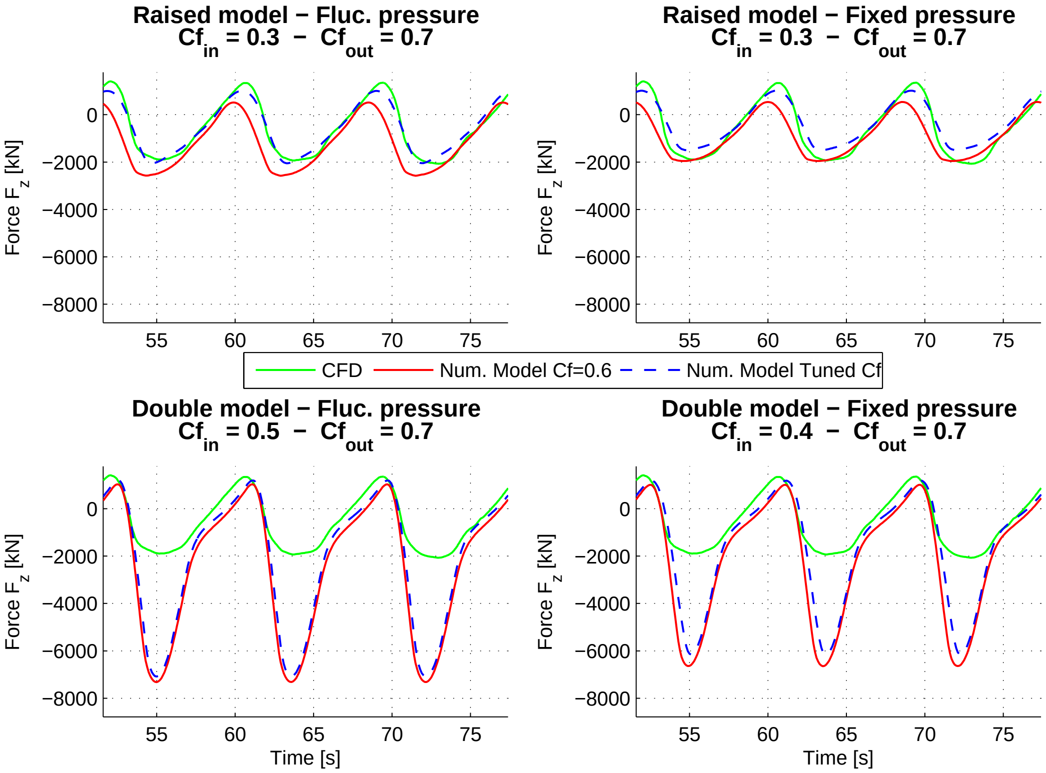

Figure D-19: *Heave force time trace. Wave height = 4m, wave period = 8.6s.*

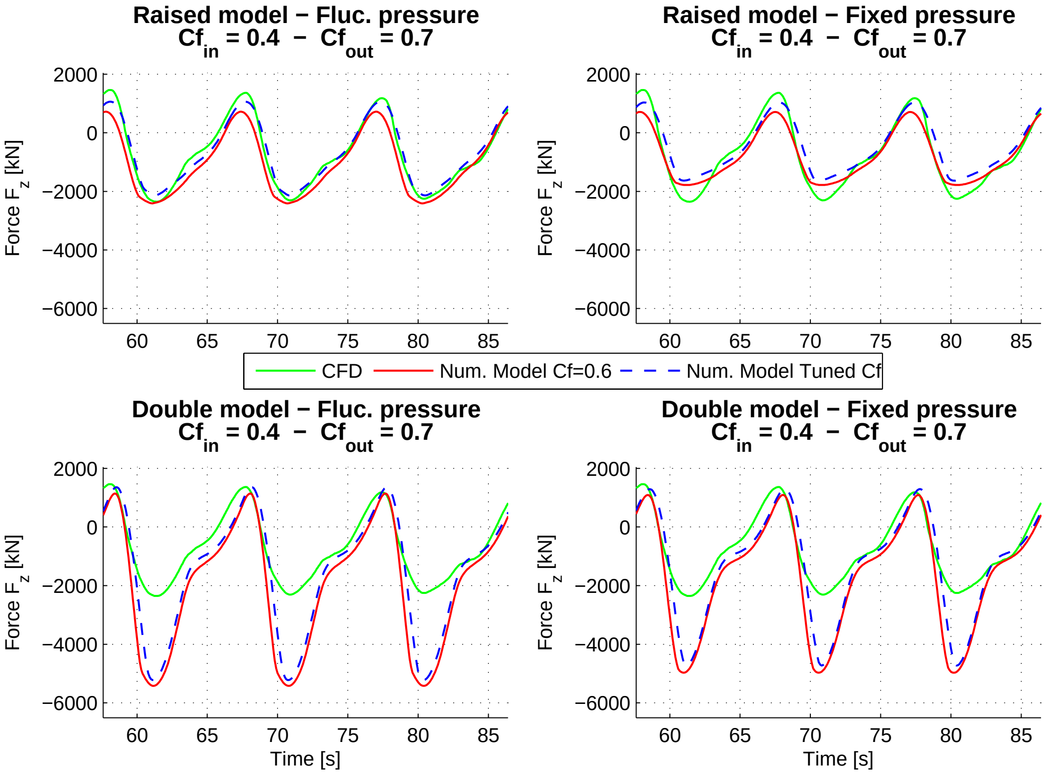

Figure D-20: *Heave force time trace. Wave height = 4m, wave period = 9.6s.*

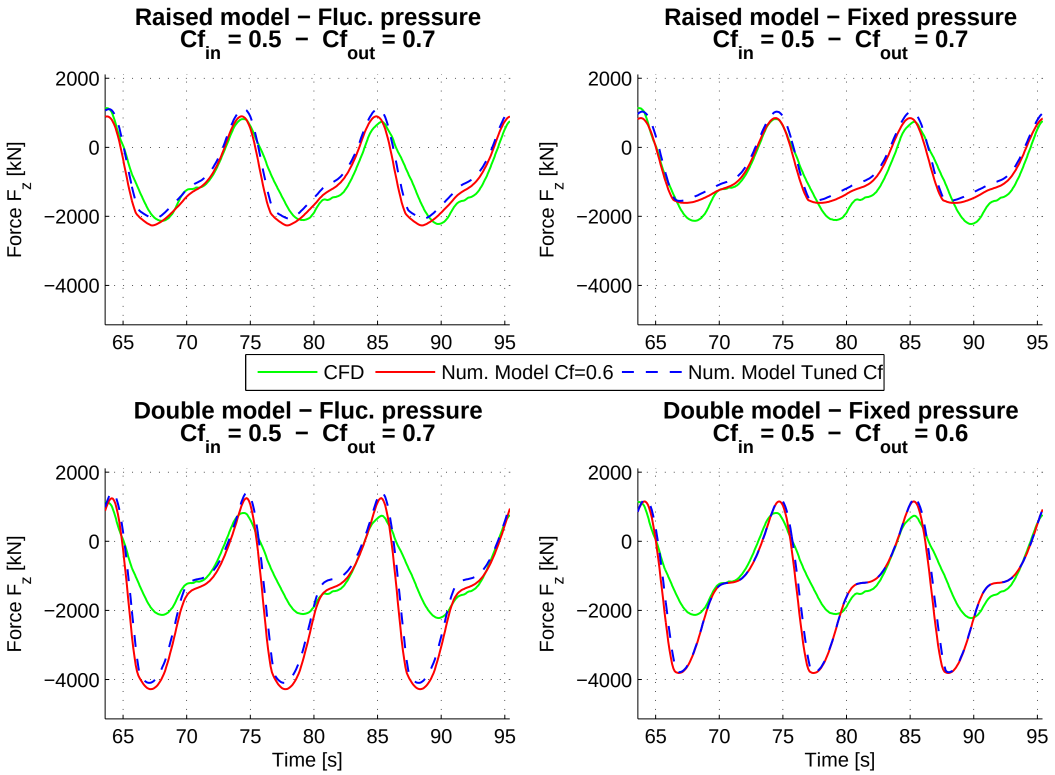

Figure D-21: *Heave force time trace. Wave height = 4m, wave period = 10.6s.*

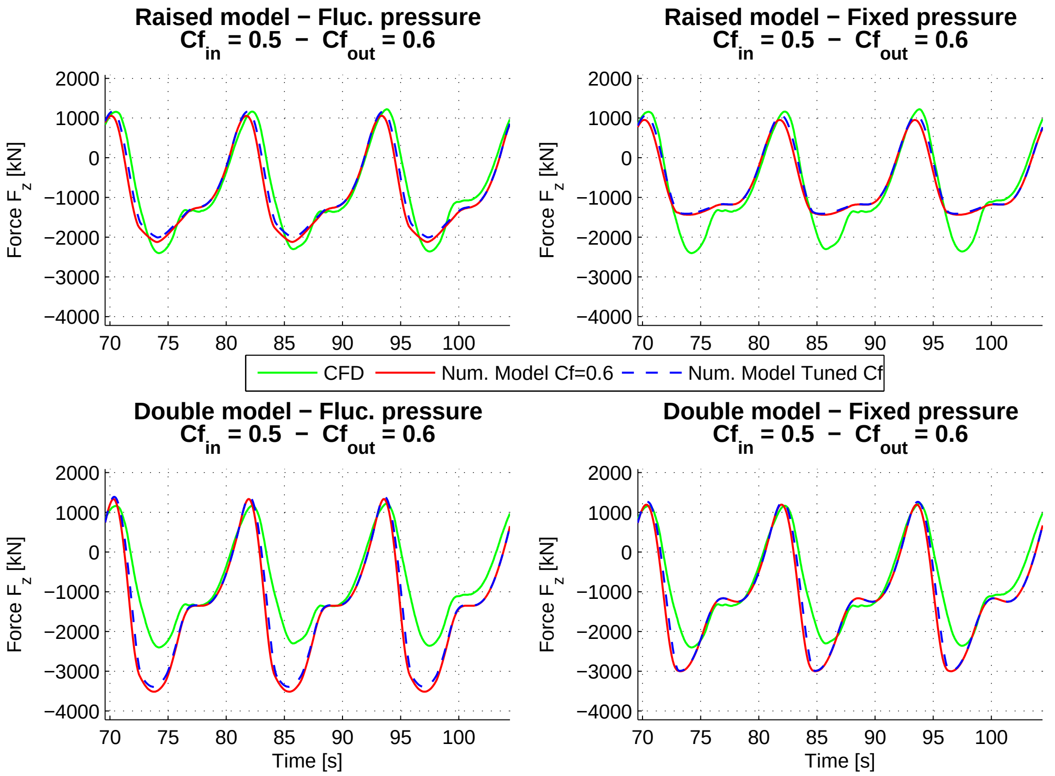

Figure D-22: *Heave force time trace. Wave height = 4m, wave period = 11.6s.*

Appendix E

Irregular Waves Results Cylinder

E-1 Surge force RAOs and phases

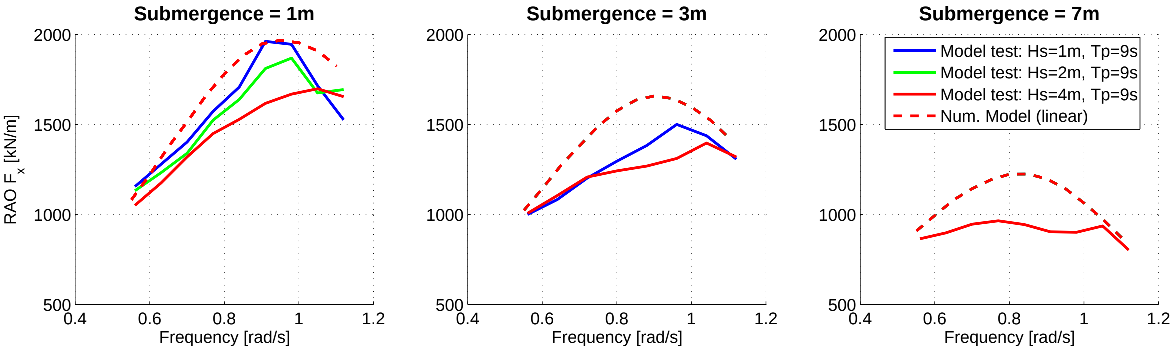

(a) *Raised panel model*

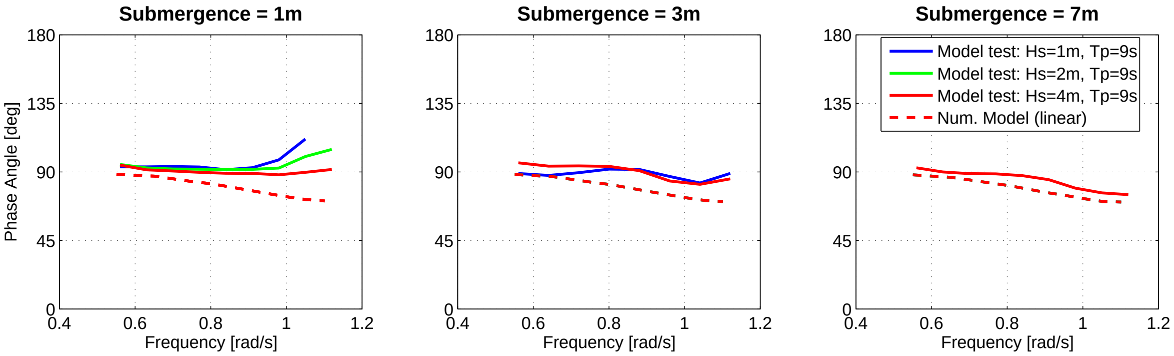

(b) *Raised panel model*

Figure E-1: *Surge force RAOs and phases for the raised panel model.*

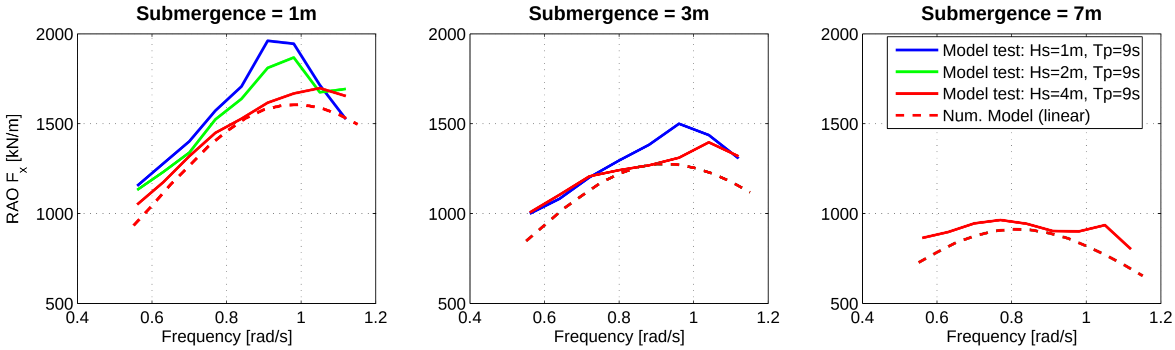

(a) *Double panel model*

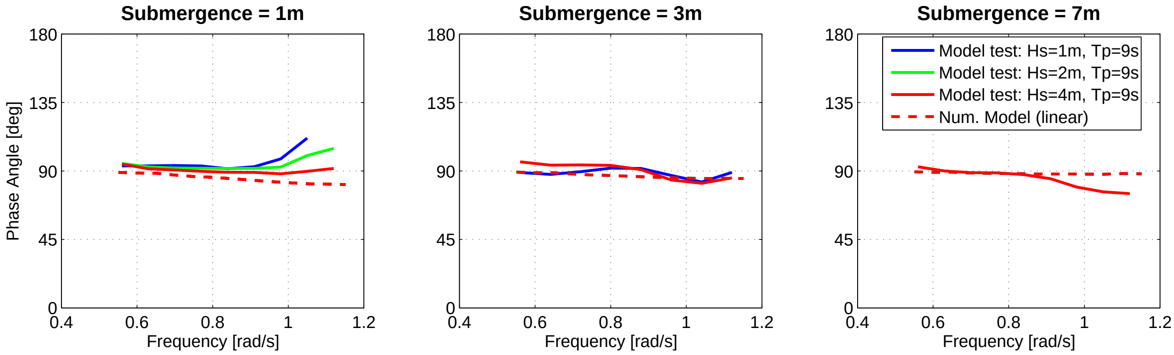

(b) *Double panel model*

Figure E-2: *Surge force RAOs and phases for the double panel model.*

E-2 Heave force RAOs and phases

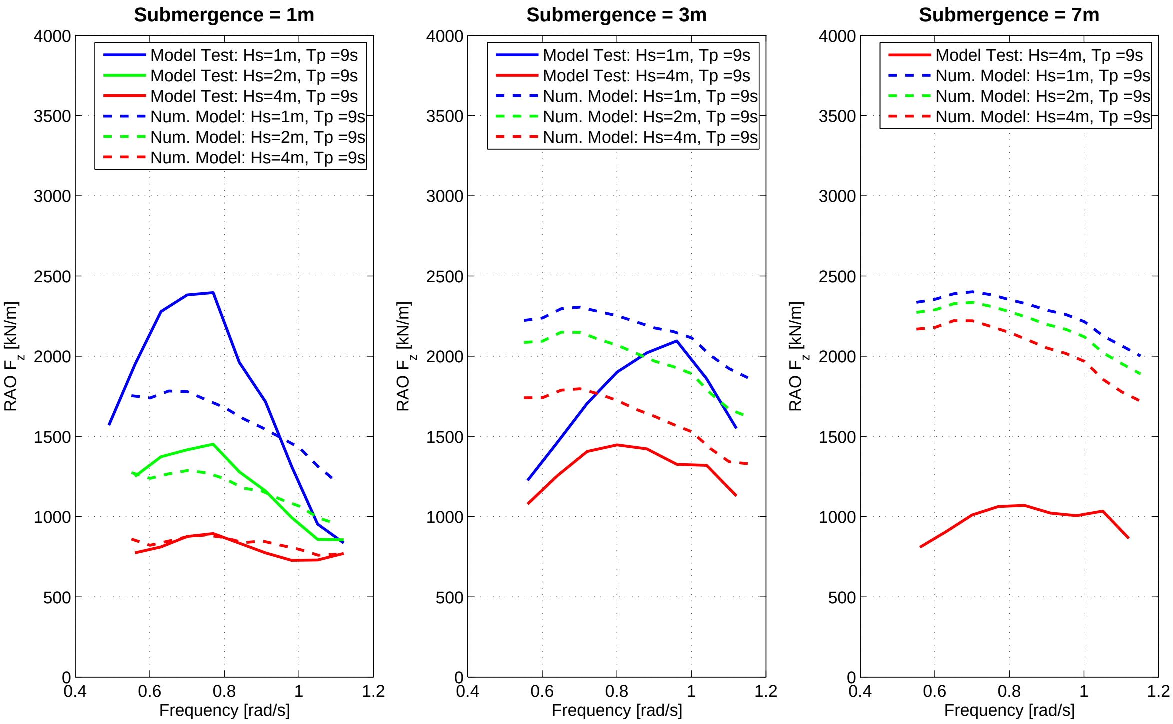

(a) *Raised panel model - fluctuating static pressure*

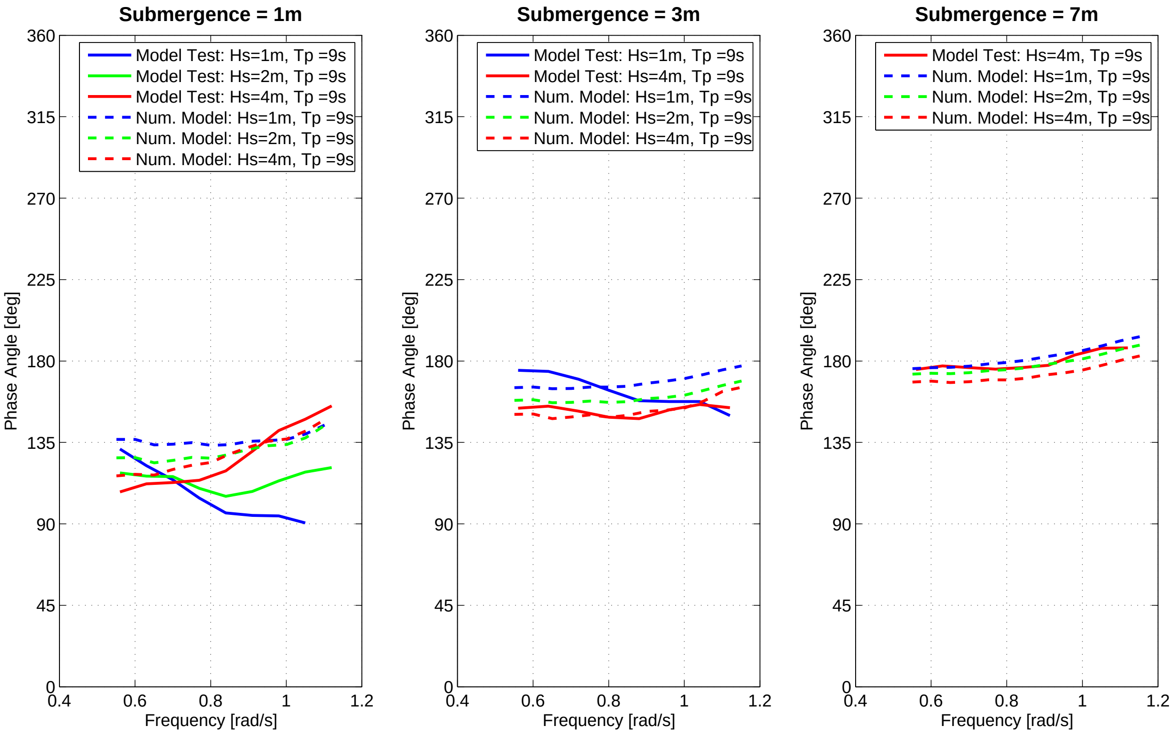

(b) *Raised panel model - fluctuating static pressure*

Figure E-3: *Heave force RAOs and phases for the raised panel model including a fluc. static pressure.*

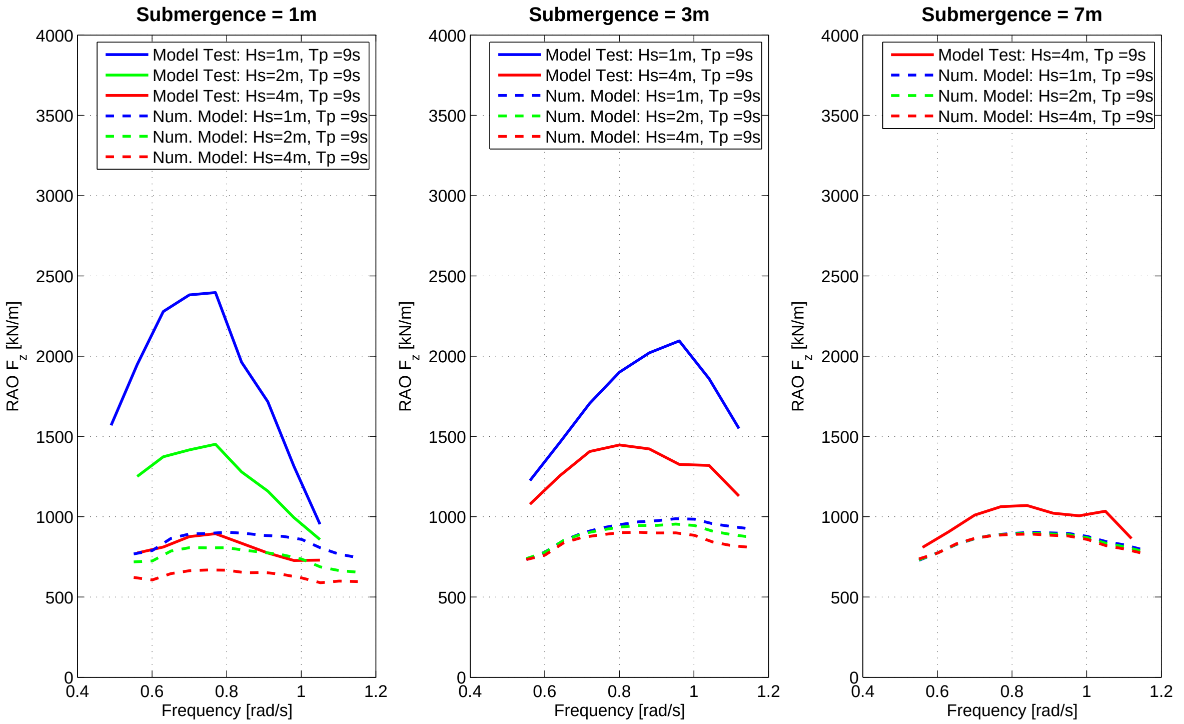

(a) *Raised panel model - fixed static pressure*

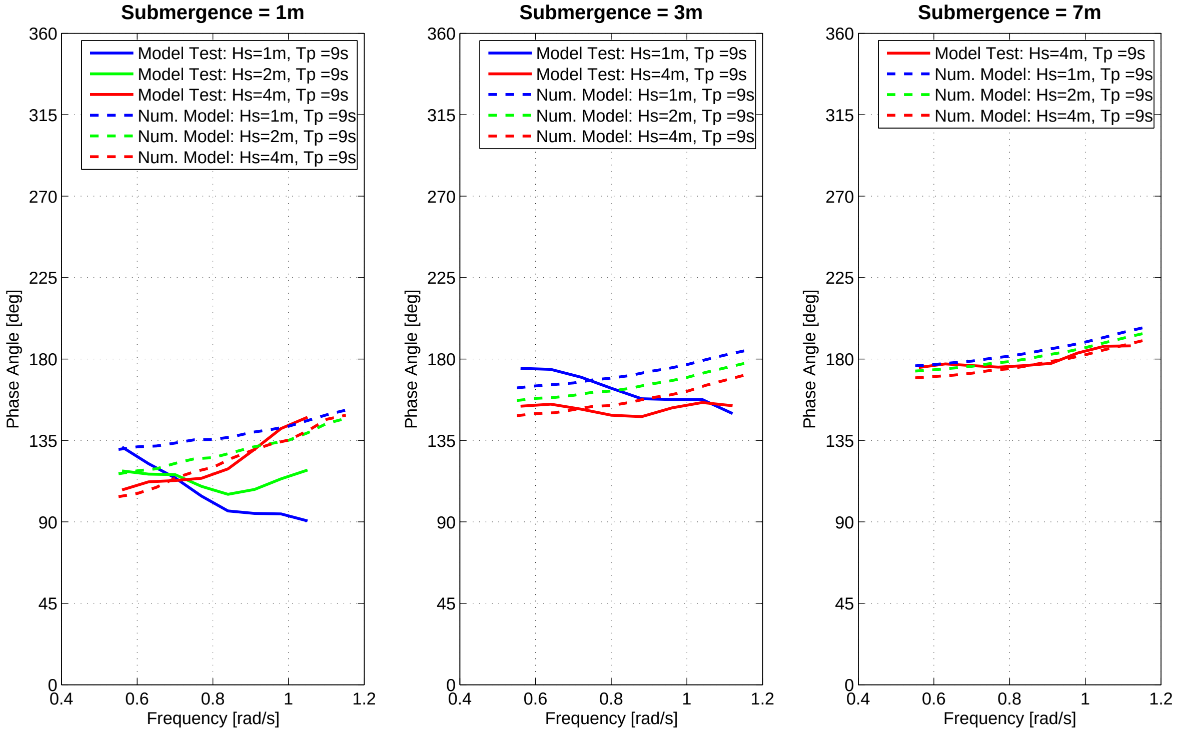

(b) *Raised panel model - fixed static pressure*

Figure E-4: *Heave force RAOs and phases for the raised panel model including a fixed static pressure.*

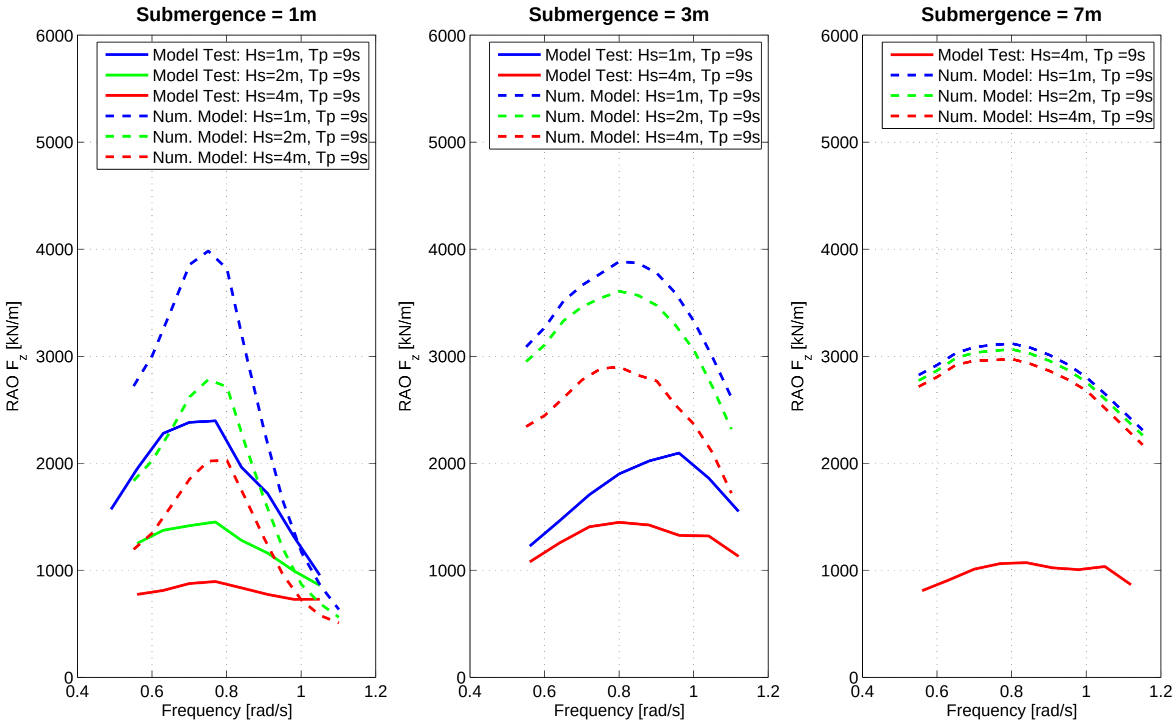

(a) *Double panel model - fluctuating static pressure (different y-scaling used)*

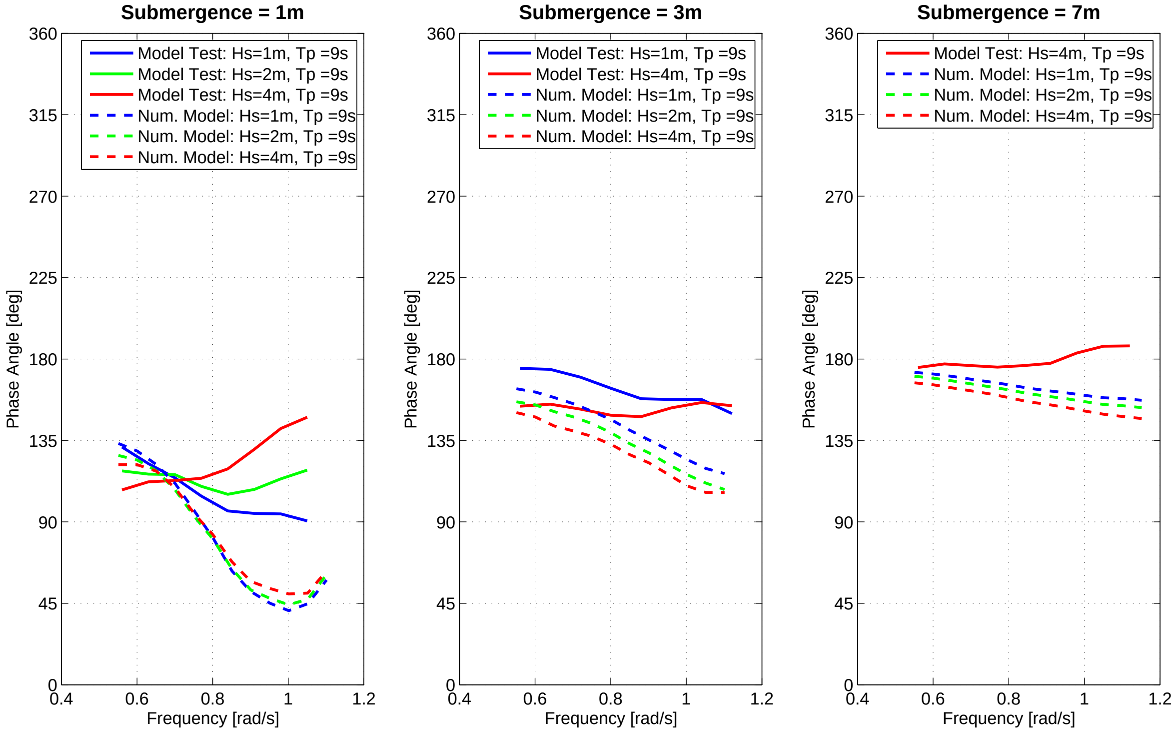

(b) *Double panel model - fluctuating static pressure*

Figure E-5: *Heave force RAOs and phases for the double panel model including a fluc. static pressure.*

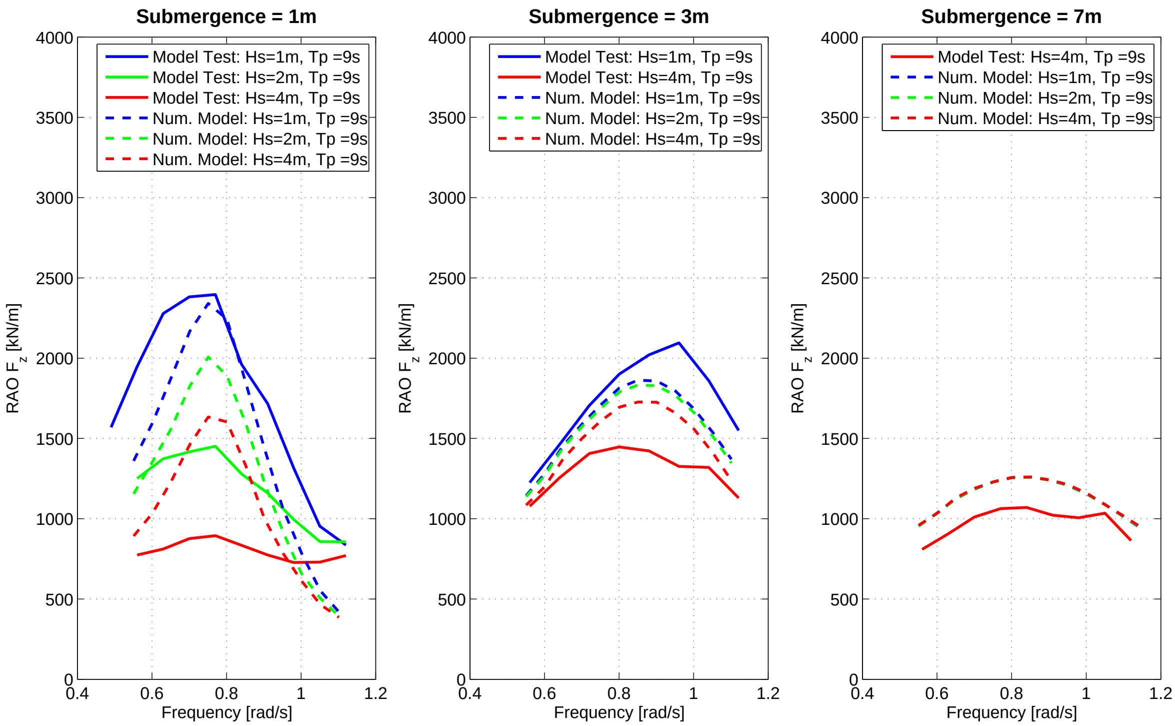

(a) *Double panel model - fixed static pressure*

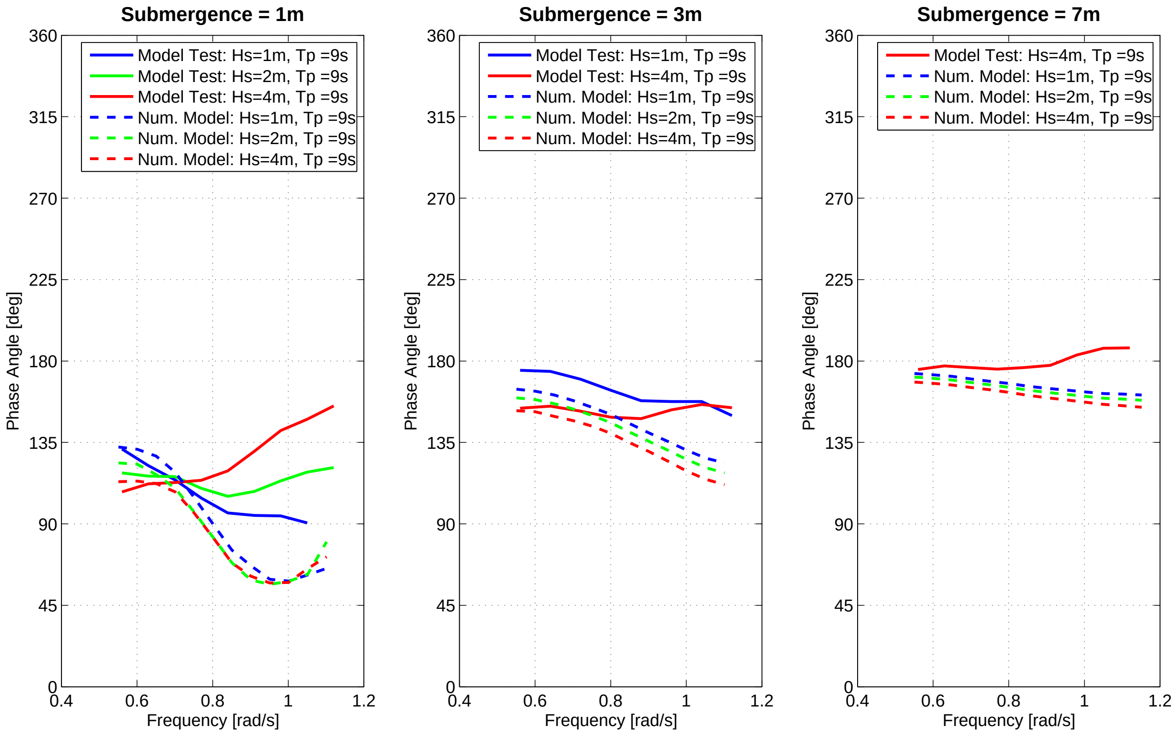

(b) *Double panel model - fixed static pressure*

Figure E-6: *Heave force RAOs and phases for the double panel model including a fixed static pressure.*

Appendix F

Numerical Model Details for SSCV Thialf

F-1 Panel Models

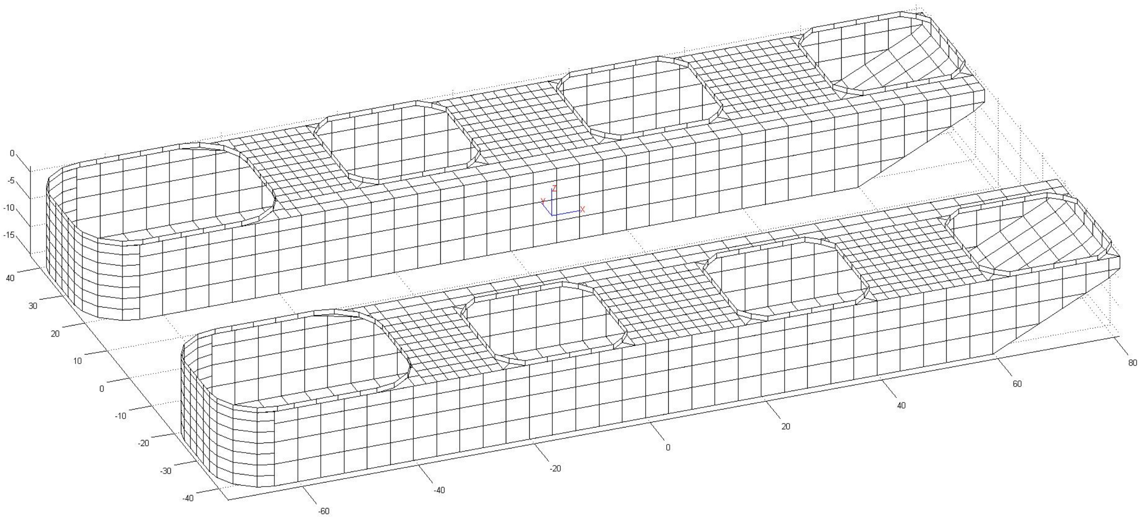

Figure F-1: *Original panel model of the SSCV Thialf at 14.5m draft*

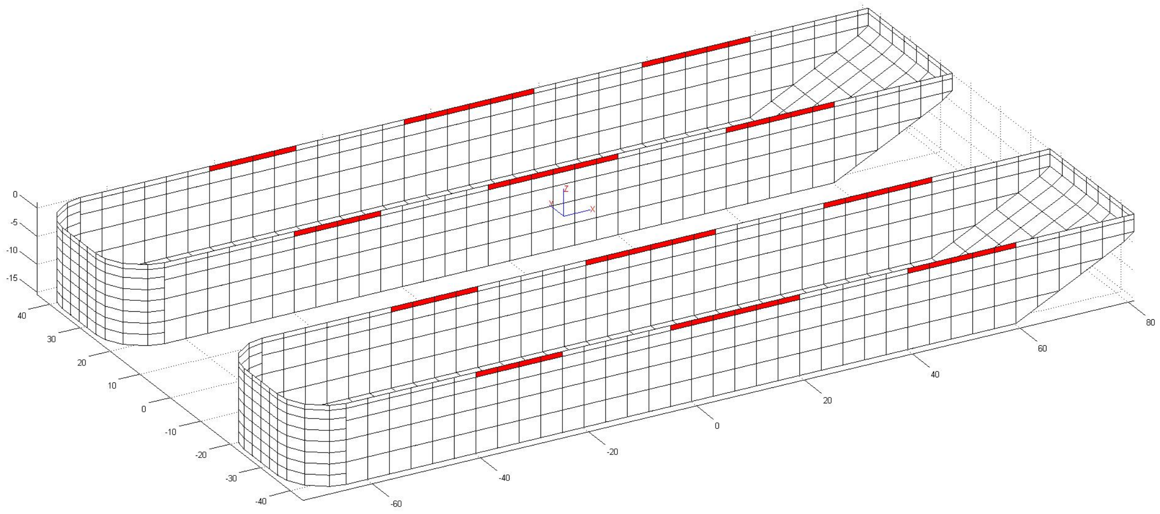

Figure F-2: *Raised panel model of the SSCV Thialf at 14.5m draft*

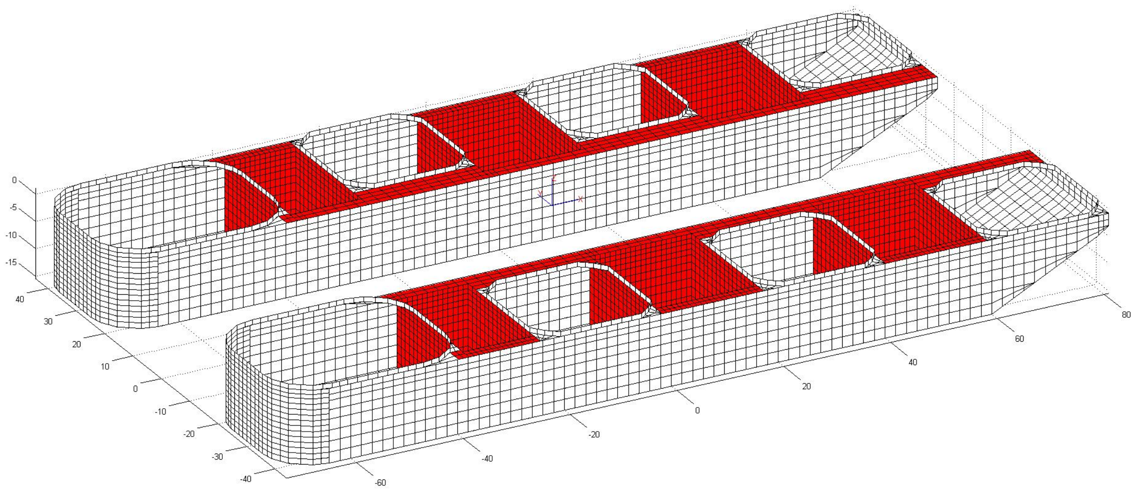

Figure F-3: *Double panel model of the SSCV Thialf at 14.5m draft*

F-2 Force RAOs

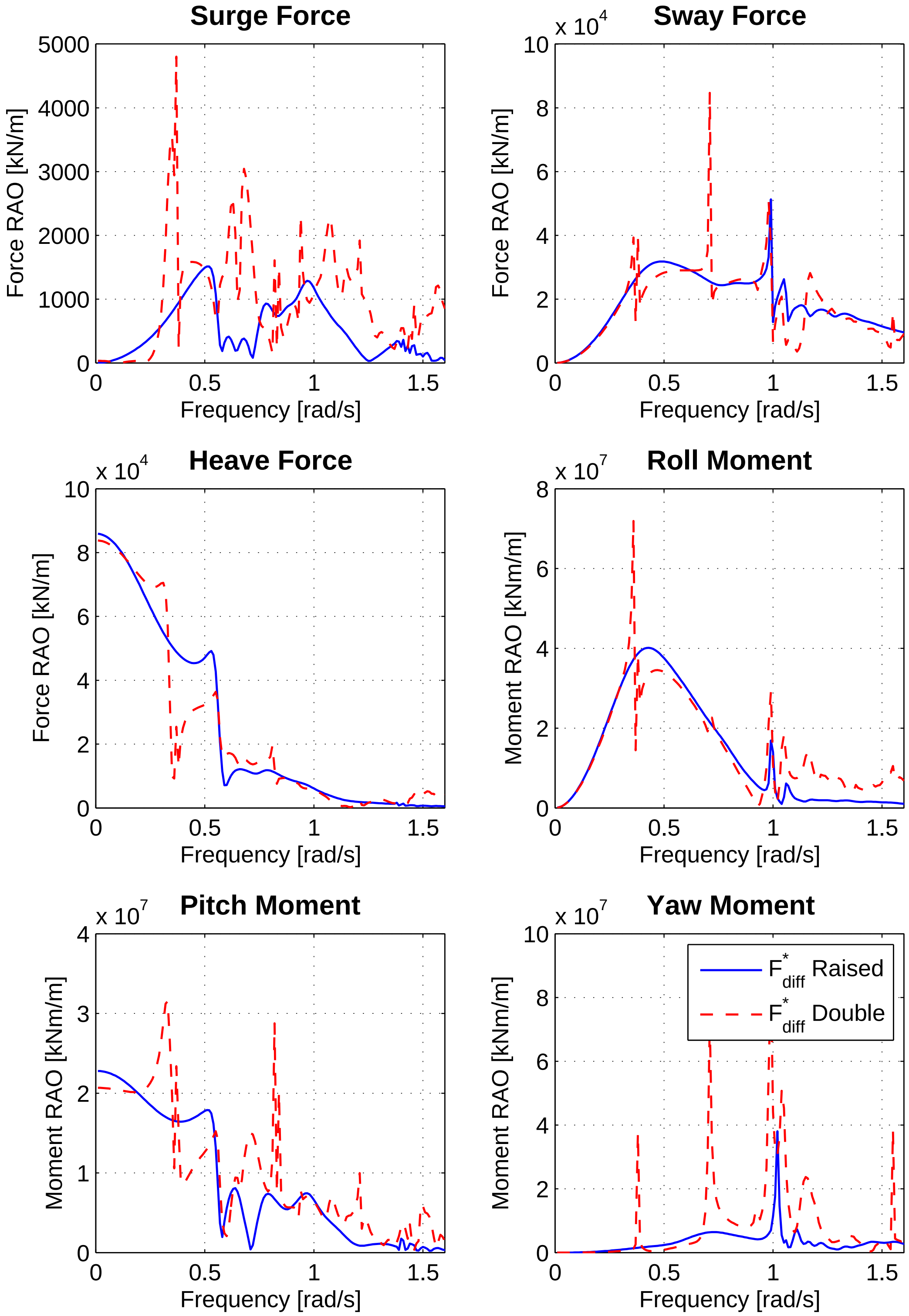

Figure F-4: *Diffraction force RAOs on the outer surface for both panel models*

F-3 Motion RAOs

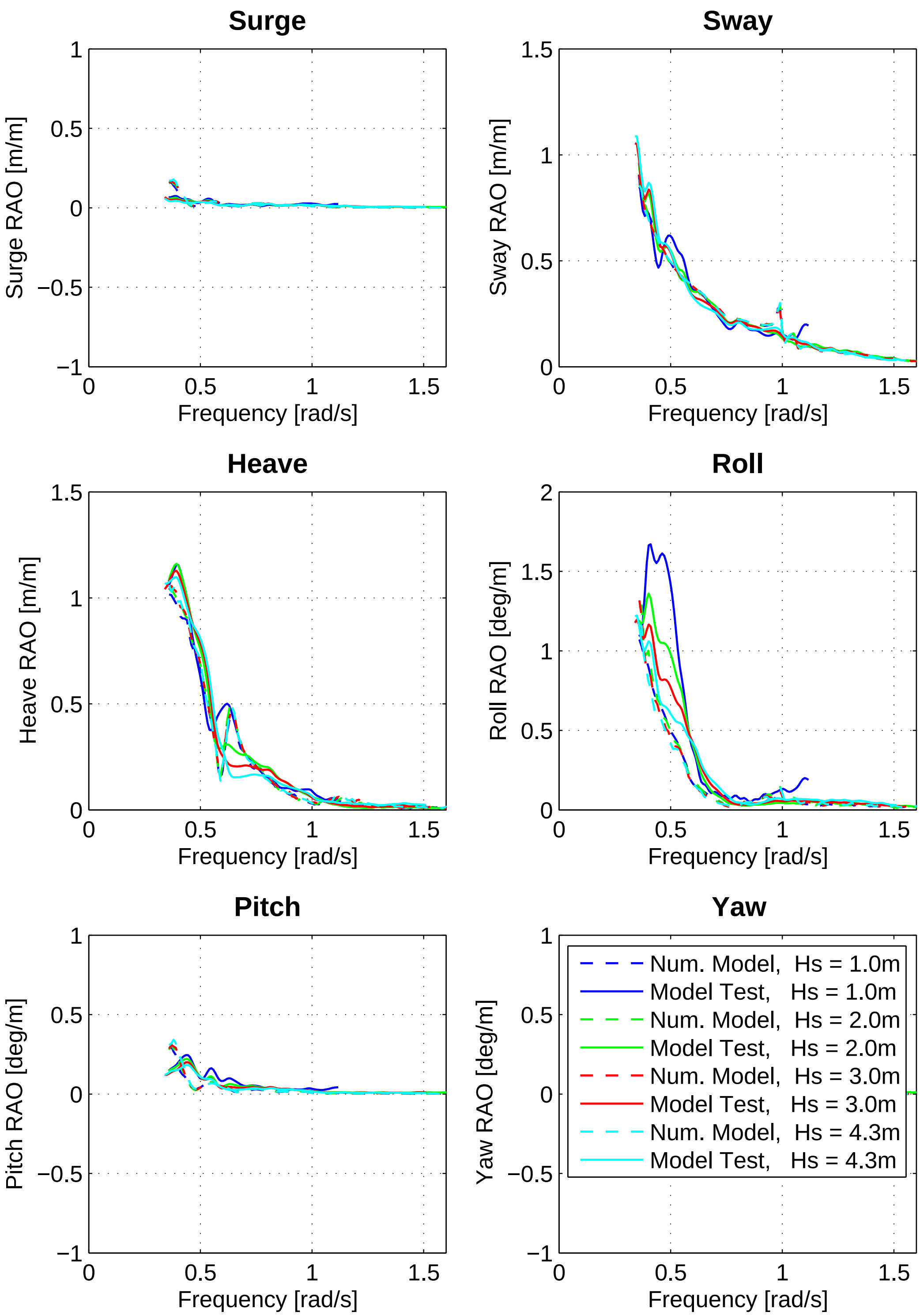

Figure F-5: *Resulting motion RAOs using the raised panel model.*

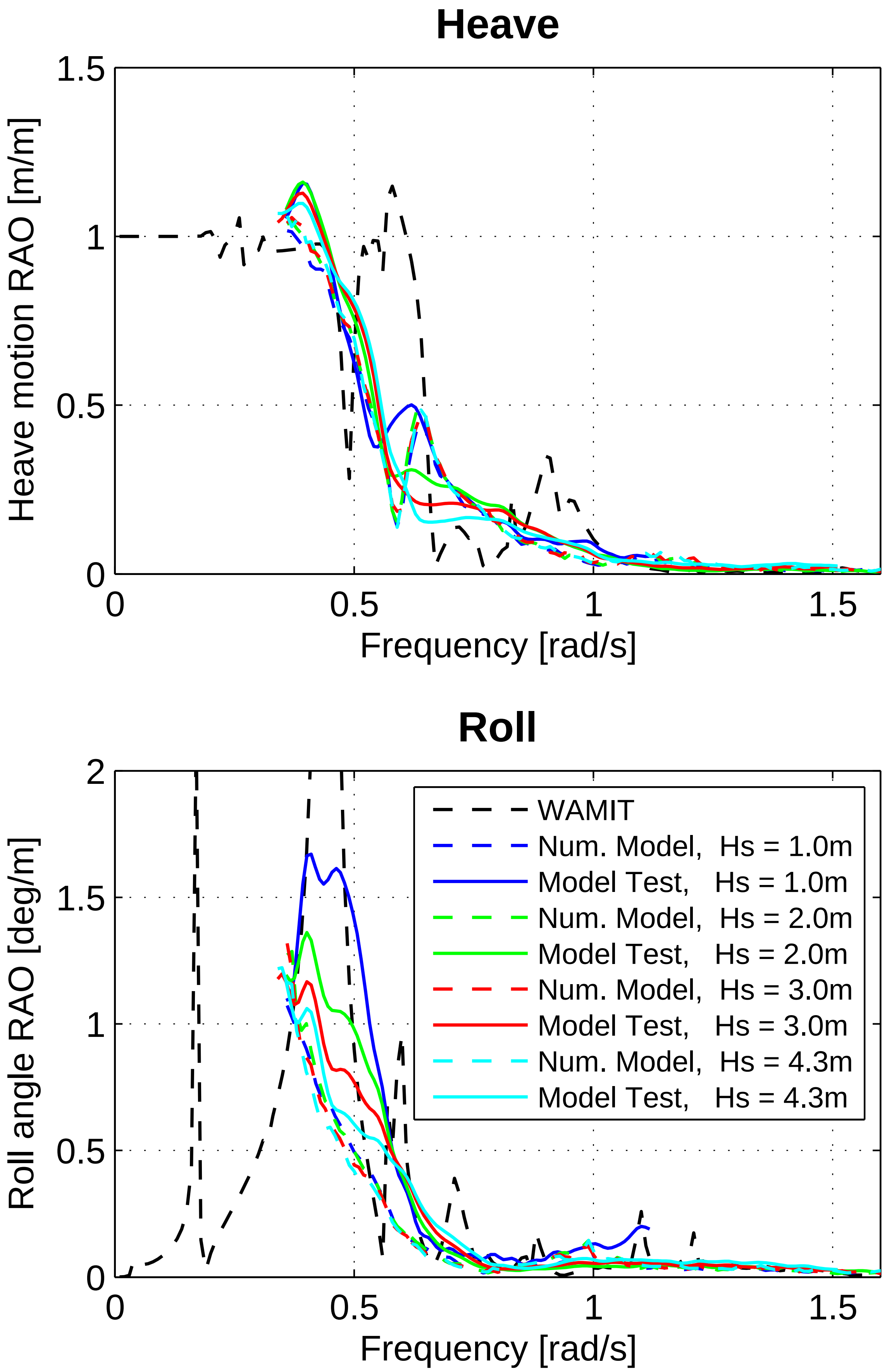

Figure F-6: *Motion RAOs for heave and roll, obtained by the numerical model using the raised panel model. Including motion RAOs obtained by WAMIT.*

Bibliography

[1] WAMIT inc. *User Manual.* MIT, MA, USA, 2013.

[2] H. Ottens, A. Pistidda, and R. van Dijk. CFD Analysis of Waves over a Submerged Cylinder in Close Proximity of the Free Surface. In *Proceedings of the ASME 2014 33rd International Conference on Ocean, Offshore and Arctic Engineering*, San Francisco, California, USA, 2014. OMAE2014-23451.

[3] O. van Straaten. Onderzoek naar het bewegingsgedrag van de Enforcer Serie. Master's thesis, Delft University of Technology, 1999.

[4] J.A. Pinkster. A Multi-Domain Approach in 3D Diffraction Calculations. In *Proceedings of the ASME 2011 30nd International Conference on Ocean, Offshore and Arctic Engineering*, Rotterdam, The Netherlands, 2011. OMAE2011-49414.

[5] S. Anink. Hydrodynamic Analysis of King Size Transport Vessel Offloading Operation at Open Sea. Master's thesis, Delft University of Technology, 2001.

[6] O.A.J. Peters and R.H.M. Huijsmans. Assesing Hydrodynamic Behavior During Offshore Loading and Discharge in the Heavy Marine Transport. In *Proceedings of the ASME 2011 30nd International Conference on Ocean, Offshore and Arctic Engineering*, Rotterdam, The Netherlands, 2011. OMAE2011-49174.

[7] R. de Bruijn and F. Huijs. Calculation of Wave Forces and Internal Loads on a Semi-Submersible at Shallow Draft Using an iVOF Method. In *Proceedings of the ASME 2011 30th International Conference on Ocean, Offshore and Arctic Engineering*, Rotterdam, The Netherlands, 2011. OMAE2011-49236.

[8] I. van Winsen, J.S. Bokhorst, and R.H.M. Huijsmans. Calculation of Wave Height Dependent Force RAOs on Submerged Bodies in Close Proximity of the Free Surface. In *Proceedings of the 32nd ASME 2013 International Conference on Ocean, Offshore and Arctic Engineering*, Nantes, France, 2013. OMAE2013-10340.

[9] H. Ottens and A. Pistidda. Motion RAOs of a SSCV at Deep and Inconvenient Draft using CFD. In *Proceedings of the ASME 2015 34rd International Conference on Ocean, Offshore and Arctic Engineering*, St John's, Newfoundland, Canada, 2015. OMAE2015-41917.

[10] R. Staroszczyk. Simulation of dam-break flow by a corrected smoothed particle hydrodynamics method. *Hydro-Engineering and Environmental Mechanics*, 57(1):61–79, 2010.

[11] S. Yeylaghi, C. Crawford, P. Oshkai, and B. Buckham. A Comparison of SPH and RANS Models for Simulation of Wave Overtopping. In *5th International Conference on Ocean Energy*, Halifax, 2014.

[12] HMC internal. Thialf inconvenient draft, motion behavior design brief. Technical report, Heerema Marine Contractors, 2014.

[13] J.M.J. Journee and W.W. Massie. *Offshore Hydromechanics.* Delft University of Technology, 2001.

[14] H. Dankowski. *A Fast and Explicit Method for Simulating Flooding and Sinkage Scenarios of Ships.* PhD thesis, Technischen Universitat Hamburg-Harburg, 2013.

[15] O.M. Faltinsen. *Sea Loads on Ship and Offshore Structures.* Cambridge University Press, 1990.

[16] J.O. de Kat and J.R. Paulling. Prediction of Extreme Motions and Capsizing of Ships and Offshore Marine Vehicles. In *Proceedings of the OMAE 2001 20th International Conference on Offshore Mechanics and Arctic Engineering*, Rio de Janeiro, Brazil, 2001. OMAE2001-1280.

[17] T.A. Santon, P. Dupla, and C. Guedes Soares. Numerical Simulation of the Progressive Flooding of a Box-Shaped Barge. In *10th International Conference on Stability of Ships and Ocean Vehicles*, Lispon, Portugal, 2009.

[18] D. Vassalos, O. Turan, and M. Pawlowski. Dynamic stability assessment of damaged passenger/ro-ro ships and proposal of rational survival criteria. *Marine Technology*, 34(4):241–266, 1997.

[19] P. Ruponen. *Progressive Flooding of a Damaged Passenger Ship.* PhD thesis, Helsinki University of Technology, 2007.

[20] T.A. Santon, I.E. Winkle, and C. Guedes Soares. Time domain modelling of the transient asymmetric flooding of ro-ro ships. *Ocean Engineering*, Vol. 29:pp 667–688, 2002.

[21] F.M. White. *Fluid Mechanics.* Mcgraw-Hill Education - Europe, seventh edition edition, 2011.

[22] P. Ackers, W.R. White, J.A. Perkins, and A.J.M. Harrison. *Weirs and Flumes for Flow Measurement.* Wiley, New York, 1978.

[23] T.I. Fossen. *Handbook of Marine Craft Hydrodynamics and Motion Control.* Wiley, United Kingdom, 2011.

[24] W.E. Cummins. The Impulse Response Function and Ship Motions. Technical Report 1661, David Taylor Model Basin, Hydromechanics Laboratory, USA, 1962.

[25] T.F. Ogilvie. Recent Progress Towards the Understanding and Prediction of Ship Motions. In *Proceedings of the 5th Symposium on Naval Hydrodynamics*, Bergen, Norway, 1964.

[26] W.H. Pauw, R.H.M. Huijsmans, and A. Voogt. Advances in the Hydromechanics of Side-by-Side Moored Vessels. In *Proceedings of the 26th International Conference on Offshore Mechanics and Arctic Engineering*, San Diego, California, USA, 2007. OMAE2007-29374.

[27] J.B. Fournier, M. Naciri, and X.B. Chen. Hydrodynamics of two side-by-side vessels, experiments and numerical simulations. In *Proceedings of the IOPSE 2006 Conference*, San Fransisco, California, USA, 2006.

[28] V. Lafon and T. Rippol. SSCV Thialf Model Tests at Shallow Draught. Technical report, OCEANIDE, 2009.

[29] L.H. Holthuijsen. *Waves in Oceanic and Coastal Waters.* Cambridge University Press, 2007.

Glossary

List of Acronyms

HMC	Heerema Marine Contractors
SSCVs	semi-submersible crane vessels
FRF	frequency response function
RAO	Response Amplitude Operator
MDD	Multi-Domain Diffraction
SPH	Smooth Particle Hydrodynamics
CFD	Computational Fluid Dynamics
FFT	Free Flooding Tanks
CoG	Center of Gravity

List of Figures

List of Tables